CHALMERS

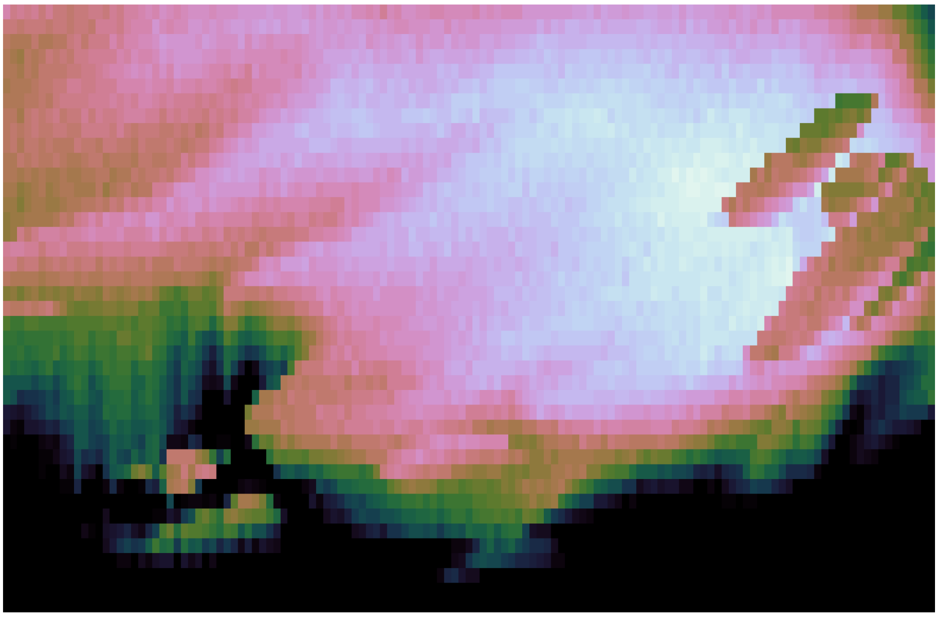

Characterisation of a travelling-wave parametric amplifier for improved qubit measurements

Master's thesis in Master Programme Nanotechnology

HAMPUS RENBERG NILSSON

Department of Microtechnology and Nanoscience
CHALMERS UNIVERSITY OF TECHNOLOGY
Göteborg, Sweden 2019

MASTER'S THESIS 2019

Characterisation of a travelling-wave parametric amplifier for improved qubit measurements

HAMPUS RENBERG NILSSON

Department of Microtechnology and Nanoscience
Division of Quantum Technology Laboratory
CHALMERS UNIVERSITY OF TECHNOLOGY
Gothenburg, Sweden 2019

Characterisation of a travelling-wave parametric amplifier for improved qubit measurements

HAMPUS RENBERG NILSSON

Supervisor and examiner:
Per Delsing, Department of Microtechnology and Nanoscience

Master's Thesis 2019
Department of Microtechnology and Nanoscience
Division of Quantum Technology Laboratory
Chalmers University of Technology
SE-412 96 Göteborg
Telephone +46 31 772 1000

Cover: Signal-to-noise ratio improvement for different pump frequencies and pump powers; average of measurements at 36 different signal frequencies.

Typeset in LaTeX
Printed by Chalmers Reproservice, Chalmers University of Technology
Göteborg, Sweden, May 2019

Characterisation of a travelling-wave parametric amplifier for improved qubit measurements

HAMPUS RENBERG NILSSON
Department of Microtechnology and Nanoscience
Chalmers University of Technology

Abstract

In order to build a large-scale quantum computer, one of the requirements is high-fidelity multiplexed qubit readout, which in turn relies on the use of ultralow-noise amplifiers. While Josephson Parametric Amplifiers (JPAs), using a cavity with few Josephson junctions, have shown promising results for single qubit readout, they have limitations such as low saturation power and a gain-bandwidth product restriction. This makes them less suited for frequency multiplexed qubit readout. A current-pumped Josephson Travelling-Wave Parametric Amplifier (JTWPA), using 4-wave mixing in a lumped-element transmission line, features both high saturation power as well as no restriction on large bandwidth and high gain. This is possible due to multiple junctions and the lack of a cavity. However, also this current pumped JTWPA has an inherent problem, namely phase mismatch between the pump and the signal. This prevents exponential gain. In this thesis, a current pumped JTWPA using the resonant phase matching (RPM) technique to reduce the phase mismatch problem is studied and characterised. The JTWPA shows high gain, high saturation power and a large signal-to-noise ratio improvement. The JTWPA is also used for qubit readout, for which it clearly improves the readout fidelity.

Keywords: parametric amplifier, parametric amplification, low-noise amplifier, ultralow-noise amplifier, Josephson effect, Josephson junction, Josephson travelling-wave parametric amplifier, TWPA, JTWPA, Josephson parametric amplifier, JPA, signal-to-noise ratio, qubit, scattering theory, directional coupler, isolator, circulator, VNA, digitizer, bandwidth, gain, average gain, microwaves, quantum efficiency, noise temperature, fidelity, single-shot readout, noise floor, noise power, up-conversion, down-conversion, frequency mixing, IQ-mixer, arbitrary waveform generator.

Acknowledgements

First and foremost I would like to thank my supervisor and examiner Prof. Per Delsing. Per gave me the opportunity to do this work, supported me throughout the work and introduced me to this field, which has given me an exciting future to look forward to. For this I am truly grateful.

Secondly I would like to thank Dr. Philip Krantz. Despite not being my official nor my unofficial supervisor, Philip has given me many helpful discussions, always been there when I have needed help and given me a lot of invaluable help and support. All our discussions did not only help me with the specifics of this project, but got me a better understanding of the field as a whole.

Thirdly I would like to thank my unofficial supervisor Yong Lu for all the helpful discussions and explanations, as well as spending all those hours in the lab with me. Despite having his own work to do and his own articles to write, he has helped me out a lot, during many hours and late evenings. Without you this would not have been possible.

Then I would like to send my sincere gratitude to Prof. William Oliver's group for realising the RPM-JTWPA and giving one to Chalmers, hence making my project possible. I especially want to thank Dr. Christopher Macklin and Associate Prof. Kevin O'Brien who have given me help and support for my project via e-mail.

Furthermore there are multiple people in the group whom I would like to thank: Simone Gasparinetti for several helpful discussions and explanations, Andreas Bengtsson and Marco Scigliuzzo for many helpful discussions as well as lending me qubits for my measurements, Associate Prof. Jonas Bylander for several discussions about a variety of things, Lars Jönsson for support with bracket fabrication, Anita Fadavi for helpful discussions as well as a good preparation for this work as my supervisor in a previous course, Ida-Maria Svensson for helpful discussions as well as help with getting the right components, Linda Brånell for nice conversations as well as help with all kinds of things in the office and everybody else at the Quantum Technology Laboratory for creating such a nice work environment.

I would also like to thank Janine Splettstößer from the Applied Quantum Physics division, both for good preparations for this kind of work during my Bachelor thesis work, but also for giving me feedback on a draft of this thesis. Then I would also like to thank Dan Kuylenstierna and Johan Karlsson from Microwave Electronics Laboratory for the help with designing a filter. Even though we never finished the design, it was an interesting side project from which I learnt a lot.

Finally I just want to say all love to my family for the support throughout my years at Chalmers: Martin Nilsson, Gudrun Renberg, Anton Nilsson, Amanda Renberg, Alvin Nilsson, Ella Nilsson, Emilia Renberg, Bo Nilsson, Gudrun Nilsson, Karin Renberg, Seline Renberg and Gabriella Grenander. I also want to thank Jenny Almkvist with family for help and support throughout the years.

Hampus Renberg Nilsson, Göteborg, May 2019

Contents

I Thesis

II Appendices

List of Definitions

Name/Symbol	Value/Formula	Description
$T_{\mathrm{N},i}$	–	The noise temperature of an amplifier number i in an amplifier chain.
T_{sys}	$\sum_{i=1}^{n} \frac{T_{\mathrm{N},i}}{\prod_{j=1}^{i-1} G_j}$	The system noise temperature of an amplifier chain of n amplifiers where G_j is the gain of amplifier number j.
I_{c}	–	The critical current for a superconductor or a Josephson junction for which superconductivity is broken if exceeded.
δ	$\theta_2 - \theta_1$	The phase difference over a Josephson junction.
Φ_0	$\frac{h}{2e}$	The superconducting magnetic flux quantum.
φ_0	$\frac{\Phi_0}{2\pi}$	The reduced superconducting magnetic flux quantum.
I_{J}	$I_{\mathrm{c}} \sin \delta$	The current through a Josephson junction.
U_{J}	$\varphi_0 \dot{\delta}$	The voltage over a Josephson junction.
i	$\frac{I_{\mathrm{J}}}{I_{\mathrm{c}}}$	A normalised and unit-less current variable for a Josephson junction.
L_{J0}	$\frac{\varphi_0}{I_{\mathrm{c}}}$	The minimum inductance of a Josephson junction.
L_{J}	$\frac{L_{\mathrm{J0}}}{\cos \delta}$	The Josephson inductance at δ phase difference.

Continued on next page

Continued from previous page

Name/Symbol	**Value/Formula**	**Description**
C_J	–	The intrinsic capacitance of a Josephson junction.
$\boldsymbol{S}$	$\begin{bmatrix} S_{11} & \cdots & S_{1N} \\ \vdots & \ddots & \vdots \\ S_{N1} & \cdots & S_{NN} \end{bmatrix}$	The scattering matrix of an N-port microwave network, describing the ratios between outgoing and incoming voltages.
S_{ij}	–	Element i, j of the scattering matrix $\boldsymbol{S}$, *i.e.* the voltage contribution to U_i^- of U_j^+.
G_eff	$S_{21}^\mathrm{TWPA} - S_{21}^\mathrm{Through}$	The effective gain, *i.e.* the amount of gain an amplifier delivers to a signal compared with not having the amplifier in the system.
G_par	$S_{21}^\text{Pump on} - S_{21}^\text{Pump off}$	The parametric gain, *i.e.* the amount of gain a parametric amplifier delivers turned on compared with transmission through the amplifier when turned off.
κ	$\omega_0 \lvert Q_\mathrm{c} \rvert^{-1}$	The coupling strength between the resonator and the feed line, as a function of the resonator frequency ω_0 and its complex quality factor Q_c.
ω_ac	$2\chi\bar{n}$	The AC Stark shift, *i.e.* a shift of qubit frequency due to photons in the resonator.
$\Gamma_{\varphi,m}$	$8\chi^2\bar{n}\kappa^{-1}$	The measurement induced dephasing, *i.e.* dephasing of a qubit caused by a measurement.
$\bar{n}$	$\dfrac{\omega_\mathrm{ac}}{2\chi}$	The average number of photons in a resonator.

List of Tables

Part I

Thesis

1

Introduction

This chapter aims to introduce the reader to basic concepts relevant for the rest of the thesis. The main goal of the thesis is to improve quantum computation using the studied amplifier, therefore we start by introducing the basics of quantum computation. Then, since a Josephson junction is at the heart of the amplifier studied here which consists of a superconductor-insulator-superconductor junction, we continue with introducing superconductivity and then the Josephson effect, the concepts necessary to understand the Josephson junction. Then we continue with cryogenic cooling, *i.e.* the technique to reach the temperatures where these phenomena take place. Lastly we describe the basic concepts of parametric amplification.

1.1 Quantum computation

Quantum computation is the name of the computation process of a quantum computer, using quantum mechanical effects in order to execute certain algorithms. This allows for a significant computation speedup for certain problems [1]. The basic building block of any quantum computer is a qubit[1]. The basic idea of a qubit is a two-level system that can be put in a superposition state as well as entangled to other qubits. In reality there are usually higher energy levels, but due to a large enough anharmonicity in the qubit the two lowest states can be distinguished from the other states.

A qubit can be built in many different ways, but in this thesis only superconducting transmon qubits have been used. Superconductivity will be explained in Section 1.2 while qubit theory will be explained in Section 2.2. In order for superconductivity to work the qubits need to be cooled down below their critical temperature, therefore cryogenic cooling will be explained below in Section 1.4. The methods about how to calibrate and use a qubit will be explained in Section 3.3.

---

[1] Qubit is short for “quantum bit”, where “bit” refers to the basic information unit of a classical computer.

1.2 Superconductivity

Superconductivity is a phenomenon which most people associate with zero resistance, *i.e.* current flow without dissipation, which is achieved once the material is cooled below a certain critical temperature T_c [2]. This is however not the whole picture.

Firstly, there are mainly two characteristic properties of a superconductor, the first is the known zero resistance property while the other is the Meissner effect. The Meissner effect is the phenomenon that a superconductor completely expels magnetic fields from its interior, see Figure 1.1, except for a tiny fraction of the field at the edge of the material on a tiny characteristic length scale, the penetration depth λ. A perfect conductor, *i.e.* a conductor with zero resistance, would simply require that the internal magnetic flux density is constant, $\partial_t \vec{B} = 0$, which is not as a strong statement as the Meissner effect which states that $\vec{B} = 0$ [3]. Superconductivity is thus more than simply perfect conductivity. The Meissner effect is enabled by the flow of dissipationless supercurrents creating an equally strong magnetic field, but in the opposite direction, as the externally applied one.

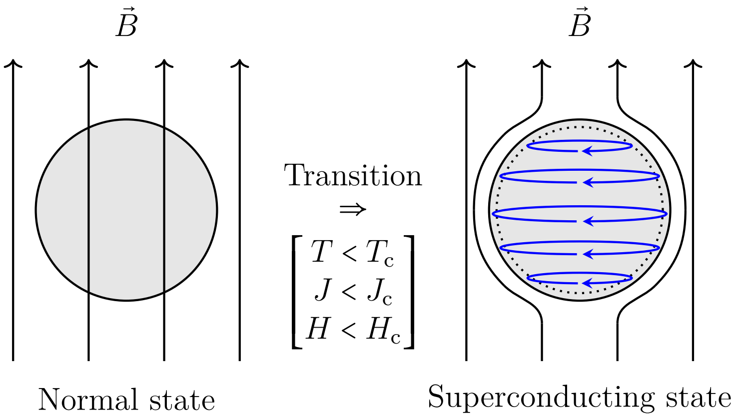

Figure 1.1: Illustration of the Meissner effect. **(Left)** Some metal in its normal state, *i.e.* not superconducting at the moment, is put in a magnetic field $\vec{B}$. **(Right)** The transition to the superconducting state has taken place and all magnetic field $\vec{B}$ is now expelled from the material. The dotted circle illustrates the characteristic penetration depth λ for which the magnetic field manages to penetrate the metal. The blue arrows indicate the flow of supercurrents creating the magnetic field of opposite direction which enables the Meissner effect.

Furthermore, a superconducting material does not only have a critical temperature T_c but also a critical current density J_c and a critical external magnetic field H_c. If any of these are exceeded, superconductivity is broken and the material goes into a resistive state, *i.e.* the normal state.

These critical values are not independent of each other; if one of the parameters (T, J, H) is increased, the critical values of the others are decreased. One could say that the critical temperature is a function of current density and magnetic flux density, $T_c(J,H)$, where the maximum of this function is when J and H are zero, *i.e.* $\max(T_c(J,H)) = T_c(0,0)$. But one could just as well say that the critical current density is a function of temperature and magnetic field, $J_c(T,H)$, or that the critical magnetic field is a function of temperature and current density, $H_c(T,J)$ [4].

When the material goes into its superconducting state, electrons pair up in so called Cooper-pairs. Then they form a so called superconducting condensate, which can be described by a single wave function with an amplitude and a phase describing all the electrons in the condensate.

1.3 Josephson effect

An interesting and very useful superconducting phenomenon is the Josephson effect, which takes place within something called a Josephson junction [5]. A Josephson junction consists of two superconductors connected to each other via some kind of weak link between them, usually an insulating material, see Figure 1.2. There are lots of variations of the weak link, it could be a resistive conductor, a ferromagnetic conductor, another kind of superconductor, *etc*, but I will not go into this deeper here since it is not relevant for this thesis. The interested reader is referred to Reference [6] for further reading. The junctions used in this thesis use an insulator as weak link.

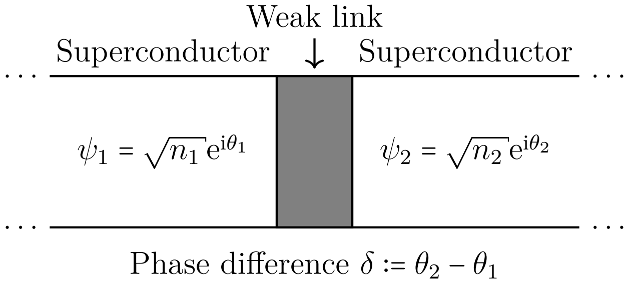

Figure 1.2: Illustration of a Josephson junction. Two superconductors are connected via a weak link. Each superconductor has its own wave function ψ_i where n_i is the Cooper-pair density and θ_i is the phase. The phase difference δ is defined as the difference between the phases of the two superconductor's wave functions.

For an ideal Josephson junction the Josephson relations can be derived [6] to be

$$I_J = I_c \sin\delta \qquad \text{“Josephson I”}, \tag{1.1a}$$

$$U_J = \varphi_0 \dot{\delta} \qquad \text{“Josephson II”}, \tag{1.1b}$$

where U_J is the voltage over the junction, I_J is the current through it, $\varphi_0 := \hbar/(2e)$ is the reduced superconducting magnetic flux quantum, I_c is the Josephson junction critical current and δ is the phase difference over the junction.

Note that for zero voltage, $U_J = 0$, there may still be a supercurrent $I < I_c$ through the junction. For currents greater than the critical current, *i.e.* $I > I_c$, superconductivity is broken and the junction transitions into a resistive state. These relations, usually referred to as the "Josephson relations", give rise to a nonlinear inductance L_J called "the Josephson inductance", which will be derived in Section 1.3.2.

1.3.1 The ideal and real Josephson junction

For any real Josephson junction the interfaces of the superconductors act as tiny capacitor plates, giving rise to an intrinsic capacitance of the junction, C_J. This is easily accounted for in circuit schematics by replacing the real Josephson junction with an ideal junction, which obeys the Josephson relations given in Equations (1.1a) and (1.1b), in parallel with a capacitor with the capacitance C_J, see Figure 1.3.

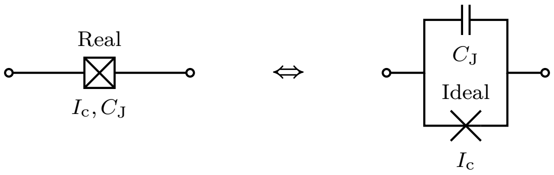

Figure 1.3: (Left) Schematic of a real Josephson junction with critical current I_c and intrinsic capacitance C_J. **(Right)** Circuit equivalent schematic with an ideal junction with the same critical current I_c in parallel with a capacitor with the same capacitance C_J.

1.3.2 Josephson inductance

Inductance describes how much an electrical conductor opposes a change of the electrical current through it [7] and is defined by

$$U = L\frac{\mathrm{d}I}{\mathrm{d}t}. \tag{1.2}$$

We now apply this concept to the Josephson relations to calculate the Josephson inductance. First we use the relation from Equation (1.1a) to calculate $\dot{I}_\mathrm{J}$ as

$$\frac{\mathrm{d}I_\mathrm{J}}{\mathrm{d}t} = I_\mathrm{c}\cos\delta\cdot\dot{\delta}. \tag{1.3}$$

Then we solve Equation (1.2) for the Josephson inductance using Equation (1.1b) together with Equation (1.3),

$$L_\mathrm{J} = \frac{U_\mathrm{J}}{\dot{I}_\mathrm{J}} = \frac{\varphi_0\,\dot{\delta}}{I_\mathrm{c}\cos\delta\cdot\dot{\delta}} = \frac{L_\mathrm{J0}}{\cos\delta} \tag{1.4}$$

where $L_\mathrm{J0} := \varphi_0/I_\mathrm{c}$ is a characteristic constant of a Josephson junction which is completely determined by its critical current. By using the trigonometric identity we can rewrite the cosine as

$$\cos\delta = \pm\sqrt{1-\sin^2\delta} \tag{1.5}$$

where the sign is positive for $\delta \in [-\pi/2, \pi/2]$ and negative for $\delta \in (\pi/2, 3\pi/2)$. By using this and rewriting Equation (1.1a) as $i = \sin\delta$, where $i = I/I_c$ is a normalised and unit-less current variable, we can write the Josephson inductance as

$$L_J = \pm\frac{L_{J0}}{\sqrt{1-i^2}}. \tag{1.6}$$

As we can see in the equation the inductance diverges as the current approaches the critical current, $i \to 1$, which can also be seen in Figure 1.4. We also see that the inductance is non-linear, which is a necessary criterion for parametric amplification.

Using Taylor expansion to the second order for small currents ($i \ll 1$) we get

$$L_J \approx \pm L_{J0}\left(1 + \frac{1}{2}i^2\right) \tag{1.7}$$

which is an approximation we use later. The approximation is also plotted in Figure 1.4. As we see here, the approximation fits well for low currents but approaches $1.5L_{J0}$ for $I \to I_c$.

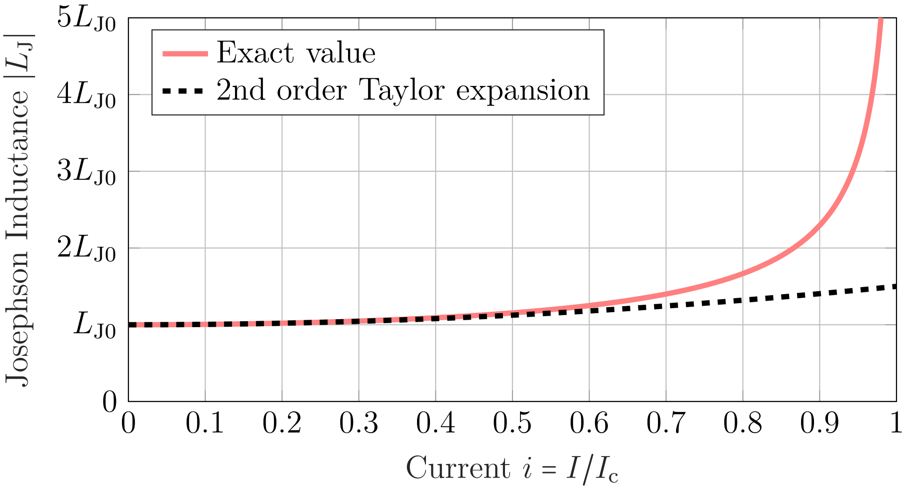

Figure 1.4: Absolute exact and approximate value of the Josephson inductance of a Josephson junction for a current $I \in [0, I_c)$. The inductance for $I = 0$ is L_{J0}, increases for $I \neq 0$ and diverges as $I \to I_c$.

1.4 Cryostats and the dilution refrigerator

A cryostat[2] is used to reach very low temperature, usually < 4 K. Cryogenic temperatures can be achieved with different kinds of refrigeration techniques such as helium-4 evaporation, helium-3 evaporation, Pomeranchuk cooling, nuclear magnetic refrigeration, helium-3-helium-4 dilution, *etc* [8]. All the experiments in this thesis have been performed within a Bluefors LD dilution refrigerator which uses the last of these refrigeration techniques.

---

[2] *Cryo* means cold and *stat* means stable.

The dilution refrigerator is a specific kind of cryostat which can reach ultra low temperatures, typically < 30 mK, and is currently the only known continuous refrigeration method for temperatures below 300 mK [8]. Details about dilution refrigerators and their cooling mechanism are described in Reference [8]. A shorter description of the dilution refrigerator is described in Reference [9].

1.5 Parametric amplification

The amplifier studied in this thesis is a parametric amplifier. A parametric amplifier is an amplifier using some kind of energy source in order to modulate a parameter of a dynamical system to add energy to the signal desired to amplify, instead of adding the energy directly to the signal. Parametric amplification does not require any energy dissipation, making it possible for them to reach quantum-limited noise performance [10].

1.5.1 An intuitive example: a massive particle in a parabolic potential

The principle of parametric amplification is presented in Figure 1.5.

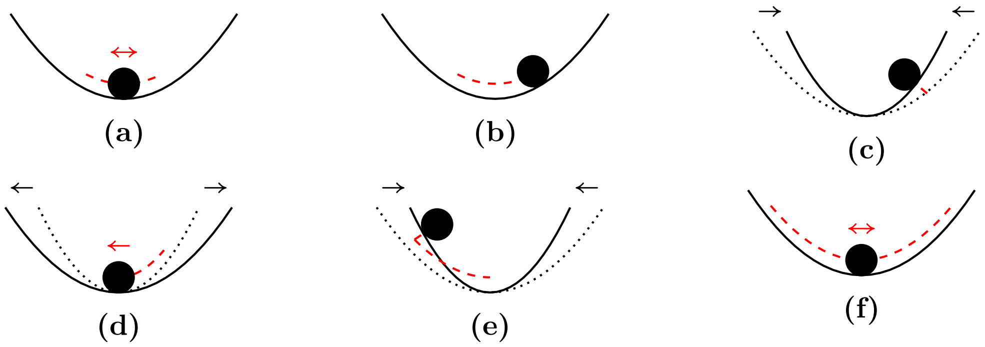

Figure 1.5: A visual representation of parametric amplification. The signal we want to measure is the movement of the particle and the parameter is the curvature of the parabolic potential. **(a)** The signal is very weak, *i.e.* the particle only moves slightly back and forth. **(b)** The particle has just reached its maximum height and is about to turn back. **(c)** The parameter is changed, *i.e.* the curvature of the potential, right before the particle starts moving in the other direction, which makes it go a little higher. **(d)** The particle has reached the lowest point, now with more momentum than before, and the parameter is changed back. **(e)** The particle has just reached its new maximum height and the parameter is changed again, raising it even higher. **(f)** The parameter is changed back and the particle goes back and forth in a much bigger parabola than before, *i.e.* the signal has been amplified by changing the parameter back and forth.

In this example the signal is a massive particle moving back and forth within a parabolic potential and an amplified signal would be equivalent to the particle reaching a higher maximum position in the potential. To accomplish this we could push the particle and hence directly add energy into the system. But alternatively we could, by using parametric amplification, change the curvature of the potential back and forth. By increasing the curvature when the particle is at a high position we increase its potential energy, hence giving it more total mechanical energy. Then by decreasing the curvature when the particle is at a low position, we do not remove the newly added mechanical energy while we make it possible to increase the curvature again. Then we can increase the curvature once again when the particle reaches its new maximum height. In this way the change in the parameter, by twice the particle frequency, leads to signal amplification.

1.5.2 The Josephson Travelling-Wave Parametric Amplifier

The amplifier treated in this thesis is a certain kind of parametric amplifier called a Josephson Travelling-Wave Parametric Amplifier[3], which uses the non-linear inductance of Josephson junctions to achieve parametric amplification of microwaves.

The specific JTWPA treated in this thesis is from MIT, by MIT referred to as "MIT TWPA package 665". In this thesis it is referred to only as "the JTWPA". It is one of MIT's 5th generation JTWPAs.

Another kind of superconducting parametric amplifier is the Josephson Parametric Amplifier (JPA), which is based on a cavity with few Josephson junctions. For this design, the gain-bandwidth product [11] has a restriction which forces the designer to choose between high gain in a narrow range or low gain in a wider range [12]. Due to the low number of junctions, it also features a low saturation power.

In comparison, the JTWPA is not based on a cavity and is thus not limited by the gain-bandwidth product. It can therefore have a much larger bandwidth while also having high gain. Due to the use of multiple junctions, instead of a few in the JPA, it also has a higher saturation power. This makes it much more suitable for multiple applications, *e.g.* multiplexed readout of qubits on the same readout line, *i.e.* amplifying several signals at different frequencies simultaneously.

1.5.3 Pumping types

Generally in parametric amplification the signal that modulates the parameter is usually referred to as the pump. More specifically for TWPAs there are both current pumped and flux pumped TWPAs (see more in Section 2.4.3), *i.e.* the pump is either an alternating current travelling in the same line as the signal, or it is an alternating magnetic flux, inductively coupled to the signal line.

There are also two different amplification processes that can take place, either three-wave mixing or four-wave mixing, and they can be either degenerate or nondegener-

---

[3] Short: JTWPA, or just TWPA, pronounced "two-pa".

ate, as shown in Table 1.1. For the different types of amplification there are different relations between the frequencies which can be found in Table 1.1.

Table 1.1: Frequency relations for different types of parametric amplification. Table is copied from Reference [13]. f_p refers to the pump frequency, f_s to the frequency of the signal to be amplified and f_i the frequency of the idler. Note that degenerate four-wave mixing never is used in reality since then $f_\mathrm{s} = f_\mathrm{p}$.

	Three-wave mixing	**Four-wave mixing**
Degenerate amplification (phase-sensitive)	$f_\mathrm{p} = f_\mathrm{s} + f_\mathrm{i}$ $f_\mathrm{s} = f_\mathrm{i} = \frac{1}{2} f_\mathrm{p}$	$2f_\mathrm{p} = f_\mathrm{s} + f_\mathrm{i}$ $f_\mathrm{s} = f_\mathrm{i} = f_\mathrm{p}$
Nondegenerate amplification (phase-insensitive)	$f_\mathrm{p} = f_\mathrm{s} + f_\mathrm{i}$ $f_\mathrm{s} \neq f_\mathrm{i}$	$2f_\mathrm{p} = f_\mathrm{s} + f_\mathrm{i}$ $f_\mathrm{s} \neq f_\mathrm{i}$

For energy to add up, all amplification processes involve the generation of another signal called the idler, and the type of mixing affects the frequency it will get. For three-wave mixing the idler frequency is symmetrically placed around half the pump frequency, with respect to the signal frequency, while for four-wave mixing the idler frequency is placed symmetrically around the pump frequency.

For degenerate amplification, also known as phase-sensitive amplification, it is possible to achieve noiseless amplification. This is possible due to “quantum squeezing”. The information of a signal is stored both in its amplitude and its phase. When using quantum squeezing, we amplify one of the quadratures[4] while we de-amplify the other [13].

In the regime of degenerate 3-wave mixing, to get parametric amplification it is important that the pump power is below a certain threshold, otherwise the parametric amplification turns into parametric oscillations. Parametric oscillations can also be used for certain applications [14]–[18], also in the nondegenerate case [19], but it has not been studied in this thesis.

For a current pumped TWPA the non-linear inductance of the Josephson junctions permits four-wave mixing [20]. Furthermore we want the amplification to be phase-insensitive, otherwise the signal frequency will be equal to the pump frequency making it hard to distinguish, so the relevant type of amplification in our case is the nondegenerate four-wave mixing, see the lower right corner of Table 1.1. Note that as mentioned above, for four-wave mixing the frequency of the idler will be symmetrically placed around the pump with respect to the signal, *i.e.* if the signal frequency is 1 GHz below the pump, the idler frequency will be 1 GHz above the pump.

---

[4] The two quadratures can be regarded as the real- and imaginary parts of the complex valued signal.

2

Theory

This chapter aims to give the reader a sufficient understanding of the relevant theories for this project. First there is a section about microwave theory, since the signals that we use and amplify are microwave signals. Then we go to something completely different, namely qubit theory, since we will use qubits for several measurements throughout this thesis. Then there is a part about noise theory, since our goal is to reduce the noise and to do this we need to understand where the noise comes from and how to avoid it. Finally there is a section about JTWPA theory where the JTWPA structure and gain derivation are presented.

2.1 Microwave theory

This section will give a brief overview of some microwave theory relevant for the project. Microwaves are typically in the range 3 - 300 GHz, corresponding to wavelengths of 10 cm to 1 mm in vacuum. Because of these short wavelengths, standard circuit theory cannot be used directly in many cases since it assumes the wave lengths to be much longer than the elements they propagate through. For further reading on the subject the reader is recommended to see Reference [21].

2.1.1 Scattering theory and the scattering matrix

When describing waves travelling through some sample and interacting with some kind of elements, scattering theory turns out to be useful to characterise the observed effects. If we have an N-port[1] network, where U_i^+ is the amplitude of the incoming voltage wave at port i and U_i^- is the amplitude of the outgoing voltage wave at port i, then the scattering matrix relates the incoming and outgoing voltage amplitudes in the following way:

$$\begin{bmatrix} U_1^- \\ \vdots \\ U_N^- \end{bmatrix} = \begin{bmatrix} S_{11} & \cdots & S_{1N} \\ \vdots & \ddots & \vdots \\ S_{N1} & \cdots & S_{NN} \end{bmatrix} \begin{bmatrix} U_1^+ \\ \vdots \\ U_N^+ \end{bmatrix} \tag{2.1}$$

---

[1] A port is simply a connection point between one system and another.

or simply just

$$\vec{U}^- = \boldsymbol{S}\vec{U}^+ \tag{2.2}$$

which describes the scattering of the voltage amplitude of each wave. A general picture of a 3-port network is depicted in Figure 2.1.

If a system is characterised by a symmetric scattering matrix, *i.e.* $S_{ij} = S_{ji}\ \forall i, j$, we call it reciprocal, while if $S_{ij} \neq S_{ji}$ for at least one pair of indices i, j, then we call it non-reciprocal [21].

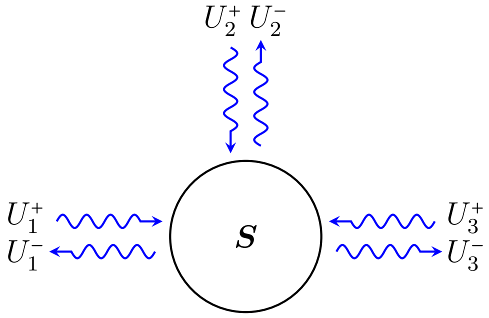

Figure 2.1: A general scattering for a 3-port network. Microwaves with the voltage amplitudes U_i^+ enter the network at port $i \in \{1, 2, 3\}$ and leave the network with the voltage amplitudes U_i^-.

In general the diagonal elements of the scattering matrix describe the reflection at the ports, while the off-diagonal elements describe the transfer between ports. In a more specific example, for a 2-port network with port 1 = IN-port and port 2 = OUT-port it follows that S_{21} relates to the transmission through the device while S_{11} relates to the reflection at the IN-port.

2.1.2 Impedance matching

When a signal travels from one medium to another it is either reflected or transmitted depending on the characteristic impedance of the two media. The reflected power is given by the reflectance R which is given by

$$\Gamma := S_{11} = \frac{Z_2 - Z_1}{Z_2 + Z_1}, \tag{2.3a}$$

$$R := |\Gamma|^2 = \left|\frac{Z_2 - Z_1}{Z_2 + Z_1}\right|^2 \tag{2.3b}$$

where $Z_i, i \in \{1, 2\}$ are the characteristic impedances of the two media. We see that $R = 0$ if $Z_1 = Z_2$ while $R \neq 0$ for $Z_1 \neq Z_2$. In order words, if the two media have the same characteristic impedance, the impedance is matched and there is no reflection, while if there is a difference, the impedance is mismatched and we have a non-zero reflection. In other words, the S_{11}-element of the scattering matrix directly relates to the impedance matching as well as the reflection at the IN-port.

2.1.3 Directional coupler

The directional coupler is one of the components used in this thesis, which we are now going to describe using scattering theory. It is a 4-port network which consists of two lines coupled to each other, usually called the “main line” (port 1 to port 2) and the “coupled line” (port 3 to port 4), see Figure 2.2a. Ideally, if we send a signal into port 1, some of the power[2] P_1 going into port 1 will exit out of port 4 given by the coupling C, $P_4 = P_1 - C$, while the rest goes out of port 2 given by the insertion loss L, $P_2 = P_1 - L$. Equivalently the same applies to the coupled line; some of the power going into port 3 exits out of port 2, $P_2 = P_3 - C$, while the rest of the power goes out of port 4, $P_4 = P_3 - L$.

Another important property of a directional coupler is the directivity, which relates the amount of power going into port 3 to the amount going out of port 1. In other words, if a signal with power P_3 goes into port 3 then a signal with power $P_3 - C - D$ exits out of port 1. For an ideal directional coupler the directivity is $D = \infty\,\mathrm{dB}$ which is equivalent to saying that none of the power going into port 3 goes out of port 1. However, in reality it is finite.

The arrows in the directional coupler in Figure 2.2a show how the ports couple to each other. However, in this work we have always terminated port 4 and only used the directional coupler to couple the pump to the input of the JTWPA. This is illustrated in Figure 2.2b.

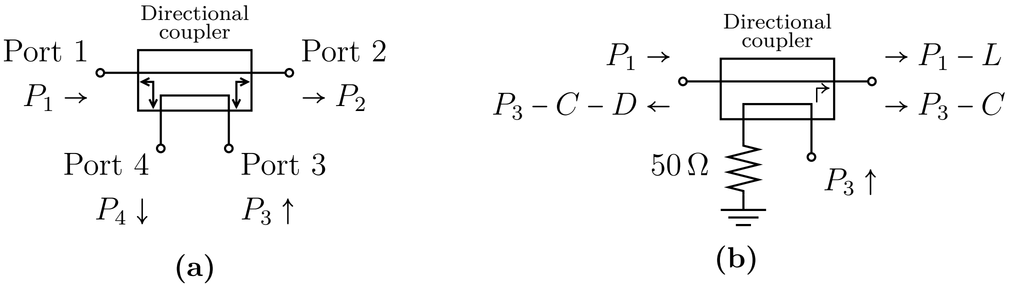

Figure 2.2: A directional coupler. **(a)** A general directional coupler without anything connected to its ports and with directions of input and output powers defined for the usage of this work. **(b)** A terminated directional coupler giving it the desired property of adding two signals together. Two signals with the powers P_1 and P_3 enter the coupler as given in the figure and two signals exit through port 2 with the powers changed due to the effects of the insertion loss L and the coupling C. Some of the power P_3 also exits out of port 1 due to the directivity D, also shown in the figure. There is also power going out of port 4, but it is not shown in the figure since port 4 is terminated with $50\,\Omega$.

If port 4 is perfectly matched with a $50\,\Omega$ termination, see Figure 2.2b, we get the version of the directional coupler most commonly used. In this setup we get the desired property of the coupler, for this thesis, that we can send both signals, signal & pump, to the amplifier.

---

[2] All powers here are expressed in dBm and all coefficients in dB.

A directional coupler is symmetric. We could just as well use port 2 for inputs, terminate port 3 and send signals into port 4 and these signals would exit, at least in theory, through port 1 exactly like the signals exit port 2 in Figure 2.2b.

2.1.4 Circulators and isolators

A circulator is one of the components used for this project. An ideal circulator is a nonreciprocal network with N ports where all of the voltage at port 1 goes out of port 2, the voltage of port 2 goes to port 3 and so on, and the voltage at port N goes to port 1.

The elements of the general scattering matrix of the ideal circulator can be written

$$S_{ij,N\text{-port circulator}} = \begin{cases} 1, & \text{if } i = j + 1 \pmod N \\ 0, & \text{otherwise} \end{cases} \tag{2.4}$$

which is illustrated in Figure 2.3.

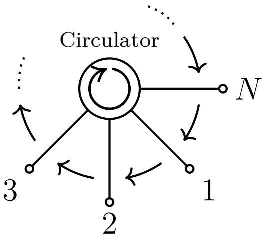

Figure 2.3: A general N-port circulator. The arrows indicate where a signal travels; a signal entering port 1 exits out of port 2, a signal at port 2 exits out of port 3, and so on, and finally the signal entering port N exits out of port 1.

Even though a circulator in theory can have an arbitrary number of ports, it usually has only 3 or 4 ports [22]. For a 3-port ideal circulator the scattering matrix is reduced to

$$\boldsymbol{S}_{\text{3-port circulator}} = \begin{bmatrix} 0 & 0 & 1 \\ 1 & 0 & 0 \\ 0 & 1 & 0 \end{bmatrix}. \tag{2.5}$$

By terminating one of the ports of a 3-port circulator we get an isolator which works like a diode for microwaves. In other words, if port 3 is terminated, microwaves can travel from port 1 to port 2 but not the other way around, see Figure 2.4.

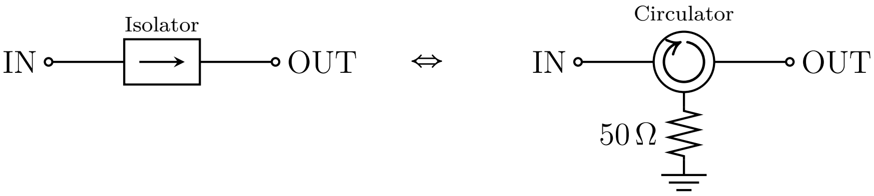

Figure 2.4: Similarities between isolators and circulators. **(Left)** An isolator. **(Right)** An equivalent circuit using a circulator with a 50 Ω termination. Note that the circulator will act as an isolator since signals travelling to the circulator from the OUT-port will exit into the termination.

For the ideal isolator the scattering matrix is reduced to the very simple form

$$\boldsymbol{S}_{\text{isolator}} = \begin{bmatrix} 0 & 0 \\ 1 & 0 \end{bmatrix}. \tag{2.6}$$

In reality we of course never have a completely ideal isolator so there will be some tiny part reflected at the ports, some power from port 2 going out of port 1 and some power loss within the isolator. The reflection at the ports is typically negligible but power loss and power from port 2 to port 1 is not, therefore there are two important quantities one should know about an isolator before using it, namely:

- The insertion loss $L_{\text{isol.}}$, *i.e.* how much power the out-signal has lost compared with the in-signal when travelling from port 1 to port 2. The insertion loss reduces the S_{21}-element of the scattering matrix in Equation (2.6) slightly below 1.
- The isolation $I_{\text{isol.}}$, *i.e.* how much power the out-signal has lost compared with the in-signal when travelling from port 2 to port 1. A finite isolation implies that the S_{12}-element of the scattering matrix in Equation (2.6) is slightly larger than zero.

Both of them are typically dependent on frequency.

A double isolator is simply two isolators in a row, or in terms of circulators two 3-port circulators in a row both with a terminated port. This typically gives both a higher isolation and a higher insertion loss.

2.2 Qubit theory

Now to something completelly else, basic theory of the qubit. The qubit can be any two-level system [1]. Any qubit state can be described by Equation (2.7a), where the coefficients α, β fulfill Equation (2.7b). The equations read

$$|\psi\rangle = \alpha\,|0\rangle + \beta\,|1\rangle\,, \tag{2.7a}$$

$$|\alpha|^2 + |\beta|^2 = 1. \tag{2.7b}$$

Without loss of generality, we can think of the qubit as a spin-1/2 particle in a magnetic field [23]. By putting the global phase to zero, we can then conveniently rewrite Equation (2.7a) as

$$|\psi\rangle = \cos\left(\frac{\theta}{2}\right)\Big|0\Big\rangle + \sin\left(\frac{\theta}{2}\right)\mathrm{e}^{\mathrm{i}\varphi}\Big|1\Big\rangle \tag{2.8}$$

where $\theta \in [0,\pi], \varphi \in [0,2\pi)$ can be thought of as the angles within a unit sphere called the Bloch sphere, see Figure 2.5. Note that $\theta = 0 \implies |\psi\rangle = |0\rangle$ and $\theta = \pi \implies |\psi\rangle = |1\rangle$, while φ contains the phase information of the qubit.

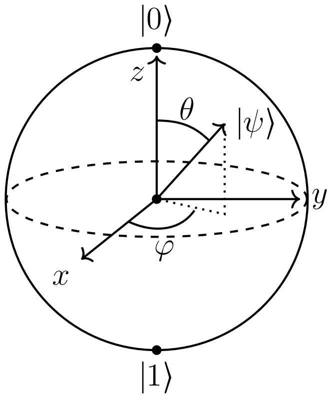

Figure 2.5: The Bloch Sphere with a general qubit state $|\psi\rangle$, where the angle $\theta \in [0,\pi]$ determines the projection on the z-axis and $\varphi \in [0,2\pi]$ is the angle between the x-axis and the projection of the state onto the xy-plane. Note that these two angles completely determine the state of a single qubit.

2.2.1 The transmon qubit

The transmon qubit [24] is a type of superconducting qubit based on the Cooper-pair box[3] [25] with an extra capacitor, and is the one that is used in the experimental work of this thesis. The qubit itself consists of a parallel-plate capacitance in parallel with either a Josephson junction or a SQUID[4]. The transmon used in this thesis had a SQUID making the qubit frequency flux-tuneable, see Figure 2.6. Another qubit that is used is a non-flux-tuneable Xmon, which has a very similar design, see Figure 2.7.

The qubit is capacitively coupled to a quarter-wave resonator which is inductively coupled to a feed line. The interactions between a qubit and a resonator can be described using circuit quantum electrodynamics [26], [27]. Due to the inductive coupling photons travelling through the feed line may interact with the resonator, which interacts with the qubit. If the resonator and the qubit frequencies are well

---

[3] Also known as a charge qubit, a simple circuit with a Josephson junction and a capacitor. Read more in [25].

[4] The SQUIDs (Superconducting Quantum Interference Devices) used here are superconducting loops with two identical Josephson junctions.

detuned we can use the dispersive approximation to describe the interaction, which will be explained further in Section 2.2.3.

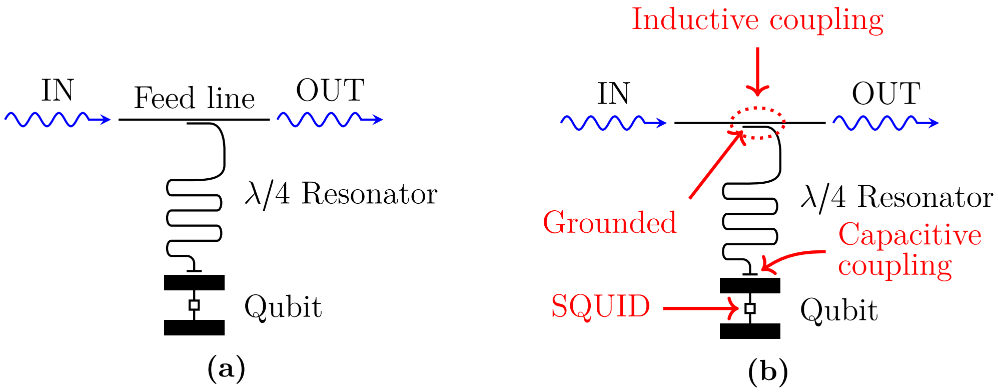

Figure 2.6: **(a)** A flux-tunable transmon qubit with a quarter-wave resonator and a feed line. **(b)** The former with additional comments.

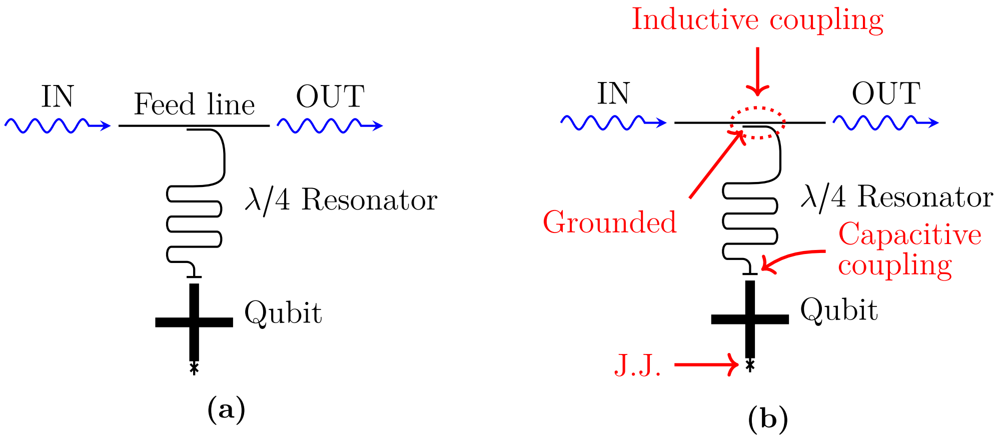

Figure 2.7: **(a)** A non-flux-tunable xmon qubit with a quarter-wave resonator and a feed line. **(b)** The former with additional comments. J.J. is short for Josephson junction.

2.2.2 Qubit control

In the spin-1/2 particle in a magnetic field-analogy, a magnetic field makes the qubit state rotate along the direction the magnetic field points. As long as the magnetic field remains pointing in the same direction, it is easily shown [23] that the exact shape of the pulse is not of importance to determine how the pulse changes the qubit state, but only its amplitude-time-integral. For example, a 100 ns-100 mV rectangular pulse will affect the qubit equally as a 50 ns-200 mV will do.

There are then two kinds of pulses of specific interest for qubit control in this thesis. First let us consider the π-pulse. The π-pulse is a pulse with the integral such that it rotates the qubit state π radians around the some axis, in Figure 2.8 we choose the y-axis. For a qubit in the ground state, as in Figure 2.8a, a perfect π-pulse will put the qubit in the excited state with a 100 % probability.

The second especially interesting pulse is the $\pi/2$-pulse, which only rotates the qubit state $\pi/2$-radians, see Figure 2.9, making a qubit in ground state go to the equator of the Bloch sphere, *i.e.* $|0\rangle \mapsto \frac{1}{\sqrt{2}}\big(|0\rangle + |1\rangle\big)$. A similar pulse is the $-\pi/2$-pulse which rotates $-\pi/2$-radians in the opposite direction, *i.e.* $\frac{1}{\sqrt{2}}\big(|0\rangle + |1\rangle\big) \mapsto |0\rangle$.

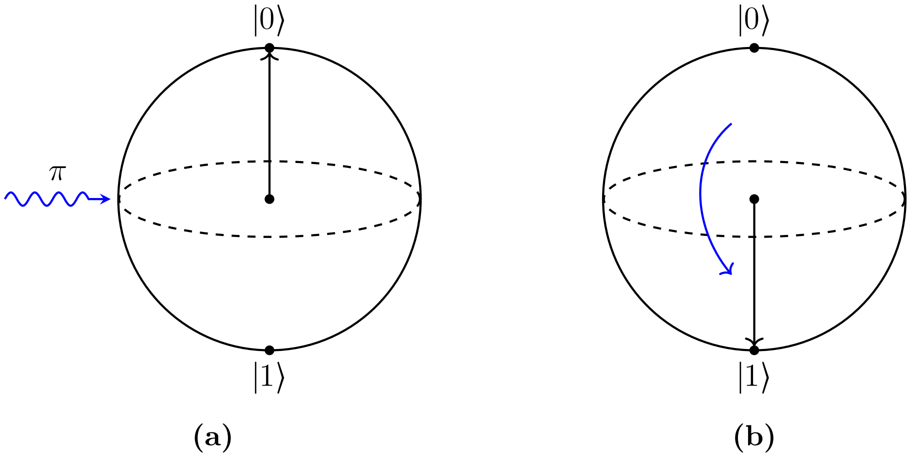

(a) **(b)**

Figure 2.8: Illustration of the π-pulse. **(a)** The qubit is in its ground state when a π-pulse is applied. **(b)** The qubit was just exposed to a π-pulse and is now in its excited state.

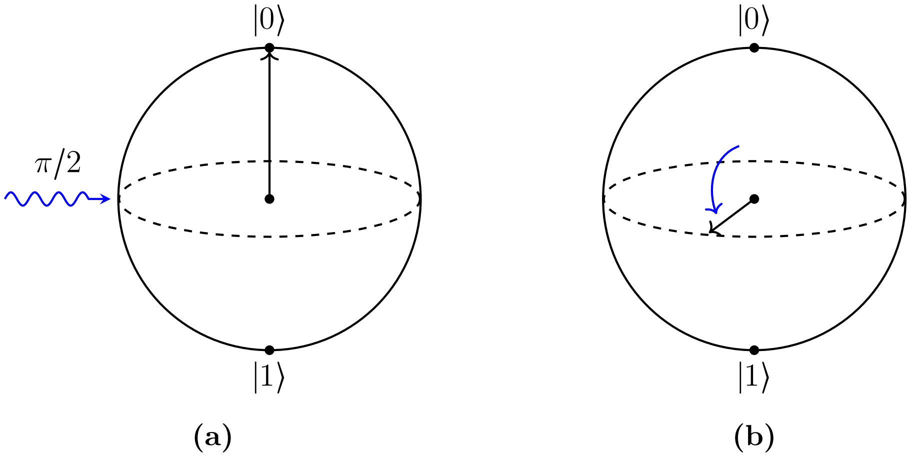

(a) **(b)**

Figure 2.9: Illustration of the $\pi/2$-pulse. **(a)** The qubit is in its ground state when a $\pi/2$-pulse is applied. **(b)** The qubit was just exposed to a $\pi/2$-pulse and is now in the superposition state given by $\theta = \pi/2, \varphi = 0$.

2.2.3 Qubit readout

Below we first explain the Hamiltonian for this system, and then how this is practically affects the choice of readout frequency.

2.2.3.1 The Jaynes-Cummings Hamiltonian

To fully quantum mechanically describe a qubit in a cavity we use the Jaynes-Cummings Hamiltonian [28], [29], which reads

$$\hat{H}_{\text{J.C.}} = \frac{\hbar\omega_0}{2}\sigma_z + \hbar\omega\left(\hat{a}^\dagger\hat{a} + \frac{1}{2}\right) + \hbar g\left(\hat{a}\sigma_+ + \hat{a}^\dagger\sigma_-\right). \tag{2.9}$$

Here ω_0 is the qubit frequency, ω is the angular frequency of the cavity, g is the coupling between the cavity and the qubit, $\hat{a}, \hat{a}^\dagger$ are the annihilation and creation operators for photons in the cavity, $\sigma_\pm$ are the excitation and de-excitation operators of the qubit and σ_z is the Pauli z spin matrix.

In the case of large detuning between the qubit frequency and the resonator frequency, *i.e.* the dispersive regime where $|\Delta| \gg g, \Delta := \omega_0 - \omega$, we can use perturbation theory to rewrite this Hamiltonian. We assume that the number of photons is below a certain critical photon number [30] and we can thus rewrite the Jaynes-Cummings Hamiltonian [31] as

$$\hat{H}_{\text{disp}} = \hbar\Big(\omega + \chi\sigma_z\Big)\hat{n} + \frac{\hbar\tilde{\omega}_0}{2}\sigma_z, \tag{2.10}$$

where $\chi := g^2/\Delta$ is the dispersive shift, $\hat{n} = \hat{a}^\dagger\hat{a}$ is the number operator and $\tilde{\omega}_0 = \omega_0 + \chi$ is the new effective qubit frequency. This Hamiltonian is known as the dispersive Hamiltonian.

In this dispersive region the photons in the resonator cannot induce any transitions in the qubit, but the state of the qubit still affects the effective cavity frequency. We also see that the shift depends on the number of photons n in the cavity.

2.2.3.2 Choosing readout frequency

To readout the state of the qubit, we probe the resonator by sending a pulse at the resonator frequency along the feedline (recall Figure 2.6) and measure the transmission. Study Figure 2.10. We can probe the resonator at a frequency which either give us a big difference of the output in magnitude or in phase, in the figure marked at a frequency with big difference in magnitude. Then we can deduct the state of the qubit depending on whether we get high or low transmission. The readout contrast is determined by the difference between the two curves, see “Readout contrast” in Figure 2.10. The signal we are interested in measuring is hence the resonator probing pulse, to see whether many or a few of these photons are transmitted. Information about the state can also be given by the phase of the probing signal, if one probes at another frequency with high difference in phase between the states.

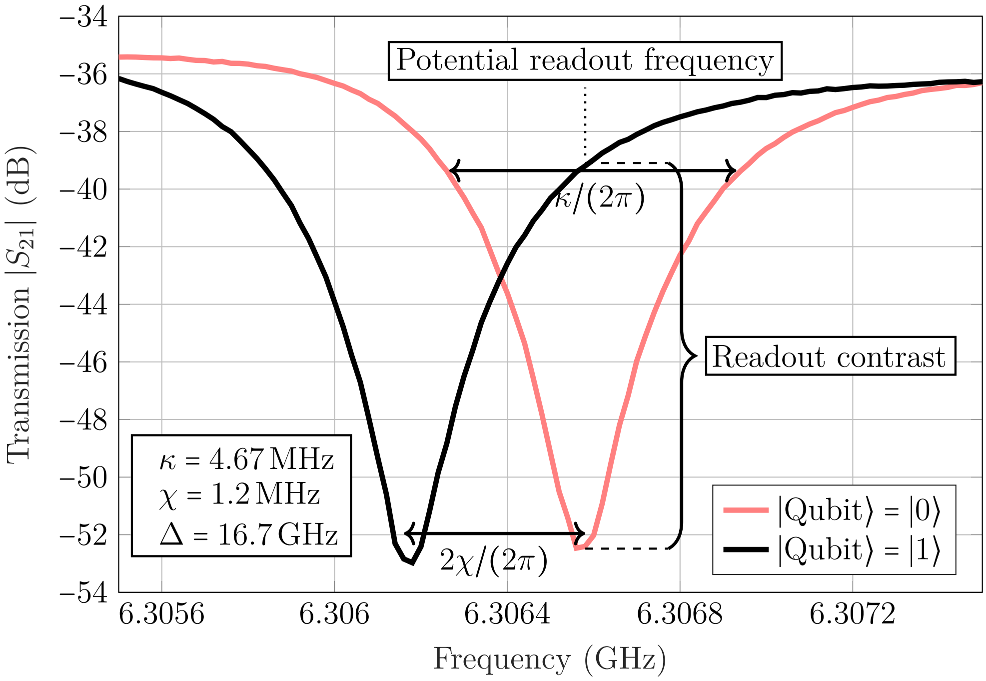

Figure 2.10: A measurement of the dispersive shift, illustrating the effect the state of the qubit has on the resonator. The readout frequency is swept while measuring transmission magnitude $|S_{21}|$ while the qubit is either in its ground state or its excited state. To readout the qubit state we pick a frequency in this range where the difference between the two curves is large, *e.g.* the frequency marked in the figure, and measure the transmission at this frequency. Note that the parameters in the box, the coupling strength κ, the dispersive shift χ and the resonator-qubit-detuning Δ, all are expressed in angular frequency, so to get them in non-angular frequency one has to divide by 2π.

2.3 Noise theory

In a noiseless environment any difference between two quantum states, *e.g.* the states of a qubit, would suffice in order to unambiguously distinguish one state from the other. However, in reality there is always noise, making the readout result of a quantum state distributed in the IQ-plane [10]. In most cases the distribution is Gaussian. Then, depending on the overlap between the state distributions, there will be some uncertainty when trying to determine a state.

The noise has multiple origins; there is vacuum noise, there is noise added by the amplifier due to Heisenberg's uncertainty principle, there may be non-idealities in the equipment used and also losses between the signal source and the first amplifier which appear as added noise [10], [31].

2.3.1 System noise temperature

The system noise temperature T_{sys}, which describes the total noise temperature of a chain of k amplifiers, is given by Friis' formula,

$$T_{\mathrm{sys}} = \sum_{i=1}^{k} \frac{T_{\mathrm{N},i}}{\prod_{j=1}^{i-1} G_j} = T_{\mathrm{N},1} + \frac{T_{\mathrm{N},2}}{G_1} + \frac{T_{\mathrm{N},3}}{G_1 G_2} + \ldots, \tag{2.11}$$

where $T_{\mathrm{N},i}$ is the noise temperature of amplifier i and G_j is the gain of amplifier j. This formula can easily be derived, see Appendix C.1.

Note that when $G_1 \to \infty$ then $T_{\mathrm{sys}} \to T_{\mathrm{N},1}$. In other words, if the first amplifier has a large gain, the noise temperature of the system as a whole will be dominated by the noise temperature of the first amplifier.

2.3.2 Signal-to-Noise Ratio

As mentioned above, if we measure and plot a quantum state in the IQ-plane, the data points will display a Gaussian distribution. The width of the distribution will correspond to the noise while the distance between the state and the origin will correspond to the signal strength and the direction from the origin to the state will correspond to the phase information about the state.

If we have two states, *e.g.* the states of a qubit $|0\rangle$ and $|1\rangle$, it is the overlap between the distributions that determine the fidelity, *i.e.* how well we can distinguish the states. If we amplify the signal and the noise equally then the overlap remains unchanged. It is hence not only the gain that is an important factor, but the ratio between the signal and the noise, known as Signal-to-Noise Ratio (SNR).

In other words, if the JTWPA in one case has mediocre gain but a low noise temperature and in another case has a larger gain but also a higher noise temperature, the former might distinguish the two states better than the latter. For some cases the JTWPA might even have a large gain but adding so much noise that it actually makes the readout resolution worse than compared with not using the JTWPA at all. An illustration of this is presented in Figure 2.11.

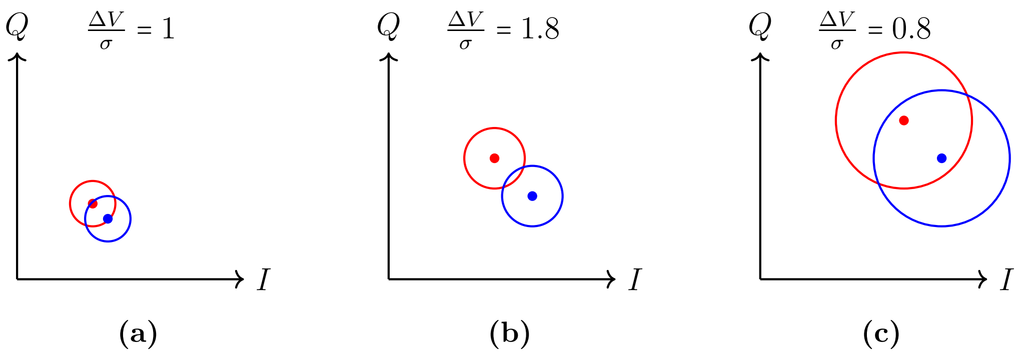

Figure 2.11: An illustration of distributed quantum states. The dot signifies the expectation value of the quantum state and the circle one standard deviation away from the expectation value. The value $\frac{\Delta V}{\sigma}$ is the difference between expectation values divided by one standard deviation. **(a)** The two states have some overlap when only using the other amplifiers. **(b)** The states are amplified also with a JTWPA and not much noise is added, resulting in a decreased overlap. **(c)** The states are greatly amplified but also much noise is added, resulting in an increased overlap.

2.3.3 The Standard Quantum Limit

The quantum state distributions depicted in Figure 2.11 cannot get arbitrarily small standard deviations. Due to Heisenberg's uncertainty principle, there is a fundamental lowest value in accuracy possible to achieve, caused by so called "vacuum noise". This noise limit corresponds to adding half a noise photon. This limit not even noiseless degenerate amplification, as described in Section 1.5.3, can surpass.

However, when using non-degenerate amplification, another half a photon must be added [12] unless the gain is very low [13]. This results in a new lowest limit of adding one whole noise photon, one half from the vacuum noise and one half from the non-degenerate amplification. This limit we call the Standard Quantum Limit (S.Q.L.). As long as we use non-degenerate amplification, we cannot surpass this limit.

2.4 JTWPA theory

Below the theory to understand the JTWPA, its structure and the theory for the amplification process, is presented.

2.4.1 Structure and unit cell

The structure of the JTWPA is nothing more than a long chain of JTWPA unit cells, see Figure 2.12, where the unit cells are built as presented in Figure 2.13.

Each unit cell consists of n Josephson cells followed by an RPM[5] resonator.

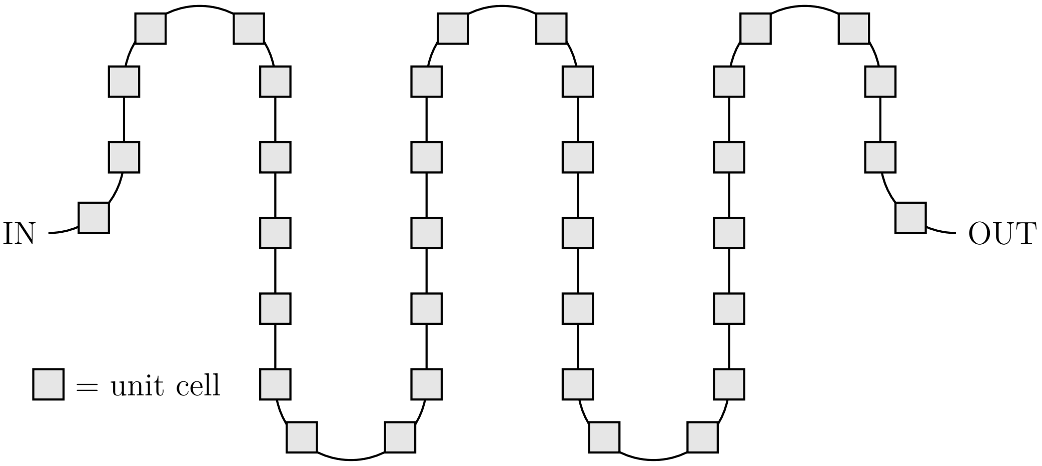

Figure 2.12: A basic overview of the JTWPA structure. Each gray box signifies a JTWPA unit cell. The JTWPA used in this thesis has approximately 700 of these unit cells.

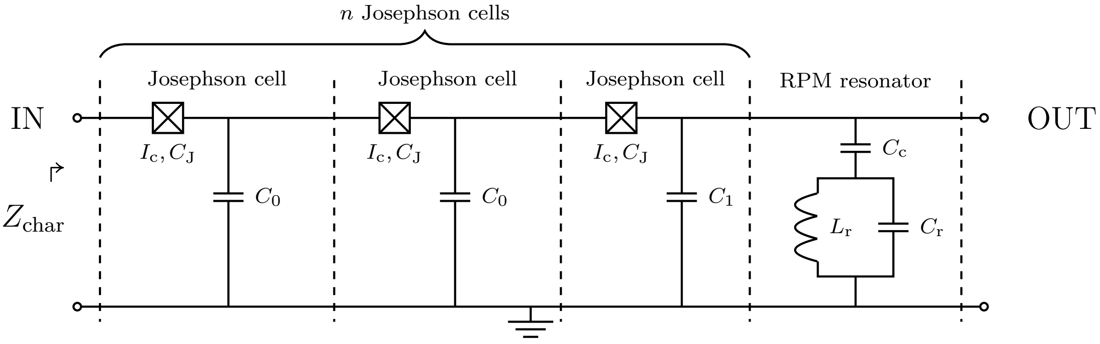

Figure 2.13: A circuit diagram of the JTWPA unit cell. The unit cell consists of n Josephson cells, in this figure $n = 3$, followed by an RPM resonator. The Josephson cell consists of a Josephson junction with a Josephson inductance L_J, an intrinsic capacitance C_J and a critical current I_c and a capacitive shunt C_g, $g \in \{0, 1\}$, to ground. The RPM resonator is coupled to the line with a strength set by the capacitance C_c and consists of a capacitance C_r in parallel with an inductance L_r. The capacitance C_1 of the n:th Josephson cell is slightly less than the capacitance C_0 of the other Josephson cells in order to compensate for C_c. The relations between these inductances and capacitances are designed such that the characteristic impedance Z_{char} is expected to be close to $50\,\Omega$.

There is also another convention used in other papers to define the unit cell, *e.g.* in Reference [20]. Then the unit cell would either be just a Josephson cell or a Josephson cell followed by an RPM resonator. In this thesis I have chosen to use the definition of the unit cell above so that “unit cell” only refers to one kind of cell and not two different kinds of cells.

---

[5] RPM = Resonant phase matching, see Section 2.4.2.

2.4.2 Resonant phase matching and the stopband

In previous versions of JTWPAs, the JTWPA unit cell only consisted of a Josephson cell. Then the gain was limited because exponential gain is only achieved for a low phase mismatch between the signal and the pump, something which will be shown further down in Section 2.4.4. For a strong pump the phase velocities are changed due to self- and cross-modulation which gives a phase mismatch and hence no exponential gain [32].

By adding a resonator, the RPM resonator, to the unit cell the dispersion relation diverges to infinity close to the resonance frequency of the RPM resonator. Then, if the pump frequency is set to be just below the resonance frequency of the RPM resonator, the new dispersion relation will give the wave vector of the pump the increase necessary to make the phase mismatch small enough to get exponential gain [32].

Due to these resonators the dispersive feature will effectively work like a stopband around the resonator frequency. However, when the pump is on, there will be an effective stopband twice as wide. The reason for this is that we use 4-wave mixing and hence, recall Table 1.1, the idler frequency will be symmetrically placed around the pump frequency. Assume that the stopband of the dispersive feature reaches from $f_{\text{lower}}^{\text{disp}}$ to $f_{\text{upper}}^{\text{disp}}$ with a bandwidth $BW_{\text{disp}} := f_{\text{upper}}^{\text{disp}} - f_{\text{lower}}^{\text{disp}}$, and that the pump frequency $f_{\text{p}} \approx f_{\text{lower}}^{\text{disp}}$. If the signal frequency f_{s} is inside the stopband it cannot be amplified. But also, if f_{s} is less than BW_{disp} below f_{p} then the idler frequency f_{i} will end up in the stopband. Then the signal cannot be amplified either, since parametric amplification requires that the idler also is amplified. We can hence conclude that the effective stop-bandwidth should have the same upper limit as the dispersive feature, while the lower limit should reach the distance between the pump and the upper limit. In other words,

$$f_{\text{upper}}^{\text{stopband}} = f_{\text{upper}}^{\text{disp}} := f_{\text{upper}}, \tag{2.12a}$$

$$f_{\text{lower}}^{\text{stopband}} = f_{\text{lower}}^{\text{disp}} - BW_{\text{disp}} \approx 2f_{\text{p}} - f_{\text{upper}}, \tag{2.12b}$$

$$BW_{\text{stopband}} \approx f_{\text{upper}} - (2f_{\text{p}} - f_{\text{upper}}) = 2(f_{\text{upper}} - f_{\text{p}}). \tag{2.12c}$$

where f_{p} is the pump frequency, f_i^{disp} are the lower and upper bounds of the dispersive feature (for $i \in \{\text{lower,upper}\}$), f_i^{stopband} are the lower and upper bounds of the effective stopband when the pump is on, and BW_j are the bandwidths of the dispersive feature and the effective stopband respectively (for $j \in \{\text{disp,stopband}\}$).

2.4.3 Current pumping versus flux pumping

In this thesis I have only worked with implementing a current based JTWPA, using the Josephson cell as shown above. But there are also flux pumped TWPAs, which are based on SQUID cells instead. The structure of the flux based JTWPA is very similar to the current pumped one. It also consists of a chain of similar unit cells, except that they do not contain any RPM resonators since the phase matching is inherently good [33]. The other difference is that the unit cell does not contain Josephson cells, as in Figure 2.14a, but SQUID cells, see Figure 2.14b.

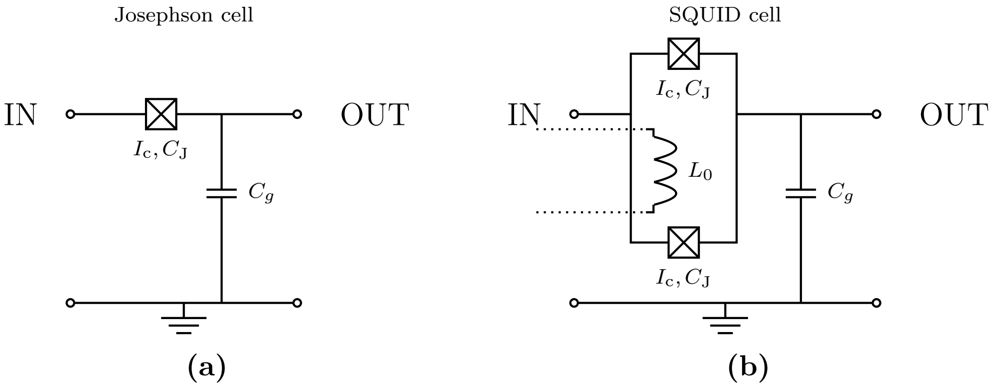

Figure 2.14: The different subcells for the current pumped JTWPA and the flux pumped JTWPA. **(a)** The Josephson cell, the basis for the current pumped JTWPA, just as in Figure 2.13. **(b)** The SQUID cell, the basis for the flux pumped TWPA. In the SQUID cell the Josephson junction is replaced with a DC-SQUID, *i.e.* two Josephson junctions in parallel with each other. An inductance L_0 is inductively coupled to the SQUID which induces the flux.

2.4.4 Analytical calculation of JTWPA gain

In this section I will present a reduced version of the derivation of the gain of a current pumped JTWPA. The full derivation can be found in Reference [12] Chapter 7 and Appendix A.

2.4.4.1 Derivation of the discrete wave equation

In this section I go through the derivation of the discrete wave equation very similar to the one done in Reference [12], but slightly different in order to use what we have already defined and derived.

Study Figure 2.15 and its definitions, where each Josephson junction in each Josephson cell has been split up into an ideal junction and a capacitor.

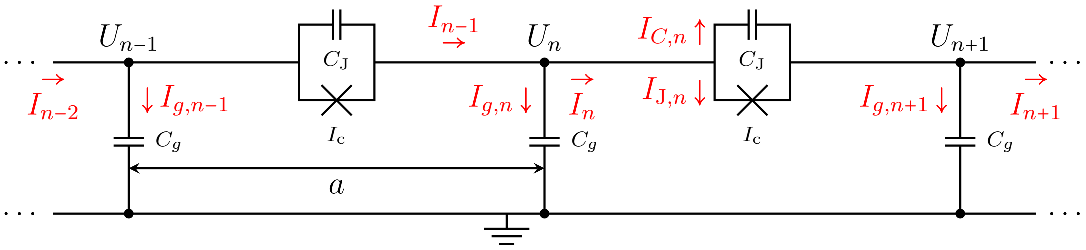

Figure 2.15: A chain of Josephson cells with definitions for voltages and currents. Note that the Josephson junctions have been split up in ideal junctions in parallel with a capacitor, as discussed in Section 1.3.1.

We know from Section 1.3.2 that for the n:th Josephson junction

$$U_{\mathrm{J},n} = L_{\mathrm{J},n}\frac{\mathrm{d}I_{\mathrm{J},n}}{\mathrm{d}t} \approx L_{\mathrm{J0}}\left(1 + \frac{1}{2}\frac{I_{\mathrm{J},n}^2}{I_\mathrm{c}^2}\right)\frac{\mathrm{d}I_{\mathrm{J},n}}{\mathrm{d}t} \tag{2.13}$$

for $I_{\mathrm{J},n} \ll I_\mathrm{c}$. By noting that the voltage over the n:th Josephson junction with current $I_{\mathrm{J},n}$ equals the difference between the node voltages, *i.e.* $U_{\mathrm{J},n} = U_n - U_{n+1}$, we can rewrite Equation (2.13) as

$$U_{n+1} - U_n = -L_{\mathrm{J0}}\frac{\mathrm{d}I_{\mathrm{J},n}}{\mathrm{d}t} - \frac{L_{\mathrm{J0}}}{2}\left(\frac{I_{\mathrm{J},n}}{I_\mathrm{c}}\right)^2\frac{\mathrm{d}I_{\mathrm{J},n}}{\mathrm{d}t} = -L_{\mathrm{J0}}\frac{\mathrm{d}I_{\mathrm{J},n}}{\mathrm{d}t} - \frac{L_{\mathrm{J0}}}{6I_\mathrm{c}^2}\left[3I_{\mathrm{J},n}^2\right]\frac{\mathrm{d}I_{\mathrm{J},n}}{\mathrm{d}t}. \tag{2.14}$$

Then by noting that

$$\frac{\mathrm{d}}{\mathrm{d}t}I_{\mathrm{J},n}^3 = 3I_{\mathrm{J},n}^2\frac{\mathrm{d}I_{\mathrm{J},n}}{\mathrm{d}t} \tag{2.15}$$

we get

$$U_{n+1} - U_n = -L_{\mathrm{J0}}\frac{\mathrm{d}I_{\mathrm{J},n}}{\mathrm{d}t} - \frac{L_{\mathrm{J0}}}{6I_\mathrm{c}^2}\frac{\mathrm{d}}{\mathrm{d}t}I_{\mathrm{J},n}^3. \tag{2.16}$$

Now by defining the node fluxes Φ_n such that

$$U_n := \frac{\mathrm{d}\Phi_n}{\mathrm{d}t} \tag{2.17}$$

and integrating Equation (2.16) over time we get

$$\Phi_{n+1} - \Phi_n = -L_{\mathrm{J0}}I_{\mathrm{J},n} - \frac{L_{\mathrm{J0}}}{6I_\mathrm{c}^2}I_{\mathrm{J},n}^3. \tag{2.18}$$

By rewriting this for $I_{\mathrm{J},n}$ and assuming that the nonlinear term is small we get

$$I_{\mathrm{J},n} = -\frac{1}{L_{\mathrm{J0}}}\left(\Phi_{n+1} - \Phi_n\right) - \cancelto{0}{\frac{1}{6I_\mathrm{c}^2}I_{\mathrm{J},n}^3} \approx -\frac{1}{L_{\mathrm{J0}}}\left(\Phi_{n+1} - \Phi_n\right) \tag{2.19}$$

And by now putting this approximate value of $I_{\mathrm{J},n}$ into the cubic term in Equation (2.18) we get

$$\Phi_{n+1} - \Phi_n = -L_{\mathrm{J0}}I_{\mathrm{J},n} + \frac{1}{6I_\mathrm{c}^2L_{\mathrm{J0}}^2}\left(\Phi_{n+1} - \Phi_n\right)^3 \tag{2.20}$$

which we can solve for the current to be

$$I_{\mathrm{J},n} = -\frac{1}{L_{\mathrm{J0}}}(\Phi_{n+1} - \Phi_n) + \frac{1}{6\varphi_0^2 L_{\mathrm{J0}}}(\Phi_{n+1} - \Phi_n)^3. \tag{2.21}$$

Now let us note that current conservation implies that

$$I_n = I_{\mathrm{J},n} + I_{C,n}, \tag{2.22a}$$

$$I_{g,n} = I_{n-1} - I_n, \tag{2.22b}$$

$$\implies -I_{g,n} = I_{\mathrm{J},n} - I_{\mathrm{J},n-1} + I_{C,n} - I_{C,n-1}. \tag{2.22c}$$

The current to ground is given by

$$I_{g,n} = -C_g \frac{\mathrm{d}}{\mathrm{d}t}(0 - U_n) = C_g \frac{\mathrm{d}U_n}{\mathrm{d}t} = \{\text{Equation (2.17)}\} = C_g \frac{\mathrm{d}^2\Phi_n}{\mathrm{d}t^2} \tag{2.23}$$

and the current corresponding to the current going through the intrinsic capacitance of the Josephson junction is given by

$$I_{C,n} = -C_{\mathrm{J}} \frac{\mathrm{d}}{\mathrm{d}t}(U_{n+1} - U_n) = \{\text{Equation (2.17)}\} = -C_{\mathrm{J}} \frac{\mathrm{d}^2}{\mathrm{d}t^2}(\Phi_{n+1} - \Phi_n). \tag{2.24}$$

Now, let us rewrite Equation (2.22c). By using Equation (2.21) to express $I_{\mathrm{J},n} - I_{\mathrm{J},n-1}$ of Equation (2.22c), Equation (2.24) to express $I_{C,n} - I_{C,n-1}$ of Equation (2.22c) and Equation (2.23) to express the left-hand side of Equation (2.22c), we finally arrive at the discrete wave equation for the JTWPA,

$$\begin{aligned} -C_g \frac{\mathrm{d}^2\Phi_n}{\mathrm{d}t^2} = {} & \left[-C_{\mathrm{J}} \frac{\mathrm{d}^2}{\mathrm{d}t^2} - \frac{1}{L_{\mathrm{J0}}}\right]\big(\Phi_{n+1} - 2\Phi_n + \Phi_{n-1}\big) \\ & + \frac{1}{6\varphi_0^2 L_{\mathrm{J0}}}\Big(\big(\Phi_{n+1} - \Phi_n\big)^3 - \big(\Phi_n - \Phi_{n-1}\big)^3\Big). \end{aligned} \tag{2.25}$$

2.4.4.2 Derivation of the continuum wave equation

Now we would like to take the discrete wave equation and turn it into a continuous equation. The length of the Josephson cell $a = 16\,\mu\mathrm{m}$ [20] and the wave length of the shortest waves that are going to be used ($f = 8\,\mathrm{GHz}$) is ~9.43 mm (on silicon), giving us that $a/\lambda \approx 1.7 \cdot 10^{-3}$. We can hence use the approximation that the wave length of a propagating wave is much longer than the cell, $a/\lambda \ll 1$, and then we can replace the node fluxes $\Phi_n(t)$ with a continuous flux variable $\phi(x,t)$ dependent on the continuous position x and replace the differences of the discrete wave equation with their continuous counterparts to the second order in a/λ and we get

$$\Phi_{n+1} - \Phi_n \approx a\frac{\partial\phi}{\partial x} + \frac{1}{2}a^2\frac{\partial^2\phi}{\partial x^2}, \tag{2.26a}$$

$$\Phi_n - \Phi_{n-1} \approx a\frac{\partial\phi}{\partial x} - \frac{1}{2}a^2\frac{\partial^2\phi}{\partial x^2}, \tag{2.26b}$$

$$\implies \Phi_{n+1} - 2\Phi_n + \Phi_{n-1} \approx a^2\frac{\partial^2\phi}{\partial x^2} \tag{2.26c}$$

and

$$\left(\Phi_{n+1}-\Phi_n\right)^3-\left(\Phi_n-\Phi_{n-1}\right)^3\approx 3a^4\frac{\partial^2\phi}{\partial x^2}\left(\frac{\partial\phi}{\partial x}\right)^2. \tag{2.27}$$

Thus we can now rewrite Equation (2.25) as a continuous equation,

$$\left[C_g\frac{\partial^2}{\partial t^2}-C_{\mathrm{J}}a^2\frac{\partial^2}{\partial t^2}\frac{\partial^2}{\partial x^2}-\frac{a^2}{L_{\mathrm{J0}}}\frac{\partial^2}{\partial x^2}\right]\phi+\frac{a^4}{2\varphi_0^2L_{\mathrm{J0}}}\frac{\partial^2\phi}{\partial x^2}\left(\frac{\partial\phi}{\partial x}\right)^2=0, \tag{2.28}$$

which we will call the continuum wave equation of the JTWPA.

2.4.4.3 Summary of JTWPA parametric amplification derivation

The full calculation of the parametric amplification of the JTWPA is rather tedious but can be found in Reference [12] Appendix A. Here I will only summarise the most important parts of this derivation. First we use the continuum wave equation of the JTWPA as derived above with the ansatz that the solutions are forward travelling waves given by

$$\phi=\sum_j\phi_j,\quad \phi_j=\frac{1}{2}A_j(x)\mathrm{e}^{\mathrm{i}(k_jx+\omega_jt)} \tag{2.29}$$

for $j\in\{\mathrm{s,i,p}\}$ where 's' denotes signal, 'i' idler and 'p' pump. Then we use the slowly varying envelope approximation[6], we neglect the small frequency dependence of the wave impedances and the small dispersion due to C_{J} and we use the stiff pump approximation[7]. Then with the definitions

$$A_{\mathrm{s}}=a_{\mathrm{s}}\mathrm{e}^{\mathrm{i}\alpha_{\mathrm{s}}x}, \tag{2.30a}$$

$$A_{\mathrm{i}}=a_{\mathrm{i}}\mathrm{e}^{\mathrm{i}\alpha_{\mathrm{i}}x}, \tag{2.30b}$$

$$k_j=\frac{\omega_j\sqrt{C_gL_{\mathrm{J0}}}}{a\sqrt{1-C_{\mathrm{J}}L_{\mathrm{J0}}\omega_j^2}}, \tag{2.30c}$$

$$\kappa=\frac{a^2k_{\mathrm{p}}^2\left|Z_{\mathrm{char}}\right|^2}{16L_{\mathrm{J0}}^2\omega_{\mathrm{p}}^2}\left(\frac{I_{\mathrm{p}}}{I_{\mathrm{c}}}\right)^2, \tag{2.30d}$$

$$\kappa_{\mathrm{s}}=\frac{\kappa(2k_{\mathrm{p}}-k_{\mathrm{i}})k_{\mathrm{s}}k_{\mathrm{i}}a^2}{L_{\mathrm{J0}}C_g\omega_{\mathrm{s}}^2}, \tag{2.30e}$$

$$\kappa_{\mathrm{i}}=\frac{\kappa(2k_{\mathrm{p}}-k_{\mathrm{s}})k_{\mathrm{s}}k_{\mathrm{i}}a^2}{L_{\mathrm{J0}}C_g\omega_{\mathrm{i}}^2}, \tag{2.30f}$$

$$\Delta k_L=2k_{\mathrm{p}}-k_{\mathrm{s}}-k_{\mathrm{i}}, \tag{2.30g}$$

$$\Delta k\approx\Delta k_L-2k_{\mathrm{p}}\kappa \tag{2.30h}$$

---

[6] The approximation that the second derivative with respect to unit length is much smaller than the first derivative times the wave vector.

[7] we assume the that the energy of the pump remains the same over the length of the transmission line

we arrive at the coupled equations

$$\frac{\partial a_{\mathrm{s}}}{\partial x} - \mathrm{i}\kappa_{\mathrm{s}}\bar{a}_{\mathrm{i}}\mathrm{e}^{\mathrm{i}\Delta kx} = 0, \tag{2.31a}$$

$$\frac{\partial a_{\mathrm{i}}}{\partial x} - \mathrm{i}\kappa_{\mathrm{i}}\bar{a}_{\mathrm{s}}\mathrm{e}^{\mathrm{i}\Delta kx} = 0. \tag{2.31b}$$

Here the a_j are the slowly-varying amplitudes of the signal and the idler, Δk_L is the phase mismatch in the low pump power limit and Δk is the phase mismatch taking the self-phase and cross-phase modulation into consideration. Note the approximation done in Equation (2.30h) is the one done by neglecting the small frequency dependence of the wave impedances, as well as the small dispersion due to C_{J}.

Assuming that $a_{\mathrm{i}}(0) = 0$, *i.e.* that initially there is no idler, the solution to Equations (2.31a) and (2.31b) is then shown to be

$$a_{\mathrm{s}}(x) = a_{\mathrm{s}}(0)\left(\cosh(gx) - \frac{\mathrm{i}\Delta k}{2g}\sinh(gx)\right)\mathrm{e}^{\mathrm{i}\Delta kx/2} \tag{2.32}$$

where the gain coefficient g is given by

$$g = \sqrt{\kappa_{\mathrm{s}}\bar{\kappa}_{\mathrm{i}} - (\Delta k/2)^2}. \tag{2.33}$$

For perfect phase matching $\Delta k = 0$ we get that

$$a_{\mathrm{s}}(x) = a_{\mathrm{s}}(0)\cosh(gx) \xrightarrow{x \gg 0} \frac{1}{2}a_{\mathrm{s}}(0)\mathrm{e}^{gx}, \tag{2.34}$$

i.e. the gain scales exponentially with length. By studying Equation (2.33) we see that for increasing phase mismatch Δk the gain coefficient g decreases, and in Equation (2.30h) we see that for increasing pump power, the phase mismatch increases.

This is why we use the RPM resonators. As mentioned in Section 2.4.2, using the resonators the dispersion relation just below the resonance frequency diverges, hence by using a pump frequency in this region we can give the pump wave vector the increase for the phase mismatch to be close to zero and thereby enable exponential gain. The full derivation is once again found in Reference [12], while a summary is presented here. By introducing the cutoff frequency $\omega_0 = (L_{\mathrm{J}0}C_g)^{-\frac{1}{2}}$ together with the impedances $C_{\mathrm{c}}, L_{\mathrm{r}}, C_{\mathrm{r}}$ shown in Figure 2.13 on page 2-13, we get that the wave vector now can be approximated by

$$(k_j a)^2 \approx \left(\frac{\omega_j}{\omega_0}\right)^2 + \frac{\omega_j^2 L_{\mathrm{J}0}C_{\mathrm{c}}(1 - \omega_j^2 L_{\mathrm{r}}C_{\mathrm{r}})}{1 - \omega_j^2 L_{\mathrm{r}}(C_{\mathrm{r}} + C_{\mathrm{c}})} \tag{2.35}$$

which for certain pump frequencies and pump powers may make the phase mismatch small enough to get exponential gain.

3

Methods

In this chapter all the methods used throughout this thesis are described. Firstly there is a section about cryogenic measurements, where the cryogenic setup is described. Then there is a section about CAD designs, *i.e.* the designs used to mount and thermalise the components. Then the methods to characterise a qubit are described and finally the section describing the characterisation methods for the JTWPA. Even though the section about the JTWPA characterisation is the most central one for this thesis, the others are also necessary in order to get the whole picture and to understand the JTWPA characterisation section.

3.1 Cryogenic measurements

Qubits and the JTWPA need to be operated at cryogenic temperatures ($T \ll 1\,\mathrm{K}$). Therefore all experiments were performed in a dilution refrigerator, with a base temperature ~ 10 mK. The refrigerator is made of multiple stages with different temperatures, successively reaching the base temperature at the lowest stage, see Figure 3.1. The input signals all enter at room temperature and continue to the 50 K-stage, then go down to a 3 K-stage, then to the still at ~ 800 mK, then via the "cold plate" at ~ 100 mK and then finally reach the mixing chamber at ~ 10 mK. At and between the stages there are attenuators. The high temperature plates ($\geq 3\,\mathrm{K}$) are cooled using a pulse tube while the low temperature stages get their cooling power from helium-3-helium-4-dilution refrigeration, as described in Section 1.4. At the mixing chamber there might be filters, isolators and switches, depending on the setup, before the signals finally reach their experimental setups respectively. Once the signals have passed their respective experimental setup there might be more isolators, filters, *etc.* (not shown in the figure) while travelling back through the stages to room temperature again. At the 3 K plate they encounter a low-noise amplifier using a HEMT[1] amplifier which amplifies the signals before they exit the cryostat and reach room temperature amplifiers.

---

[1] High Electron Mobility Transistor.

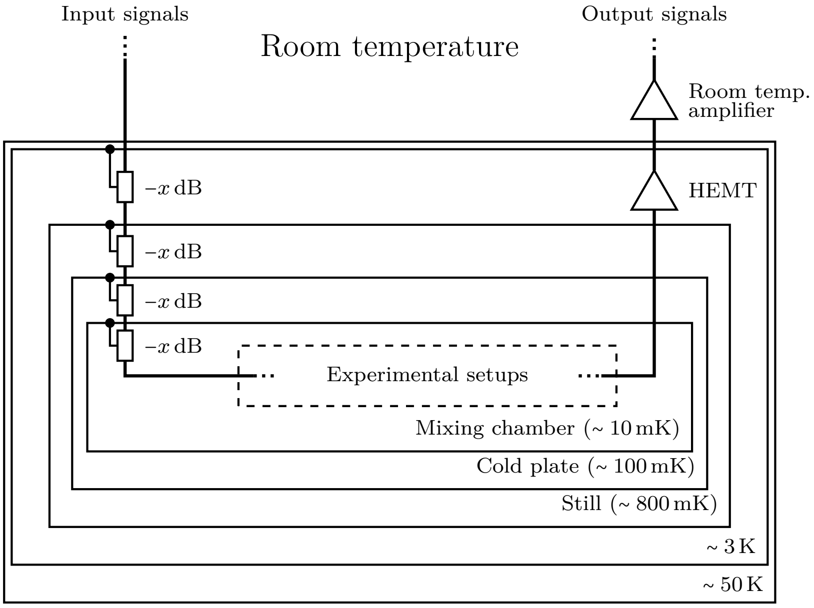

Figure 3.1: A simple schematic of the levels of the dilution refrigerator. Multiple signals, here marked by the thick line, travel down through attenuators, which are thermally anchored in the different stages, to the mixing chamber where the experimental setups are placed. These setups might include some filters,isolators, cryogenic switches, *etc.* The output signals from the setups then travel back up to room temperature and are amplified by a low-noise HEMT amplifier at the 3 K stage and then amplified at room temperature using room temperature amplifiers.

3.1.1 Magnetic shielding at low temperature

As mentioned in Section 1.2 the critical current of a superconductor, and hence of a Josephson junction, is suppressed by external magnetic fields. And as mentioned in Section 1.3, the characteristic inductance of a Josephson junction is completely determined by its critical current. Therefore, if the JTWPA experiences magnetic flux it will change the inductances of the Josephson junctions which in turn might then affect its performance. To minimise the influence of external magnetic fields the JTWPA was magnetically shielded by being put into a box made of CryoPerm 10®, from MµShield®, which is a material specifically made for magnetic shielding at cryogenic temperatures. Isolators and circulators nearby, which are magnetic by default, were also put into boxes of CryoPerm. While common magnetic shielding gets lower permeability when temperature is decreased, CryoPerm gets higher permeability.

3.2 Design of bracket using CAD

In order to mount the experimental setup[2] onto the mixing chamber the necessary components had to be mounted onto a plate and this plate, the “bracket”, had to have screwing holes matching the ones in the cryostat and the components. This was done by creating a model in Autodesk® Inventor® Professional 2018, see Figure 3.2. Most holes in the design were made elongated, so that the components could be moved around a little if necessary. Then this model was fabricated of OFHC[3] copper, see Figure 3.3.

One problem with this bracket design was that it was longer than the distance between the mixing chamber plate and the cold plate. Therefore it could only be mounted in areas where there was an opening in the cold plate. In order to be able to mount the JTWPA module in any available area on the mixing chamber plate, a new shorter design was made, see Figure 3.4, which was also fabricated. This design fits below the cold plate, and it is less wide than the original bracket (50 mm width instead of 54 mm) and can still carry both JTWPAs. However, the drawback with this design is that the cables now need to be drawn on the sides of the bracket, since all the components now are mounted in a horisontal position rather than a vertical one, effectively making it wider than the original design.

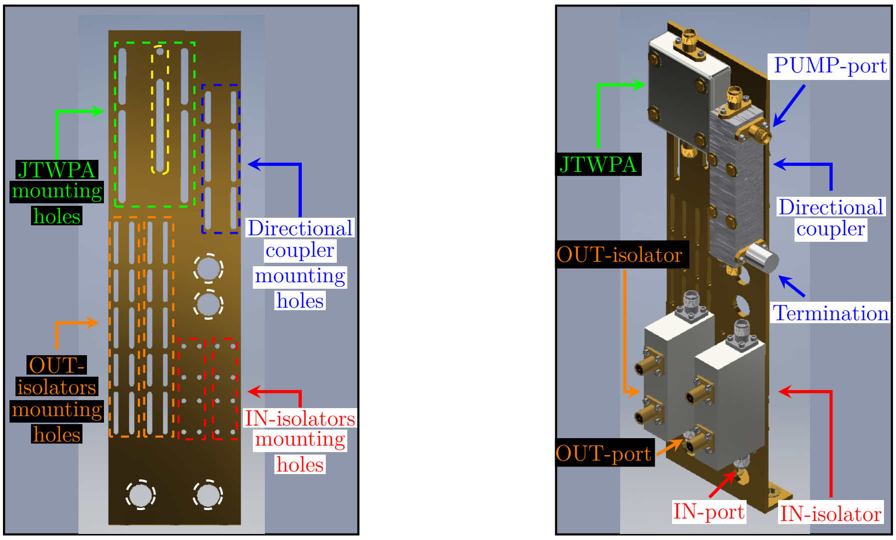

(a) **(b)**

Figure 3.2: The first bracket design of the JTWPA module, designed to be able to carry two JTWPAs in parallel. **(a)** Front of the bracket without components. The white- and yellow-dashed holes were never used for anything. Note that almost all holes are elongated, in order to be able to adjust the position of the components in order to match the cable lengths. **(b)** The bracket with the components for one JTWPA line.

---

[2] The experimental setup itself is shown in Section 3.4.

[3] Oxygen-Free High thermal Conductivity

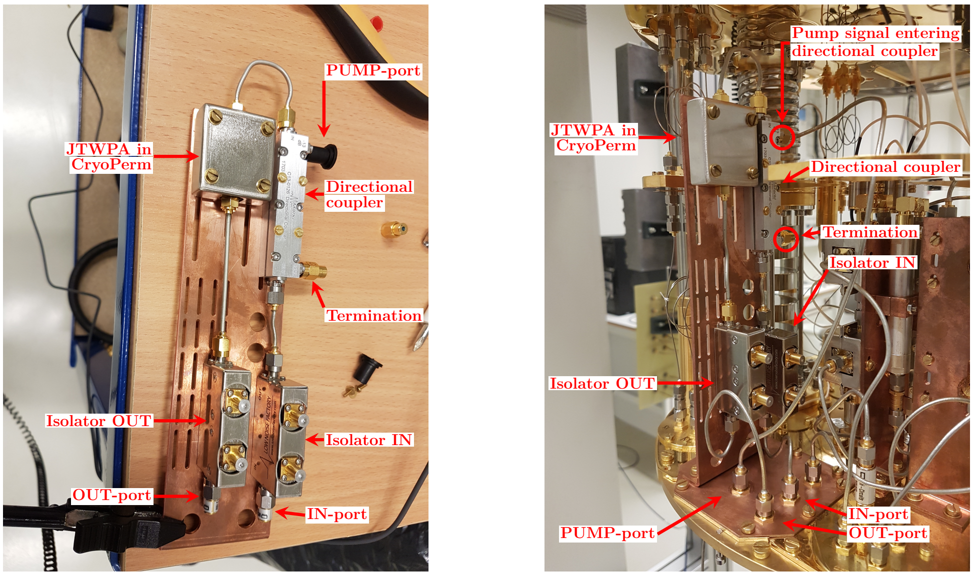

(a) **(b)**

Figure 3.3: **(a)** The JTWPA module, *i.e.* the JTWPA with all the components necessary to use it mounted on the bracket. **(b)** The JTWPA module mounted into the dilution refrigerator.

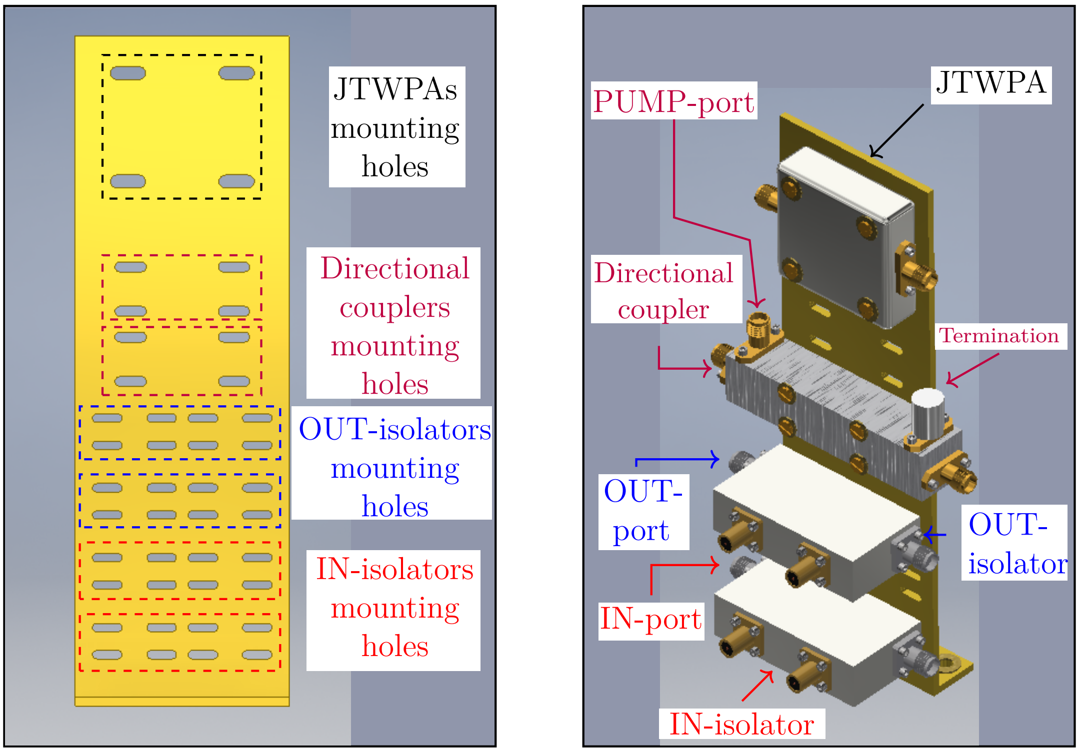

(a) **(b)**

Figure 3.4: The second bracket design of the JTWPA module, also designed to be able to carry two JTWPAs in parallel. **(a)** Front of the bracket without components. Note that all holes are elongated, in order to be able to adjust the position of the components in order to match the cable lengths. **(b)** The bracket with the components for one JTWPA line.

3.3 Characterisation of qubit

We used a qubit to measure the system noise temperature and the quantum efficiency of the JTWPA, but first, the qubit needs to be characterised itself. The methods for characterising the qubit are described below. The theory necessary to understand this characterisation is described in Section 2.2 on page 2-5.

3.3.1 To determine the ground state resonator frequency

As a first step to characterise and calibrate a qubit, we want to find the resonance frequency of the resonator $f_r = \omega_r/(2\pi)$ when the qubit is in the ground state. This is done by connecting a VNA[4] to the IN- and OUT-ports to the qubit feed line and sweep frequencies in the interval we expect the resonator to be, see Figure 3.5.

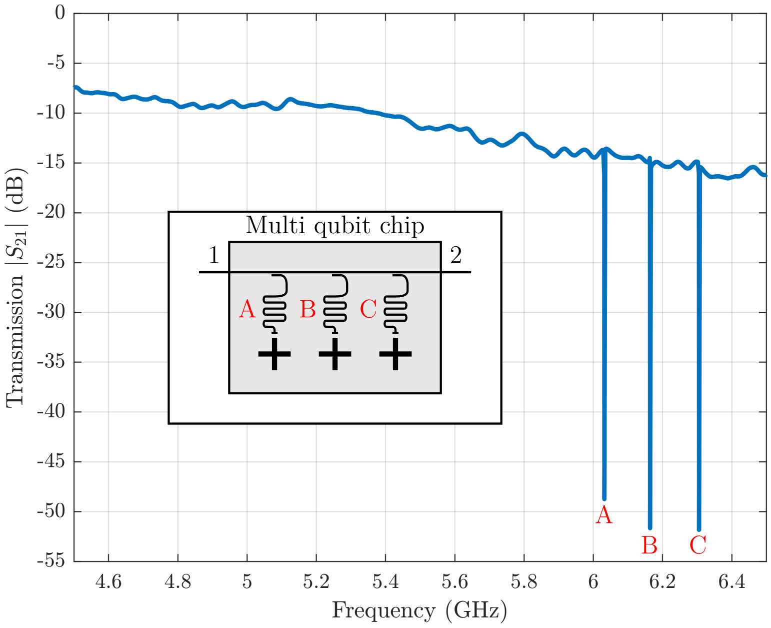

Figure 3.5: A sweep of transmission magnitude of a multi qubit chip with three qubits and resonators. Each of the three dips correspond to one of the resonators.

We know from Section 2.2 that for low power, *i.e.* few photons, the resonance frequency of the resonator will be shifted as described by the dispersive Hamiltonian in Equation (2.10), and this new frequency we call the dressed resonance frequency. For high power, *i.e.* many photons, the approximation for the dispersive Hamiltonian is no longer valid and we will then measure the bare resonance frequency, *i.e.* the resonance frequency of the resonator as if the qubit were not there.

---

[4] A Vector Network Analyser.

Since we do not know whether the frequency found in the transmission sweep in Figure 3.5 is the dressed or the bare resonance frequency, we sweep both power and frequency in a narrow range around the measured resonance frequency, see Figure 3.6. At some power we see a shift in frequency and then we know that the resonance frequency at low power is the dressed resonance frequency, *i.e.* the one we are looking for.

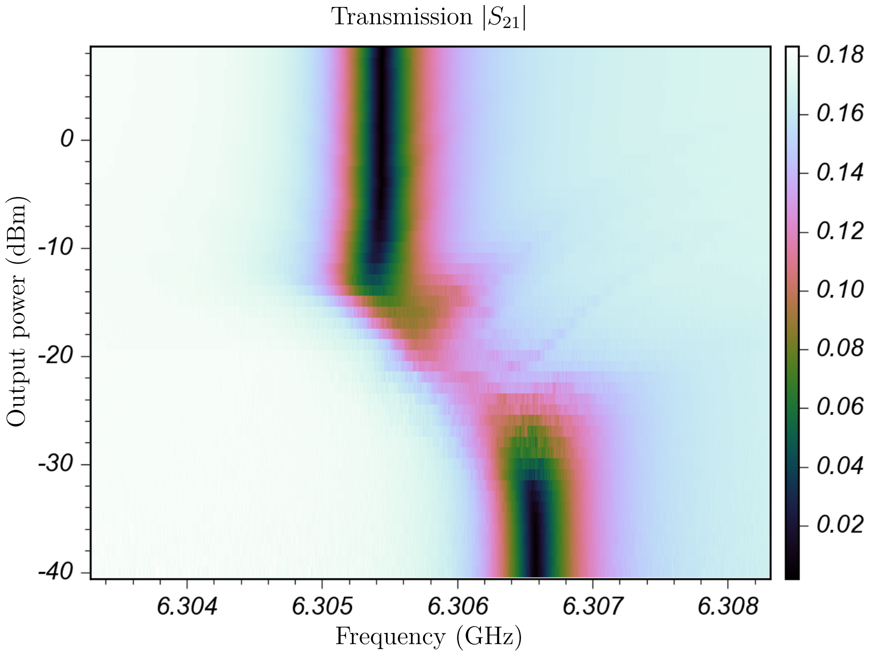

Figure 3.6: Transmission magnitude around the resonator frequency for different resonator powers. Note the shift of frequency between −30 dBm and −15 dBm. Also note that the powers here are the powers at room temperature, which then are attenuated before they reach the mixing chamber and the resonator, by approximately 75 dB.

3.3.2 Up and down conversion of pulses

In order to control and readout a qubit, we will need to be able to send multiple pulses at high frequency (GHz) after each other. To create the pulses we need pulse "up conversion". To readout the response of these pulses once they have interacted with the qubit and the resonator we need pulse "down conversion". The methods to accomplish this are described below.

3.3.2.1 Frequency mixing

The main principle for up and down conversion is frequency mixing, which is depicted in Figure 3.7. A typical mixer takes two signals with the frequencies f_{LO} and f_{IF} and mix them to a signal with the joint envelope of them both with either, or both, of the frequencies $f_{\mathrm{RF}} = |f_{\mathrm{LO}} \pm f_{\mathrm{IF}}|$. This process also works in reverse, where an RF-frequency pulse after mixing with a local oscillator becomes a pulse with a frequency

$f_{\mathrm{IF}} = |f_{\mathrm{LO}} - f_{\mathrm{RF}}|$.

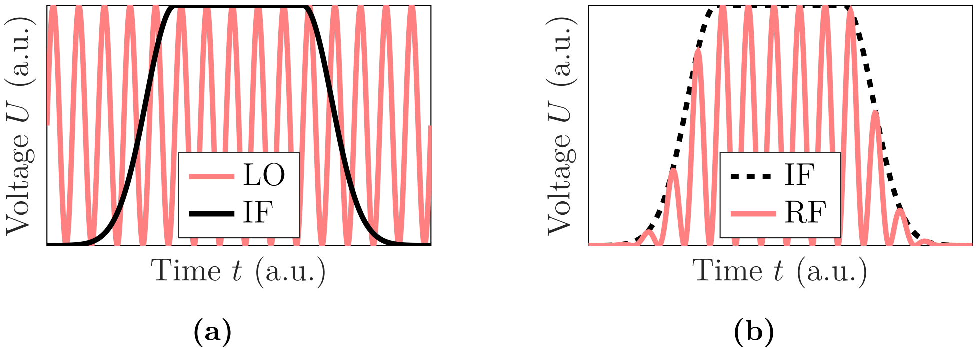

Figure 3.7: Schematics of frequency mixing. **(a)** Two signals enter the RF mixer, a continuous signal with the frequency f_{LO} and a pulse with the frequency f_{IF} (here only its envelope is shown). **(b)** The pulse envelope of the intermediate frequency signal (IF) and the signal output with, depending on the mixer, either or both of the frequencies $f_{\mathrm{RF}} = |f_{\mathrm{LO}} \pm f_{\mathrm{IF}}|$.

3.3.2.2 Up conversion

Microwave generators that directly outputs pulses at GHz frequencies are expensive. Instead we use an AWG[5] which can generate well-defined pulses at MHz frequencies, combined with mixers and local oscillators that can generate continuous GHz signals. Schematics for this are depicted in Figure 3.8.

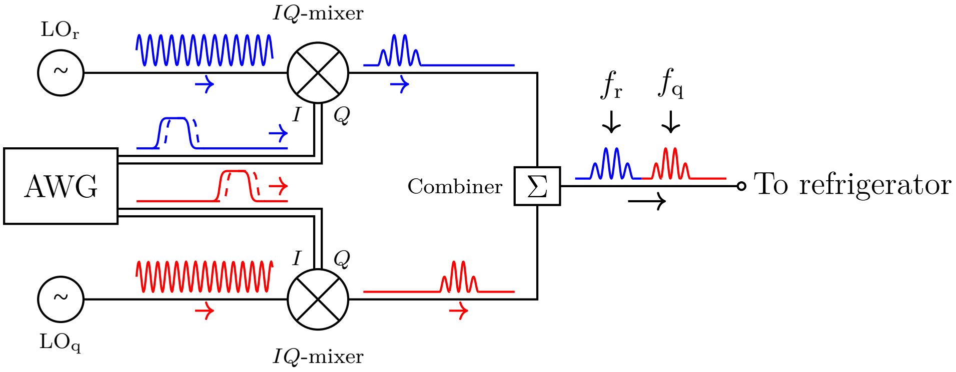

Figure 3.8: Schematics of generating two pulses of different frequencies after each other. Two signal generators generate two continuous signals of the frequencies $f_{\mathrm{LO,r}}, f_{\mathrm{LO,q}}$ and send these signals into one mixer each respectively. An AWG generates two pulses each with an I and a Q component with the frequencies $f_{\mathrm{AWG,r}}, f_{\mathrm{AWG,q}}$ and these pulses also reach each mixer. After the mixing there are two pulses at the frequencies $f_{\mathrm{r}} = f_{\mathrm{LO,r}} - f_{\mathrm{AWG,r}}$ and $f_{\mathrm{q}} = f_{\mathrm{LO,q}} - f_{\mathrm{AWG,q}}$ exiting the mixers. These two pulses reach some kind of combiner where they form a pulse train which is what enters the refrigerator. The IQ-mixers are calibrated such that pulses of other frequencies, such as $f_{\mathrm{LO,q}} + f_{\mathrm{AWG,q}}$, are small.

---

[5] Arbitrary Wave Generator.

3.3.2.3 Down conversion

To convert the output pulse from the refrigerator to a frequency commercial electronics can keep up with we use so called down conversion. This works in the same way as the up conversion process but in reverse, see Figure 3.9. The down converted pulse exits the IQ-mixer as an in-phase pulse (I) and a $\frac{\pi}{2}$ out-of-phase pulse (Q). These pulses go into a digitizer which takes a number of samples of each. Finally, through data processing, these samples are turned into two voltages which we can see as the real and imaginary parts of a complex number.

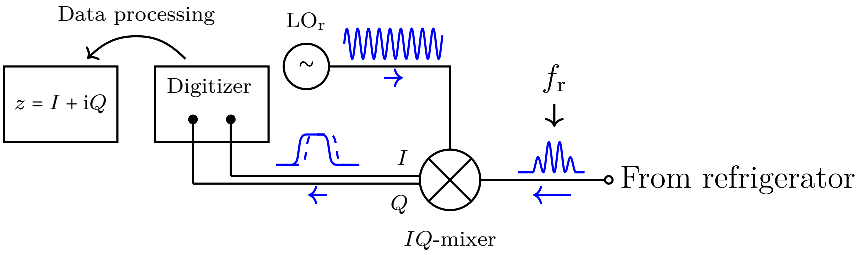

Figure 3.9: Schematics of down conversion of a pulse. The pulse at frequency f_r enters an IQ-mixer and is down-converted into two pulses I and Q, which go into a digitizer. After some data processing these samples are turned into two voltages, which we see as the real and imaginary parts of a complex number.

3.3.3 Calibrating demodulation for optimal readout contrast

Until now, only continuous waves have been used for finding the dressed resonance frequency, and then we do not need to fine-tune the time of sampling the response. In the next step, however, we will start using the pulse setup shown in Figures 3.8 and 3.9. The data processing in the down conversion requires us to sample at the right time, otherwise we will only sample noise.

Study Figure 3.10. Here we see the response in time when a pulse at the resonance frequency is sent. Comparing the two different responses, dependent on the state of the qubit, we see that there is an optimal time for sampling when the difference in response between the qubit states is high. We aim hence to adjust our skip time and sampling time such that the demodulation takes place within the short optimal integration window. An actual measurement of this is shown in Figure 3.11.

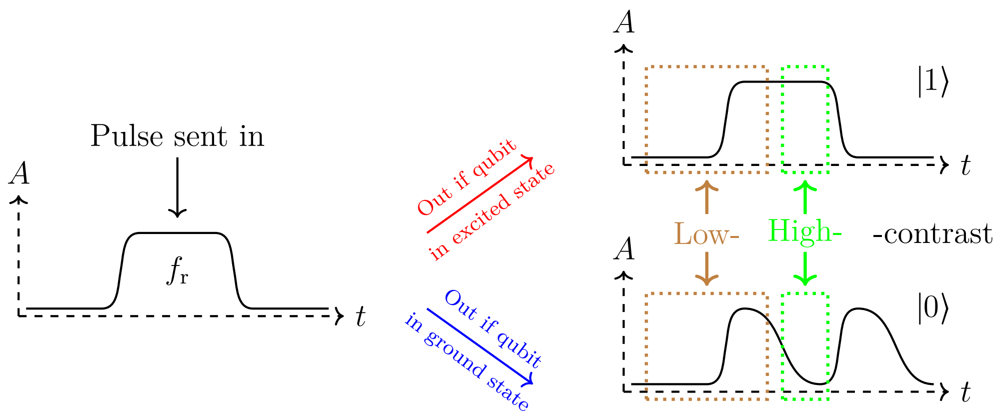

Figure 3.10: Sketch of the envelope of different responses of a pulse at the resonator frequency, depending on the state of the qubit. If the qubit is in the excited and it has shifted the resonator frequency more than a line width, the pulse will be unchanged. If the qubit is in the ground state the pulse will have a dip after a certain time. Note that if we measure what comes out at the time marked "Low contrast" there is almost no difference between the pulses, while if we measure at the time marked "High contrast" there will be a big difference. Since we want as good resolution as possible, we try adjusting the triggers such that we measure at the "High contrast"-time.

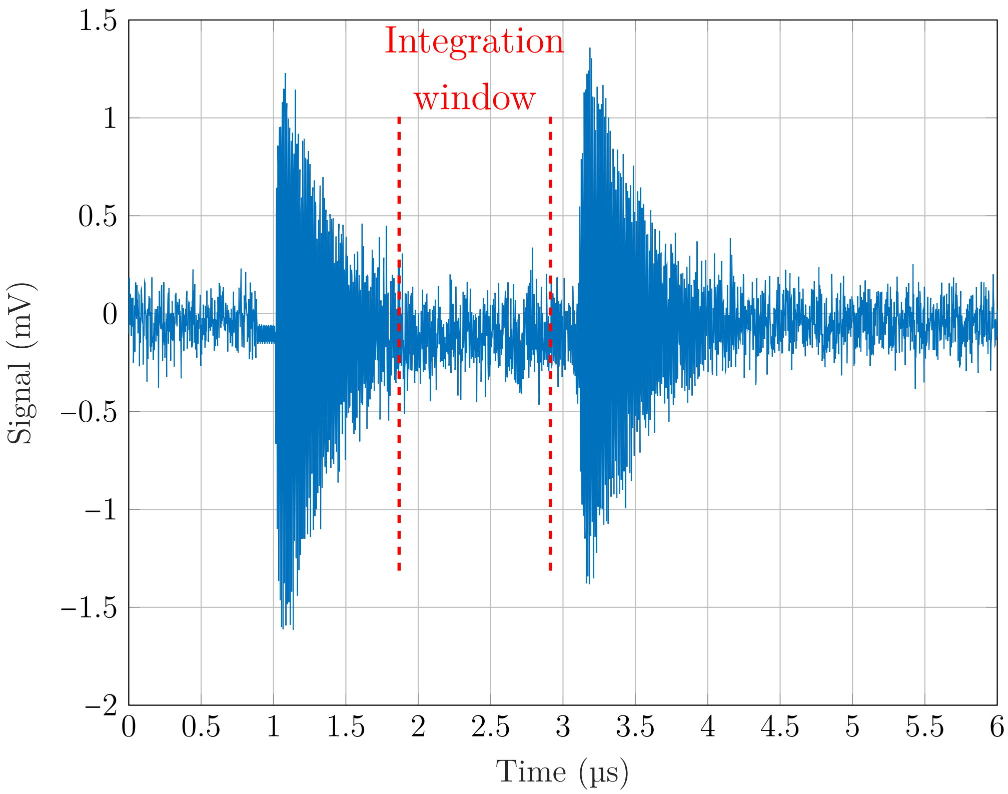

Figure 3.11: The response after sending a 2 µs pulse at the resonance frequency. The period marked "Integration window" is the time where good resolution between the qubit states will be achieved.

3.3.4 Qubit spectroscopy to determine the qubit frequency

Now we know the dressed resonator frequency and we have adjusted the demodulation of the readout pulse to get high resolution between the qubit states. The next step is to find the qubit frequency f_q. We send a pulse at a frequency f and then send a readout pulse to the resonator. If the state of the qubit is changed, the readout response of the resonator will be changed as depicted in Figure 3.10. We sweep f and once $f = f_\mathrm{q}$ we will see a peak, see Figure 3.12.

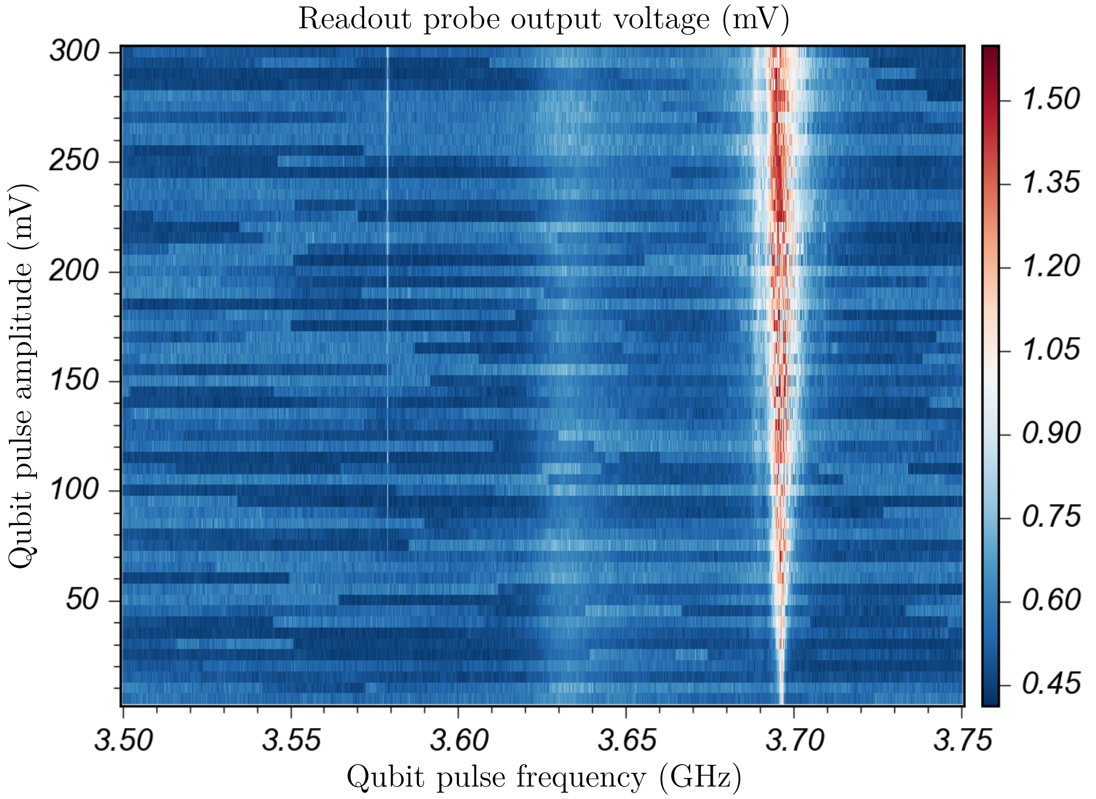

Figure 3.12: Qubit spectroscopy. A long high-amplitude pulse at a frequency f is sent, followed by a calibrated readout pulse. The amplitude and the frequency f are both swept. The frequency of this qubit appears to be around 3.69 GHz. Note that the qubit linewidth broadens the higher the power is. Also note that this figure does not depict the qubit that we used for most measurements, since that qubit had $f_\mathrm{q} \approx 3.64$ GHz.

Since we do not yet know the time and amplitude of a π-pulse we cannot simply excite the qubit with a π-pulse. Instead, we send a long pulse with high amplitude, driving the qubit into a mixed state, and then we take many averages. Thus when $f = f_\mathrm{q}$ the average value will be 50 % excited and we will get a visible peak.

3.3.5 Rabi oscillations to determine the integral of a pi- and pi-half-pulse

Now that we know the dressed resonator frequency f_r and the qubit frequency f_q we want to find a specific pulse corresponding to a π-pulse as described in Section 2.2.2. This is done by sending pulses as shown in Figure 3.13 and sweep the pulse length Δt. Then we will get so called Rabi oscillations, see Figure 3.14, and we know that half the period time of these oscillations correspond to a π-pulse at this specific pulse amplitude. Once it is known we also know that a $\pi/2$-pulse is a pulse of the same length but half the amplitude, since this will give an integral half as big. A pulse of half the plateau time instead of half the amplitude will not correspond exactly to a $\pi/2$-pulse since the pulse is not perfectly rectangular, which is seen by noting that $t_0 \neq t_1$ and $t_2 \neq t_3$ in Figure 3.13. We do not use rectangular pulses in order to reduce other frequency components.

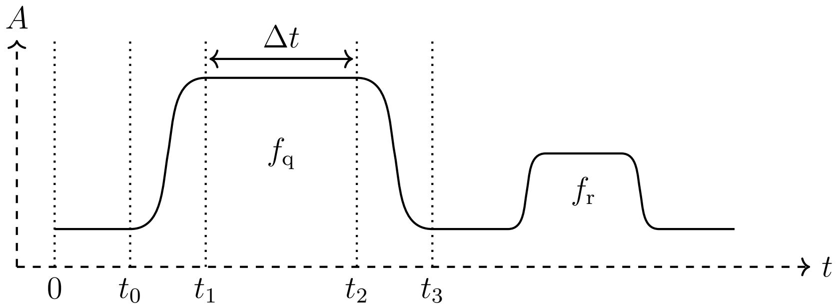

Figure 3.13: Pulse schematics to find the π-pulse. First a pulse at the qubit frequency with some amplitude and a plateau length Δt is sent, followed by a readout pulse. Note that the pulses are not perfectly rectangular but have some rising time, t_0 to t_1, and a descending time, t_2 to t_3. By sweeping the plateau length and averaging over many measurements we will be able to determine the plateau length for a π-pulse.

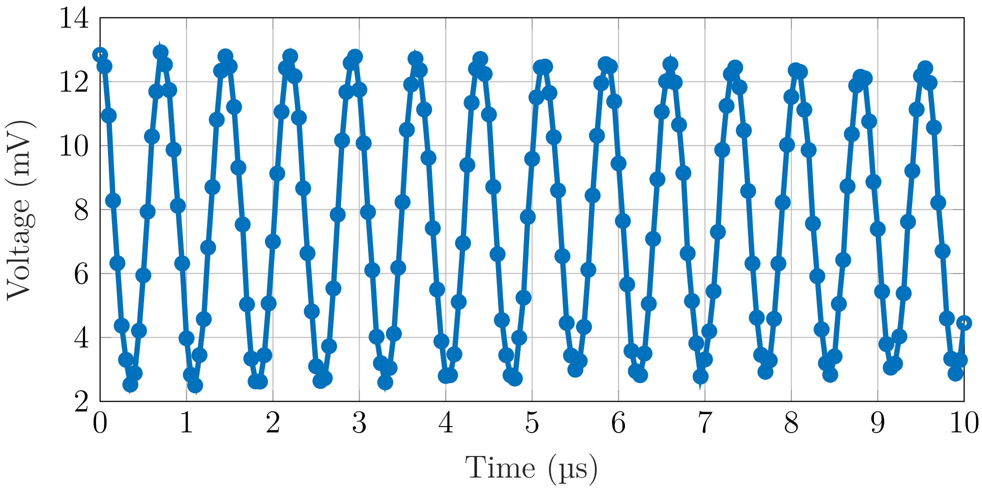

Figure 3.14: Rabi oscillations with a readout pulse at the dressed resonance frequency for an excited qubit, *i.e.* high voltage corresponds to the ground state and low voltage corresponds to the excited state. Note that the period time is about 730 ns, giving us that the time of a π-pulse at this amplitude is $t_\pi \approx 365$ ns.

3.3.6 Ramsey fringes to fine-tune the qubit frequency

The qubit frequency determined in the qubit spectroscopy is approximately the correct one, but may be minimally detuned from the actual qubit frequency. In order to fine-tune the qubit frequency we measure so called Ramsey fringes, see the pulse schematics in Figure 3.15.

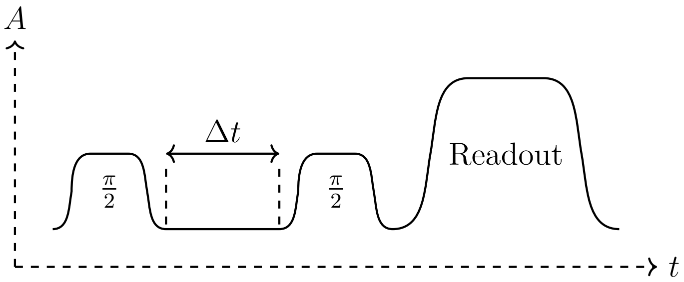

Figure 3.15: The pulse schematics to measure Ramsey fringes. A $\frac{\pi}{2}$-pulse is sent, then we say a time Δt, and then another $\frac{\pi}{2}$-pulse is sent, followed by a readout pulse.

We sweep many different frequencies in a small range around the approximate qubit frequency we determine earlier, and we sweep the pulse separation time Δt, see Figure 3.16. From this measurement we can now determine the qubit frequency very precisely.

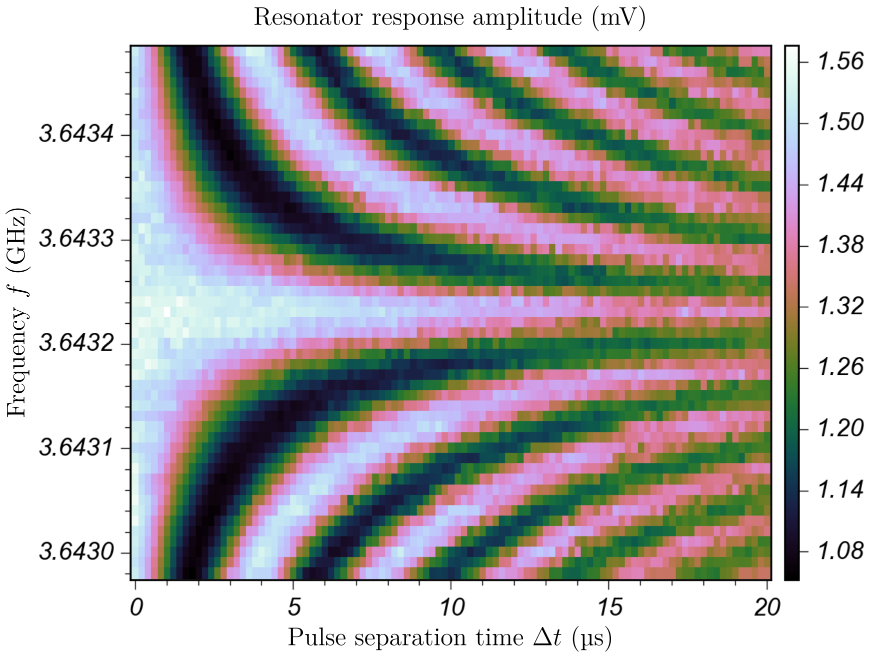

Figure 3.16: Measured Ramsey fringes. From this measurement a very precise qubit frequency can be extracted to be $f_\mathrm{q} = 3.643229\,\mathrm{GHz}$.

One way to determine the qubit frequency is to take a horisontal line cut. We know from theory that the oscillations will oscillate with the same frequency as we are detuned from the qubit frequency, hence we add or subtract the oscillation frequency from the one of the line cut. In theory it is hence enough with one of these line cuts, but due to noise and non-ideal readout we take many separate line cuts and average the frequency they point to.

Another way to determine the qubit frequency is to take a vertical line cut at $\Delta t > 0$. The line cut should then be symmetric around the qubit frequency. Also in this case one line cut should be enough to accurately determine the qubit frequency, but in order to average away noise and non-idealities it is good to take multiple and average the result.

3.3.7 To measure coherence times

A qubit has two characteristic coherence times, the relaxation time T_1 and the decoherence time T_2. When characterising a qubit it is good to determine these for multiple reasons, *e.g.* to know how long your readout pulse can be before relaxation has to be considered.

The decoherence time T_2 we already have enough data to determine at this point. It is simply determined by the exponential decay of the envelope of the Ramsey fringes measurement. It is found by fitting an exponential sinusoidal function to one of the horisontal line cuts of the Ramsey fringes measurement.

The relaxation time T_1 is given by exciting the qubit, wait a time Δt and then readout the state, see Figure 3.17. We sweep the waiting time and fit an exponential to the data, see Figure 3.18. The relaxation time is then given by the fitting constant of the exponent, giving us that $T_1 = 101.3\,\mu s$ and with a 95 % confidence bound in the interval [98.96 µs, 103.6 µs].

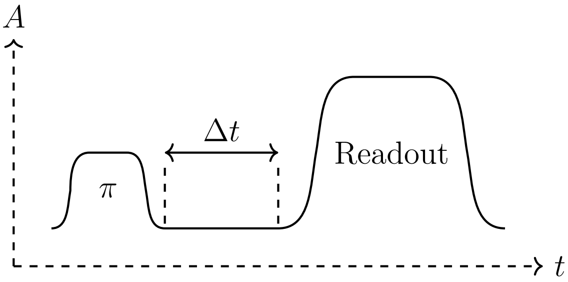

Figure 3.17: Schematics for how to measure T_1. First the qubit is excited, then we wait for a time Δt and then we readout the state of the qubit. The waiting time is swept and then an exponential is fitted to the results, and T_1 is found as the constant of the exponential.

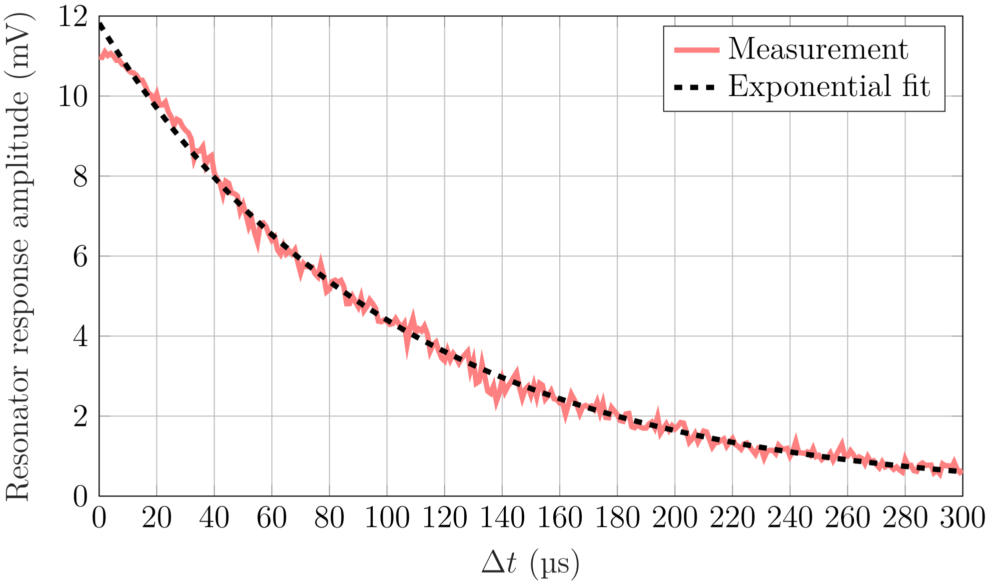

Figure 3.18: Measurement of T_1 as described in Figure 3.17. An exponential is fit to the data from which we extract that $T_1 = 101.3\,\mu s$.

3.3.8 To determine measurement result of a single-shot readout

In the above measurements we use a lot of averages. A single-shot readout is, on the other hand, a readout with no averages. To determine the fidelity, *i.e.* the probability of a correct single-shot readout, we measure the qubit state n_{meas} times without preparing it in any state and n times directly after a π-pulse. The waiting time between each measurement is 1 ms. Since the qubit naturally relaxes to its ground state on a time scale around 100 µs, we assume the qubit is in its ground state at the beginning of each measurement.

We plot each measurement in the IQ-plane and calculate the average value of the ground state measurements and the excited state measurements. Assuming that noise is random, that we do many measurements $n_{\text{meas}} \gg 1$ and that thermal excitations are rare, the average values correspond to the states $|0\rangle$ and $|1\rangle$.

The result of a single-shot readout is defined as which state is the closest to the measured value. The fidelity is determined by counting the number of measurements $n_{a|b}$ that were expected to be in state b but were measured in state a. The fidelity is hence

$$F = \frac{n_{0|0} + n_{1|1}}{2n_{\text{meas}}} = 1 - \frac{n_{0|1} + n_{1|0}}{2n_{\text{meas}}}. \tag{3.1}$$

There are methods for further improving the fidelity calibration, such as heralded state preparation [34], but we have not done any of those in this thesis.

3.3.9 Calibrating the resonator photon number

To further calibrate our qubit-resonator system, we want to calibrate the number of photons in the resonator. This is done in a number of steps described below.

3.3.9.1 To determine the coupling strength

First we measure the transmission with a VNA and extract the real and imaginary parts of the data, see Figure 3.19. Then we use a fitting program, based on the method described in Reference [35], to find a fit to the data, also shown in Figure 3.19. From this fit we can extract the resonator frequency ω_0 and its complex valued quality factor Q_c, amongst others. From these fitting parameters we extract the coupling strength as

$$\kappa = \omega_0 \left|Q_c\right|^{-1} \approx 4.471\,\text{MHz} = 2\pi \cdot 712\,\text{kHz}. \tag{3.2}$$

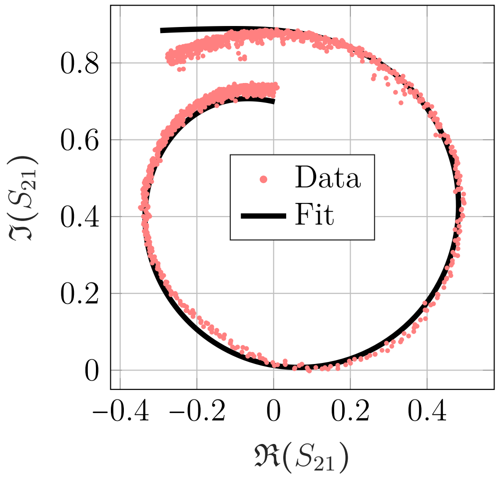

Figure 3.19: The real and imaginary parts of the transmission around the resonator frequency, together with a fit. The fit is based on the method described in Reference [35].

3.3.9.2 To determine the AC Stark shift and the measurement induced dephasing

The next step in our calibration is to determine the AC Stark shift and the measurement induced dephasing. This is done by following the pulse schematics shown in Figure 3.20. In this figure, note that there are two lines with pulses that are sent at the same time. The pulses on the upper line, marked "Qubit", have the frequency $f = f_\mathrm{q} - \delta f$, where δf is some detuning from the qubit frequency. The pulses on the lower line have the same frequency as the readout frequency, f_r.

First a driving pulse to the resonator arrives. After some time, when the resonator ring-up time has passed and the number of photons in the resonator hence is stable, a $\frac{\pi}{2}$-pulse is sent to the qubit. Then we wait some time Δt. Next another $\frac{\pi}{2}$-pulse is sent and finally a readout pulse is sent, and the measured output voltage of the readout pulse is the measurement result. We sweep this for multiple values of Δt. This sequence is then repeated, but with the second qubit pulse replaced with a $-\frac{\pi}{2}$-pulse, in order to get a reference to suppress low frequency noise. We repeat both of these sequences 30 times, in order to be able to average away more noise. Finally we run the whole sequence again, with another value of A_drive. This we do for $A_\mathrm{drive} \in \{0, 2, 4, 6, 8, 10\}\,\mathrm{mV}$.

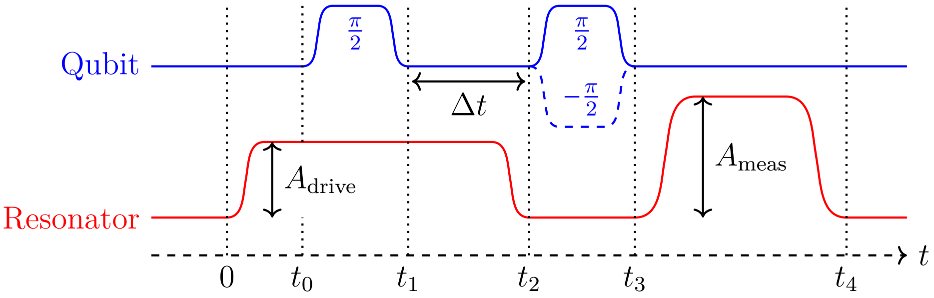

Figure 3.20: Pulse schematics to determine the measurement induced dephasing. At time 0 a drive signal is turned on with a frequency close to the resonator frequency. Then at time t_0 a $\pi/2$-pulse at the qubit frequency is sent. At time t_1 the $\pi/2$-pulse is completed. Then at time t_2, *i.e.* after time Δt, the drive signal is turned off while a $\pi/2$ or a $-\pi/2$-pulse is sent. Finally at time t_3, when the second qubit pulse is completed, a measurement pulse is sent which is completed at time t_4.

When this measurement is done we subtract the reference from the results and take the average from the 30 different measurements for each value of A_{drive}, see Figure 3.21. Then to each of these curves we fit the amplitude of the readout output voltage U to the expression

$$U = A\mathrm{e}^{-\Gamma\Delta t}\sin(\omega\cdot\Delta t+\delta)\,, \tag{3.3}$$

where Δt is the pulse separation as depicted in Figure 3.20 and $\{A,\Gamma,\omega,\delta\}$ are the fitting parameters. The parameter A is the maximum amplitude of the oscillations, Γ the envelope exponential decay constant, ω the oscillation angular frequency and δ a phase shift. The fits are presented in Figure 3.21. From these fits we can then extract the AC Stark shift ω_{ac} and the measurement induced dephasing Γ_φ.

The AC Stark shift is found by the fact that $\omega_{\text{ac}} = 2\pi\delta f-\omega$, where $\delta f = 529\,\text{kHz}$ is the detuning of the qubit pulses from the qubit frequency.

The measurement induced dephasing is found by the fact that $\Gamma_{\varphi,m} = \Gamma-\Gamma_2^*$, where $\Gamma_2^* = T_2^{-1}$ is the decoherence rate we find for $A_{\text{drive}} = 0\,\text{mV}$.

By putting these results together, we can plot the AC Stark shift ω_{ac} and the measurement induced dephasing rate $\Gamma_{\varphi,m}$ as functions of A^2_{drive}, see Figure 3.22.

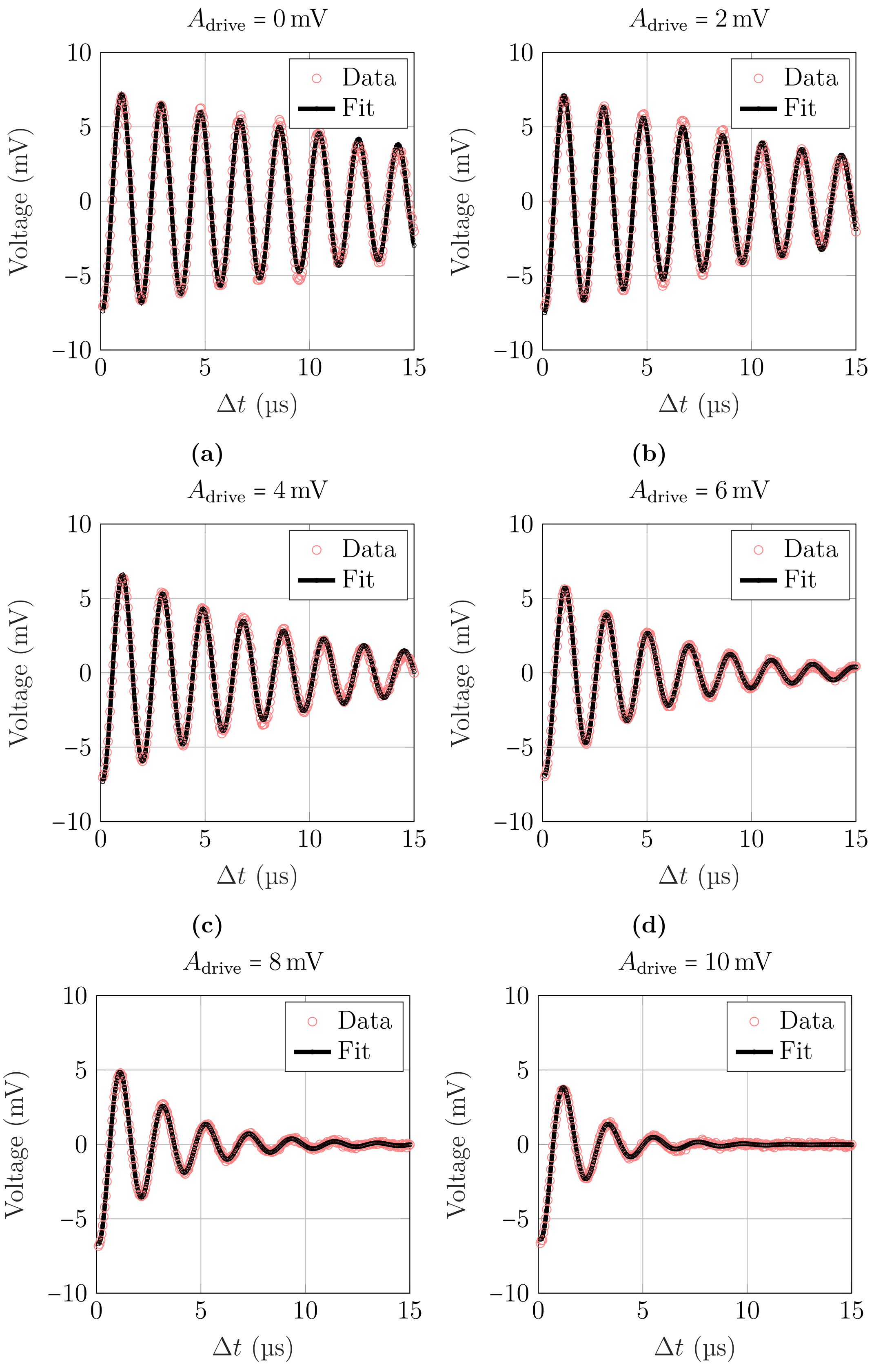

(a) **(b)** **(c)** **(d)** **(e)** **(f)**

Figure 3.21: Ramsey oscillations using a $-\frac{\pi}{2}$-pulse to create a reference, for different amplitudes of A_{drive}, together with a fit of the kind shown in Equation (3.3).

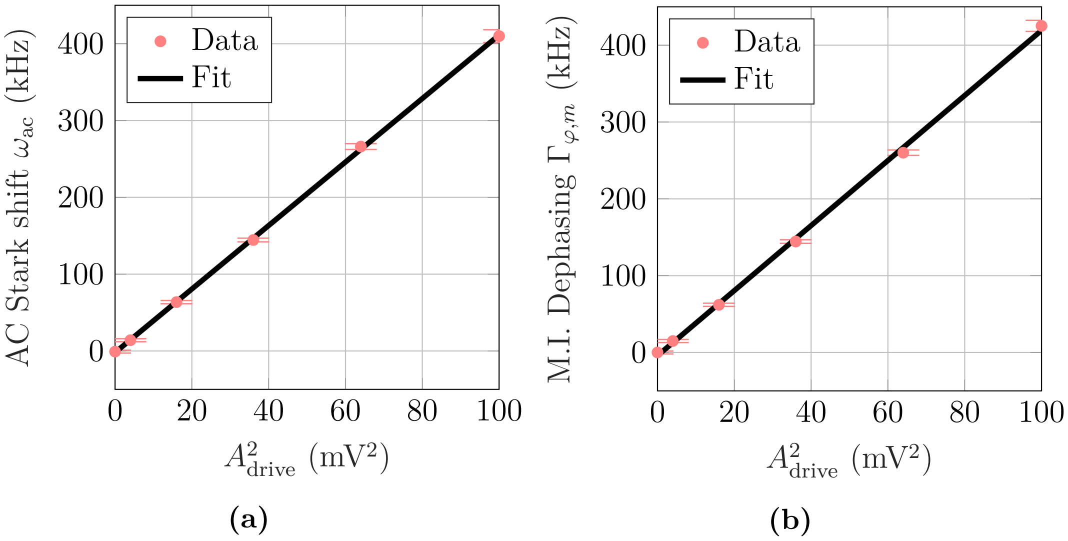

(a) **(b)**

Figure 3.22: The AC Stark shift ω_{ac} and the measurement induced dephasing Γ_φ as functions of A^2_{drive} with 95 % confidence bounds, determined from the fitting of the Ramsey oscillations presented in Figure 3.21, together with linear fits. Both are expressed in angular frequency.

3.3.9.3 To determine the dispersive shift and the photon number

We know from theory [12] that $A^2_{\mathrm{drive}} \propto \bar{P} \propto \bar{n}$, where $\bar{n}$ is the average number of photons in the resonator, for both the AC Stark shift and the measurement induced dephasing. We also know that

$$\omega_{\mathrm{ac}} = 2\chi\bar{n}, \tag{3.4a}$$

$$\Gamma_\varphi = 8\chi^2\bar{n}\kappa^{-1}. \tag{3.4b}$$

Hence by taking the ratio of the slopes of the linear fits we get

$$\frac{m_\varphi}{m_{\mathrm{ac}}} = \frac{8\chi^2\kappa^{-1}}{2\chi} = \frac{4\chi}{\kappa} \approx 1.0246, \tag{3.5}$$

where the m_i are slopes of the fits. This value is with a 95 % confidence bound in the interval [0.965,1.086]. By using this value together with the κ determined in Equation (3.2), we get the dispersive shift

$$\chi \approx 1.0246 \cdot \frac{\kappa}{4} = 1.197\,\mathrm{MHz}. \tag{3.6}$$

Now we can solve Equation (3.4a) for $\bar{n}$ to get the average photon number in the resonator as a function of the AC Stark shift, which is given by the linear fit in Figure 3.22a, see Table 3.1 below.

Table 3.1: Number of photons $\bar{n}$ in the resonator, given the amplitude A_{drive} in mV of the resonator pulse.

A_{drive} (mV)	0	2	4	6	8	10	100
$\bar{n}$	0	0.01	0.03	0.06	0.11	0.17	17.27

3.4 Characterisation of the JTWPA

In this section the methods used for characterising the JTWPA are described. In Figure 3.23 we see the circuit schematics of the JTWPA module, which was used throughout all experiments. Almost all focus has been put on studying the effects of the JTWPA module on the interval 4-8 GHz because most of the HEMT amplifiers and the isolators only work well in this band.

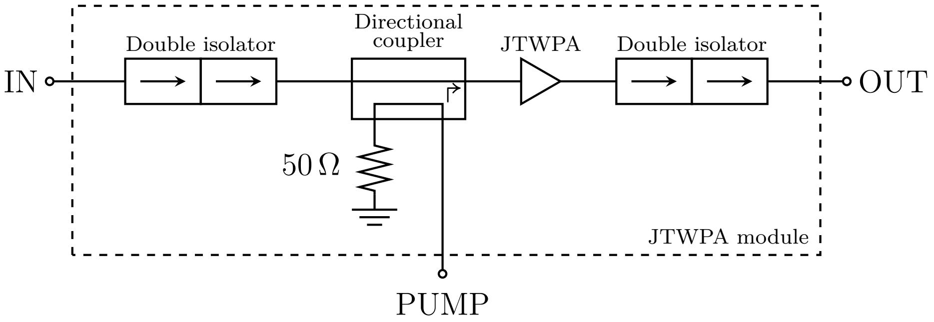

Figure 3.23: Design of the JTWPA module. The signal to amplify enters at the IN-port, goes through a double isolator, couples with the pump when going through the directional coupler, enters the JTWPA and is amplified and finally goes through another double isolator to the OUT-port. The first double isolator prevents reflections at the JTWPA and the backwards-travelling pump signal (due to finite directivity in the directional coupler) to enter the sample. The last double isolator mainly blocks heat radiation from higher stages entering the JTWPA module.

3.4.1 Characterisation of the JTWPA module components

In order to better understand how the JTWPA module circuit works it would help to characterise each component and each cable, measure the reflection, insertion loss and other properties. But since the properties of materials are not the same at room temperature as at cryogenic temperatures, these characterisation measurements would need to be performed in the cryostat when it is cold. This was not done however, since it then would require a separate cool down which would take a lot of both space in the cryostat, preventing others from doing other experiments, and also time from other measurements. Instead focus was put on characterising the JTWPA module as a whole and see how it works as an amplifier circuit.

3.4.2 Basic determination of the pump region

The first step of characterising the JTWPA is to identify in what region the parameters of the pump, the pump frequency and the pump power, should be in order for the JTWPA to be able to amplify. The steps of doing this are described below.

3.4.2.1 Use of cable through for background correction

The JTWPA is connected into a circuit, the "JTWPA module", as depicted in Figure 3.23. Then the JTWPA module is connected in parallel with a through line as depicted in Figure 3.24. A signal generator is connected to the PUMP-port and a VNA is connected to the IN- and OUT-ports in order to measure the S_{21}-parameter. From the VNA and the signal generator down to the JTWPA module, there multiple attenuators as depicted in Figure 3.1. For a full overview of the complete setup, see Figure A.2 on page A-2.

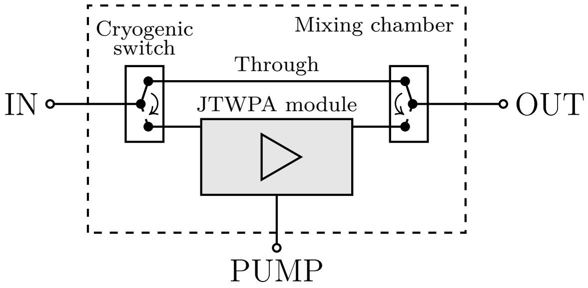

Figure 3.24: The experimental setup in the dilution refrigerator for characterisation of the JTWPA module gain. The JTWPA module, depicted in Figure 3.23, is put in parallel with a line through, in order to measure gain over the JTWPA module compared with not having it there at all.

In the whole setup there are multiple components. There are components at room temperature, at the different stages in the cryostat, *etc*, and every part has its own noise temperature and insertion loss. The whole setup except for the actual experimental setup is referred to as the background. If the gain was calculated by comparing what signal we send down to the JTWPA module with what comes out of the cryostat, the result would be very misleading since the background attenuation, the amplification and noise would then be included in the results.

To correct for the background we use a cable through, as depicted in Figure 3.24, in parallel with the JTWPA module. In this way we can get a reference measurement which we can put as zero gain. Then we can see if and how much the JTWPA module actually amplifies, the "effective gain", by taking the subtraction

$$G_{\text{eff}} = S_{21}^{\text{Pump on}} - S_{21}^{\text{Through}}, \quad \text{(dB)} \tag{3.7}$$

where $S_{21}^{\text{Pump on}}$ is the transmission through the JTWPA module in dB with the pump on and S_{21}^{Through} is the transmission through the cable through in dB, not to be confused with the parametric gain, which is given by

$$G_{\text{par}} = S_{21}^{\text{Pump on}} - S_{21}^{\text{Pump off}}, \quad \text{(dB)} \tag{3.8}$$

where $S_{21}^{\text{Pump off}}$ is the transmission through the JTWPA module in dB without using a pump. The difference between effective and parametric gain is hence that effective gain is the gain compared with not using the amplifier at all, while parametric gain is the gain the amplifier circuit, the JTWPA module, gives relative to its own insertion loss.

3.4.2.2 Determination of the insertion loss and pump frequency region

In order to get a reference to the background for all measurements, the transmission through the cable through was compared with the transmission through the JTWPA module when there was no pump signal, see Figure 3.25.

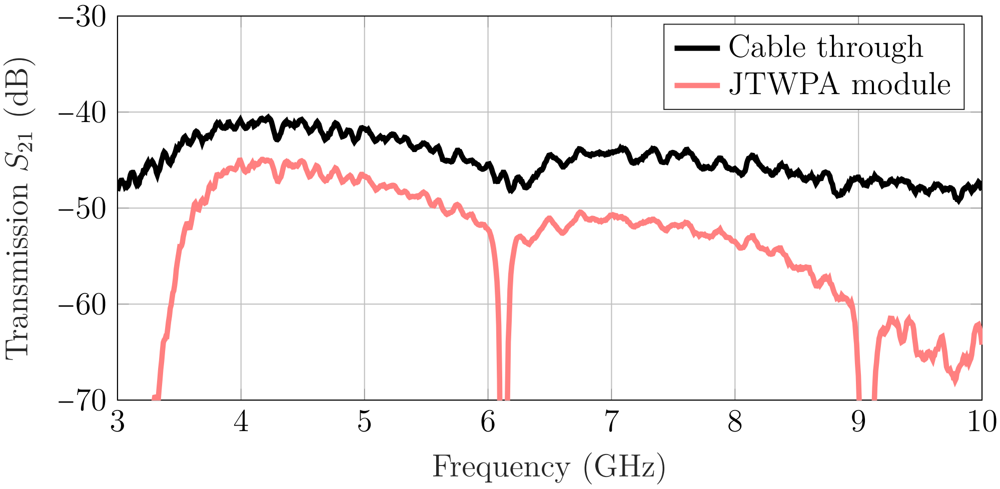

Figure 3.25: Measurement of the transmission, S_{21}, through the JTWPA module compared with the transmission through the cable through. Note the reduced transmission at the dispersive regime, just above 6 GHz. Note also the other transmission reduction at 9 GHz, for which the explanation remains unknown.

By subtracting the transmission through the cable through from the JTWPA module transmission we then find the insertion loss of the JTWPA module, see Figure 3.26. By studying the insertion loss we find that the dispersive feature is around 6.1 GHz and thereby that the pump frequency should be set to around 6.05 GHz. Disregarding the dispersive feature, the JTWPA module insertion loss in dB is approximately linear with respect to frequency. A linear fit gives us that the insertion loss L in dB at frequency f in GHz is well approximated by

$$L = 0.91f + 0.4 \pm 0.25. \tag{3.9}$$

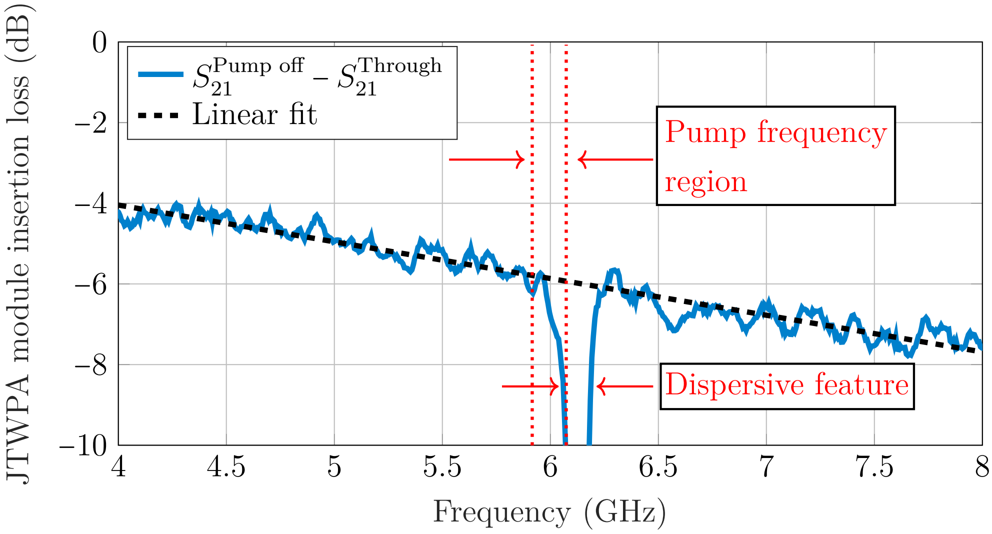

Figure 3.26: The insertion loss of the JTWPA, calculated as the transmission through the JTWPA without a pump minus the transmission through the cable through. The dispersive feature is identified by heavy losses, since the resonators of the JTWPA work as a band-stop filter there, and the region for where the optimal pump frequency is expected to be slightly below that.

3.4.2.3 Determination of pump power interval

While fixing the pump frequency to 6.05 GHz, we increase the pump power from low powers of −70 dBm at the JTWPA module PUMP-port, which corresponds to approximately −83 dBm at the chip[6], and increase the power until we get gain. At approximately $P_{\text{p}} = -55\,\text{dBm}$ we start seeing gain. At −52 dBm we have reached a pretty stable gain profile with a wide band with ≥ 10 dB gain, and at approximately −48 dBm we no longer have any gain, see Figure 3.27.

By calculating the average gain in dB, given by

$$G_{\text{avg}}(\text{interval}) = \langle G_{\text{eff}}(\text{interval})[\text{in dB}] \rangle\,, \tag{3.10}$$

where the interval may be the whole frequency interval 4-8 GHz or a smaller interval, we get a clear figure showing what the pump power should be, see Figure 3.28. Therefore we conclude that we the optimal pump power roughly should be in the interval −55 dBm to −48 dBm at the JTWPA module pump input port.

---

[6] We get 13 dB attenuation from the directional coupler.

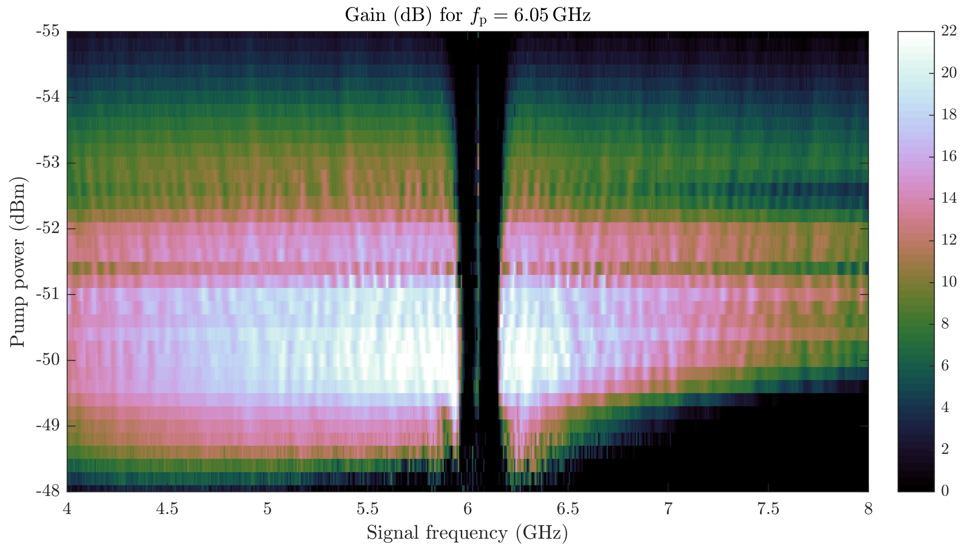

Figure 3.27: Gain profiles for a fixed pump frequency $f_\mathrm{p} = 6.05\,\mathrm{GHz}$ and different pump powers. Note that for high powers, noticeable in this figure from $-49.6\,\mathrm{dBm}$, the gain quickly drops for signal frequencies above the stopband. Meanwhile higher powers, like $-48.4\,\mathrm{dBm}$, are required for the gain for frequencies below the stopband to drop heavily.

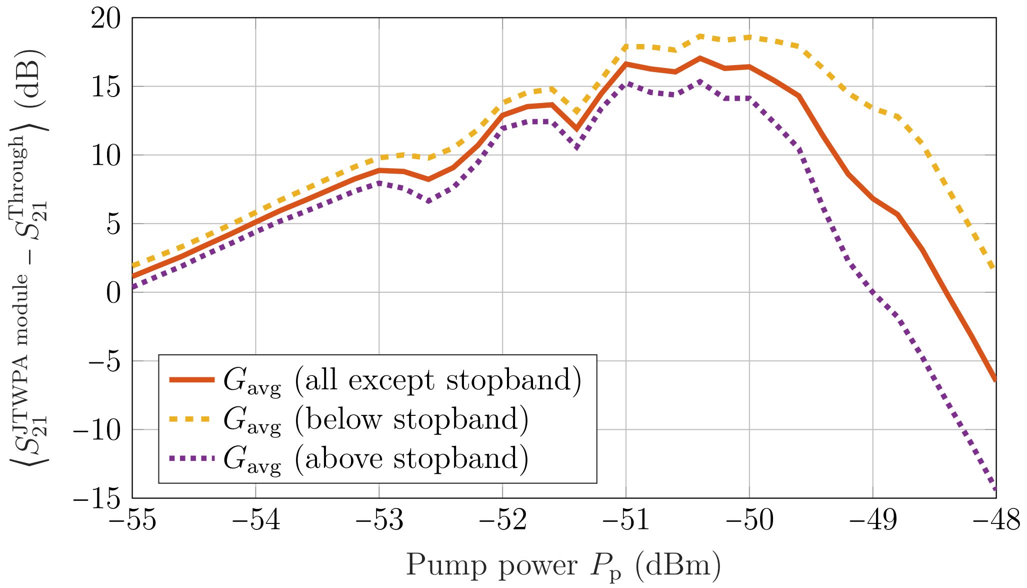

Figure 3.28: The average effective gain in dB, defined as the average difference $S_{21}^{\text{JTWPA module}} - S_{21}^{\text{Through}}$ in dB on a given interval, for a pump of frequency 6.05 GHz at different pump powers. The intervals studied are the whole interval 4-8 GHz (ignoring the stopband), the region below the stopband, and the region above the stopband. We can see that at $P_\mathrm{p} = -55\,\mathrm{dBm}$ we start getting gain but at $P_\mathrm{p} = -48\,\mathrm{dBm}$ we have lost almost all gain even for the frequency interval below the stopband, which tends to be higher than the frequencies above the stopband.

3.4.3 Characterisation of the gain profiles and determination of the optimal pump parameters

To characterise different gain profiles the same setup as above was used. Now we know that the optimal pump frequency is around 6.05 GHz and that the optimal pump power is in the interval −55 to −48 dBm, but since we do not know the exact parameter values of the JTWPA[7] what pump powers and pump frequencies are expected to be the optimal ones. Therefore we sweep both pump power and pump frequency in their relevant intervals respectively and measure the gain profile. After a few simple tests, in order to not sweep unnecessary frequencies, the pump frequency was chosen to be swept in the interval 5.95 GHz to 6.1 GHz. Using frequency steps of 1 MHz and power steps of 0.2 dB, this results in 151 × 36 = 5436 different gain profiles.

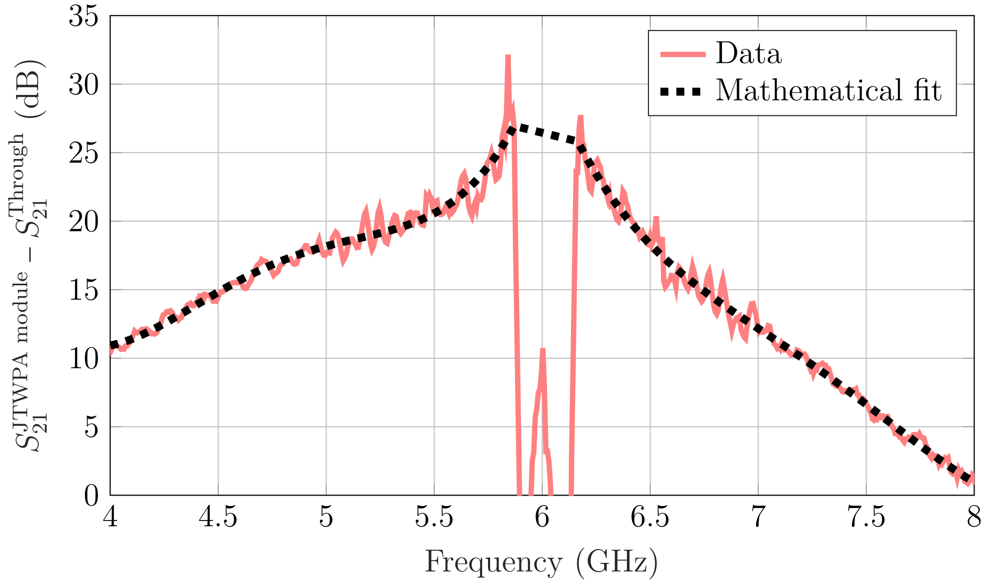

Figure 3.29: Gain profile with mathematical fit. The data is the S_{21}-values of the JTWPA module minus the S_{21}-values of the cable through, *i.e.* the effective gain, for a pump of frequency $f_\mathrm{p} = 6.009\,\mathrm{GHz}$ and power $P_\mathrm{p} = -50.2\,\mathrm{dBm}$. To each side of the stopband a 4th degree polynomial was fitted in order to determine gain bandwidths and the ripple level. Note that the stopband simply is ignored when fitting the curves.

To evaluate all the measured gain profiles in a systematic way a characterisation protocol is followed for each gain profile in the following manner: First the stopband is identified[8] and ignored since the amplifier does not work in that region. Then to each side of it a 4th degree polynomial is fitted[9]. Next these two polynomials are put together as one function and we define the bandwidth BW_x for $x\,\mathrm{dB}$ gain

---

[7] The characteristic values $C_g, C_\mathrm{c}, C_\mathrm{r}, L_\mathrm{r}, I_\mathrm{c}$ as depicted in Figure 2.13.

[8] The stopband is identified based on the theory described in Section 2.4.2.

[9] Note that there is nothing physical about 4th degree polynomials. These fits were only done in order to determine the ripple level and bandwidth of the gain profiles.

to be the width of the interval when this function is above x dB[10]. We define the ripple value to be the square root of the sum of all quadratic distances from the fitted curve, *i.e.* a value similar to the variance, which then gives us a number on the smoothness of a curve. Finally, since this definition of the bandwidth includes the stopband but the size of the stopband is different for different pump frequencies, we define the effective bandwidth $BW_{x,\mathrm{eff}}$ for x dB gain to be the bandwidth minus the width of the stopband.

An example of this can be seen in Figure 3.29. In this figure we see that we have a gain larger than 15 dB from approximately 4.5 GHz all the way to 6.75 GHz, giving us a bandwidth for 15 dB gain BW_{15} = 6.75 GHz – 4.5 GHz = 2.7 GHz. The stopband for this profile reaches from 5.87 GHz to 6.16 GHz, giving us a stop-bandwidth of 0.29 GHz resulting in an effective bandwidth for 15 dB gain of $BW_{15,\mathrm{eff}}$ = 2.7 GHz – 0.29 GHz = 2.41 GHz.

The results of the gain profile analysis are presented in Section 4.1 on page 4-1.

3.4.4 To determine the saturation power

The saturation power, also known as the 1 dB compression point, is defined as the signal power where the gain is decreased by 1 dB. It is measured by fixing the pump frequency and pump power and then measure the gain profile for different signal powers P_s over the whole JTWPA module interval. Then the saturation power, at a specific signal frequency f_s, on the whole JTWPA module interval 4-8 GHz or on a smaller interval, *e.g.* 4-5 GHz, is extracted by simply identifying the signal power P_s for which the gain is 1 dB below the maximum gain.

3.4.5 Measurement of Signal-to-Noise Ratio improvement

Once the gain profiles are measured the next step is to measure the Signal-to-Noise Ratio improvement (ΔSNR), *i.e.* to determine how much better the Signal-to-Noise Ratio (SNR) becomes when using the JTWPA, or in other words, how much more the JTWPA module can amplify the signal compared with how much it amplifies the noise. The ΔSNR most certainly differs at different frequencies, since the JTWPA module amplifies differently at different frequencies, therefore we measure the ΔSNR at 36 different frequencies spread on the whole band 4 to 8 GHz, namely the frequencies 4 - 5.7 GHz and 6.3 - 8 GHz with steps of 100 MHz.

For the ΔSNR characterisation the same setup as above is used, except that an RF-source is connected to the IN-port and a spectrum analyser to the OUT-port. Using this setup we can measure the ΔSNR of the JTWPA module at a given frequency, using the method described below.

---

[10] This definition of bandwidth and the reason for using it will be explained in Chapter 5.

3.4.5.1 To determine Signal-to-Noise Ratio

The SNR is determined by first sending a signal at a frequency f_s and sweep the spectrum with the spectrum analyser in a narrow range of 500 kHz around this frequency, *i.e.* $f \in [f_\mathrm{s} - 250\,\mathrm{kHz}, f_\mathrm{s} + 250\,\mathrm{kHz}]$. Then the signal strength is defined as the value in the middle of this interval and the noise floor is defined as the average value of the rest of the data points, *i.e.* the average excluding the signal. Finally the SNR, in dB, is defined as the signal strength minus the noise floor, see Figure 3.30.

3.4.5.2 To determine a reference

Just as when determining the effective gain, we need to measure the SNR using a through line in order to get a reference for when using the JTWPA. Since the SNR may vary with frequency, we measure the SNR with the through at all the 36 frequencies. We also measure this with the JTWPA module switched in but with pump off, so that we can compare the parametric ΔSNR with the effective ΔSNR.

3.4.5.3 To determine ΔSNR for a specific pump

To determine the ΔSNR for a specific JTWPA pump, we measure the SNR using the JTWPA with this pump, and then we subtract the SNR of the through at the same frequency. For example in Figure 3.31 a pump with $f_\mathrm{p} = 6.058\,\mathrm{GHz}$ and $P_\mathrm{p} = -52.6\,\mathrm{dBm}$ is used and the SNR is 54 dB. Using the through, the SNR is 45 dB, recall Figure 3.30. The ΔSNR for this pump at this frequency is hence $54\,\mathrm{dB} - 45\,\mathrm{dB} = 9\,\mathrm{dB}$.

3.4.5.4 To determine ΔSNR over the whole band

Finally we want to measure the ΔSNR over the whole band 4 - 8 GHz, at many different frequencies and for many different pumps to see if we can find a pump that gives high ΔSNR at all frequencies.

Given the results from the gain characterisation we know that gain drops quickly for pump frequencies above 6.08 GHz, hence we limit ourselves to the pump frequencies 5.95 GHz to 6.08 GHz. We begin with a small range of pump powers around the pump region of maximum gain, but realise soon that a bigger interval is needed because the ΔSNR tends to be higher for pump powers lower than the ones for maximal gain[11].

In the end we sweep the pump power interval −53.5 dBm to −49.5 dBm with 0.1 dB steps, pump frequencies 5.95 GHz to 6.08 GHz with steps of 1 MHz and signal fre-

---

[11] Possibly because at high pump powers some junctions turn normal and add extra noise photons.

quencies 4 GHz - 5.7 GHz and 6.3 GHz - 8 GHz. We skip measuring the ΔSNR in the interval 5.8 GHz to 6.2 GHz since the stopband is approximately in this region.

The most significant ΔSNR results are presented Section 4.2 on page 4-5, while all the ΔSNR data is presented in Appendix B.

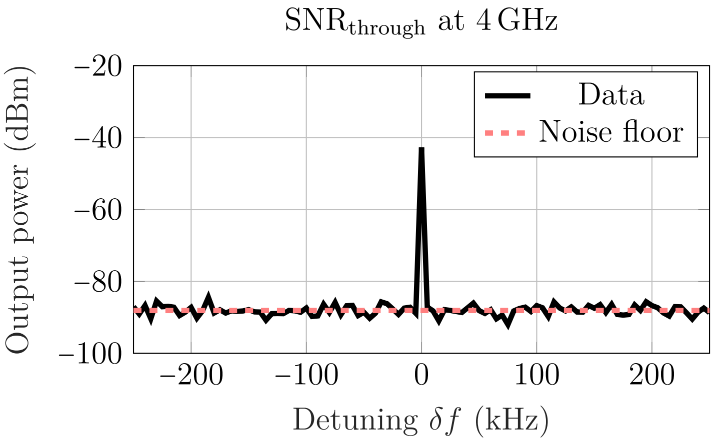

Figure 3.30: The transmission in a 500 kHz range around the signal frequency 4 GHz using the through line and 14 averages. The amplified signal is at −43 dB and the amplified noise floor approximately at −88 dB. The SNR is hence 45 dB.

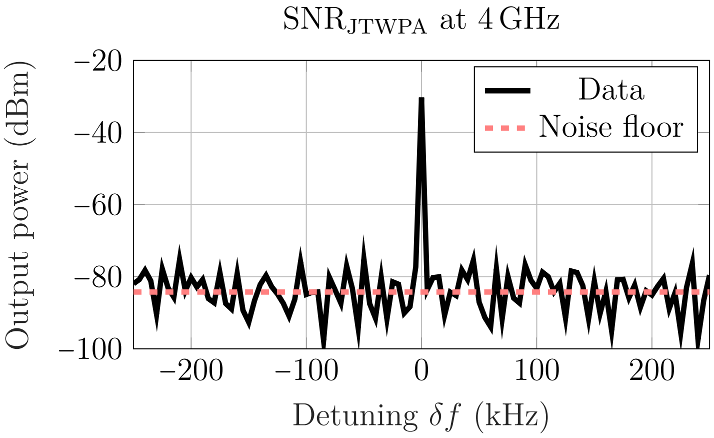

Figure 3.31: The transmission in a 500 kHz range around the signal frequency 4 GHz using the JTWPA with $f_{\mathrm{p}} = 6.058\,\mathrm{GHz}$ and $P_{\mathrm{p}} = -52.6\,\mathrm{dBm}$ and no averages. The amplified signal is at −30 dBm and the amplified noise floor approximately at −84 dBm. The SNR is hence 54 dB. Note that the noise floor looks very noisy since no averages have been used.

3.4.6 Measurement of quantum efficiency

In order to measure the quantum efficiency we use a well characterised qubit in the setup depicted in Figure 3.32. The qubit is characterised as described in Section 3.3. We use this qubit to calibrate the number of photons at the qubit chip, which combined with a spectrum measurement lets us determine the system noise temperature which finally lets us determine the quantum efficiency.

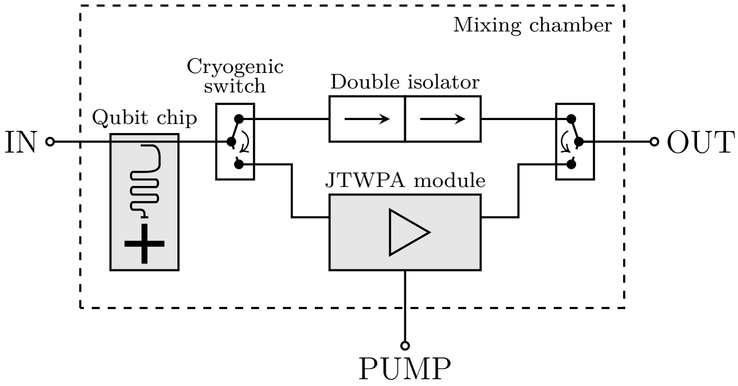

Figure 3.32: The second experimental setup in the mixing chamber to measure the quantum efficiency of the JTWPA module. The qubit is of the Xmon design here. The JTWPA module is put in parallel with a double isolator in order to compare results with the regular readout setup.

3.4.6.1 To measure cavity-referred power

In order to measure the system noise temperature we need to determine the number of photons at the JTWPA IN-port. Assuming low losses between the qubit chip and the JTWPA module, the number of photons is closely related to the cavity-referred power. To measure the cavity-referred power, we send a continuous signal of amplitude 100 mV at a frequency slightly detuned from the qubit resonator frequency and measure the output with a digitizer.

From the qubit calibration, see Section 3.3, we know the number of photons in the resonator at a given readout amplitude. For $A_{\text{drive}} = 100\,\text{mV}$ we get

$$\omega_{\text{ac}} \approx 41.3\,\text{MHz} \tag{3.11}$$

which, recall Equation (3.4a) on page 3-19, gives us that

$$\bar{n} = \frac{\omega_{\text{ac}}}{2\chi} \approx 17.27\,\text{photons}. \tag{3.12}$$

Using the measured coupling strength and the assumption that we have no internal losses in the resonator, the cavity-referred power is given [36] by

$$\bar{P} = \frac{1}{2}\hbar\omega_{\text{r}}\kappa\bar{n} \approx -127.7\,\text{dBm} \quad (\omega_{\text{r}} = 6.305\,\text{GHz}) \tag{3.13}$$

which we then set as the maximum value of the transmission measurement.

3.4.6.2 The standard quantum limit

The standard quantum limit (S.Q.L.) noise power is given by

$$P_{\text{S.Q.L.}} = 2 \cdot \frac{1}{2}\hbar\omega_{\text{r}}\mathcal{S} \tag{3.14}$$

where $\mathcal{S}$ is the measurement resolution bandwidth. The factor 2 comes from the fact that we do non-degenerate amplification. In our setup we sampled 400 data points over 1 MHz in both quadratures, implying that

$$\mathcal{S} = 2 \cdot \frac{1\,\mathrm{MHz}}{400} = 5\,\mathrm{kHz} \tag{3.15}$$

giving us that the noise power S.Q.L.[12] is $-166.8\,\mathrm{dBm}$. The factor 2 here comes from the fact that we sample data points in both quadratures, effectively giving us twice the sampling speed. The corresponding S.Q.L. noise temperature is given by

$$T_{\mathrm{S.Q.L.}} = 2 \cdot \frac{1}{2} \frac{\hbar \omega_{\mathrm{r}}}{k_{\mathrm{B}}} \approx 303\,\mathrm{mK}. \tag{3.16}$$

The factor 2 here also comes from the fact that we do non-degenerate amplification.

3.4.6.3 Noise temperature calculation

We set the power of the S.Q.L. noise floor in Figure 3.33 equal to the vacuum noise temperature in Equation (3.16). Then we use the difference between the measured and calibrated values of the noise floor for pump on and pump off and the vacuum noise floor in order to find the equivalent noise floor temperatures. That is, if

$$\Delta_i = P_i - P_{\mathrm{S.Q.L.}} \quad \text{(in dB)} \tag{3.17}$$

for $i \in \{\text{pump off, pump on, through}\}$ then

$$T_i = T_{\mathrm{S.Q.L.}} \cdot 10^{\frac{\Delta_i}{10}}. \tag{3.18}$$

The noise floor of the through was not measured, but estimated by using the difference between previous measurements of the through and pump off transmissions. The through line includes two switches and a double isolator, which will add loss and effectively increase the noise floor. Find the specific values from the measurement and the estimation in Table 3.2.

---

[12] Recall S.Q.L. from Section 2.3.3.

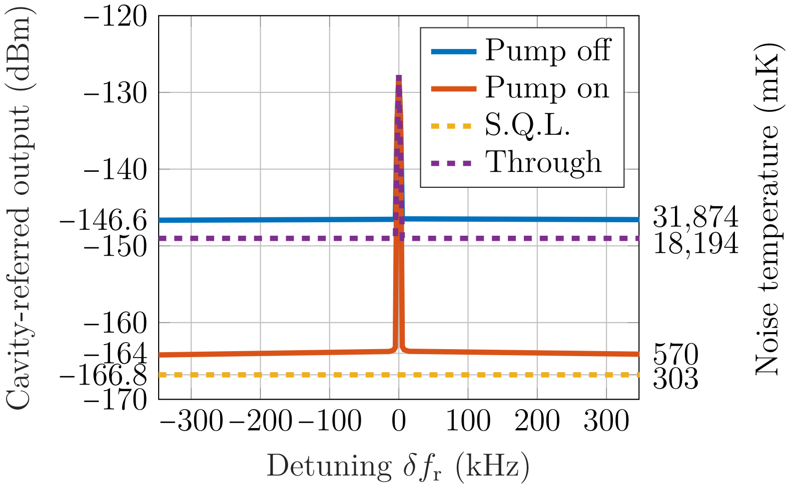

Figure 3.33: Measurement of noise floor for JTWPA pump on and pump off, using the calibrated value of $\bar{n} = 17.27$ at readout frequency $f_{\mathrm{r}} \approx 6.306\,\mathrm{GHz}$. The noise floor with the through is only an estimation. The pump has $f_{\mathrm{p}} = 6.0123\,\mathrm{GHz}$ and $P_{\mathrm{p}} = -52.41$.

Table 3.2: The noise floor in dBm and its equivalent temperature for the measurement. The noise floor with the through is only an estimation.

Noise floor	$P_{\mathrm{N.\text{-}floor}}$ (dBm)	T_{N} (mK)
S.Q.L.	−166.8	303
Pump On	−164.0	570
Pump Off	−146.6	31,874
Through	−149.0	18,194

4

Results

4.1 Gain characteristics

Below the results from the gain characterisation of the JTWPA module are presented.

4.1.1 Gain profiles

In Figure 4.1 three gain profiles are presented that are the "best" gain profiles in different aspects. The first two use a pump with $P_\mathrm{p} = -50.2\,\mathrm{dBm}$ while the third uses $P_\mathrm{p} = -52\,\mathrm{dBm}$.

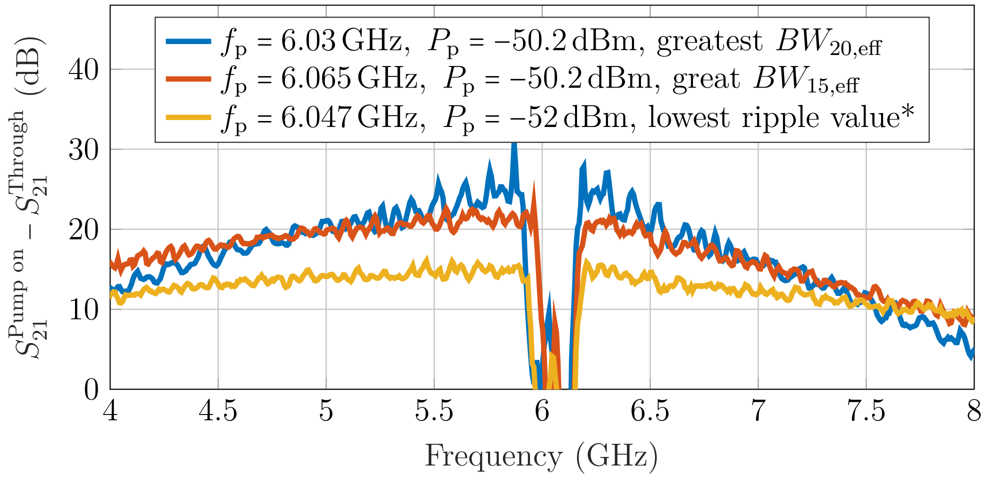

Figure 4.1: Gain profiles for three different pump parameters . The first one has the greatest $BW_{20,\mathrm{eff}} := BW_{G\geq 20} - BW_{\mathrm{Stopband}}$. The second one has the greatest $BW_{15,\mathrm{eff}} := BW_{G\geq 15} - BW_{\mathrm{Stopband}}$ and also a very low ripple value. The third one has the lowest ripple value of all gain profiles that reach 15 dB gain at any point.

The one with $f_\mathrm{p} = 6.03\,\mathrm{GHz}$ has the greatest $BW_{20,\mathrm{eff}}$[1]. The one with $f_\mathrm{p} = 6.065\,\mathrm{GHz}$ has the greatest $BW_{15,\mathrm{eff}}$. The latter also has a relatively low ripple level. The third use a pump with $f_\mathrm{p} = 6.047\,\mathrm{GHz}$ and $P_\mathrm{p} = -52\,\mathrm{dBm}$ and has the lowest ripple value of all the gain profiles with any gain above 15 dB, *i.e.* $BW_{15} \neq 0$.

4.1.2 Average gain

In Figure 4.2 the average gain in dB on the whole interval, excluding the stopband, is presented. A high average gain does not imply high gain at every frequency within the JTWPA module bandwidth[2] but gives a rough estimate on what pump frequencies and pump powers that work for the JTWPA.

Note that there is no data in the region $f_\mathrm{p} \in [6.051, 6.1]\,\mathrm{GHz}$, $P_\mathrm{p} \in [-55, -52.4]\,\mathrm{dBm}$. This is only because we ran out of measurement time and that region seemed less interesting due to its low average gain.

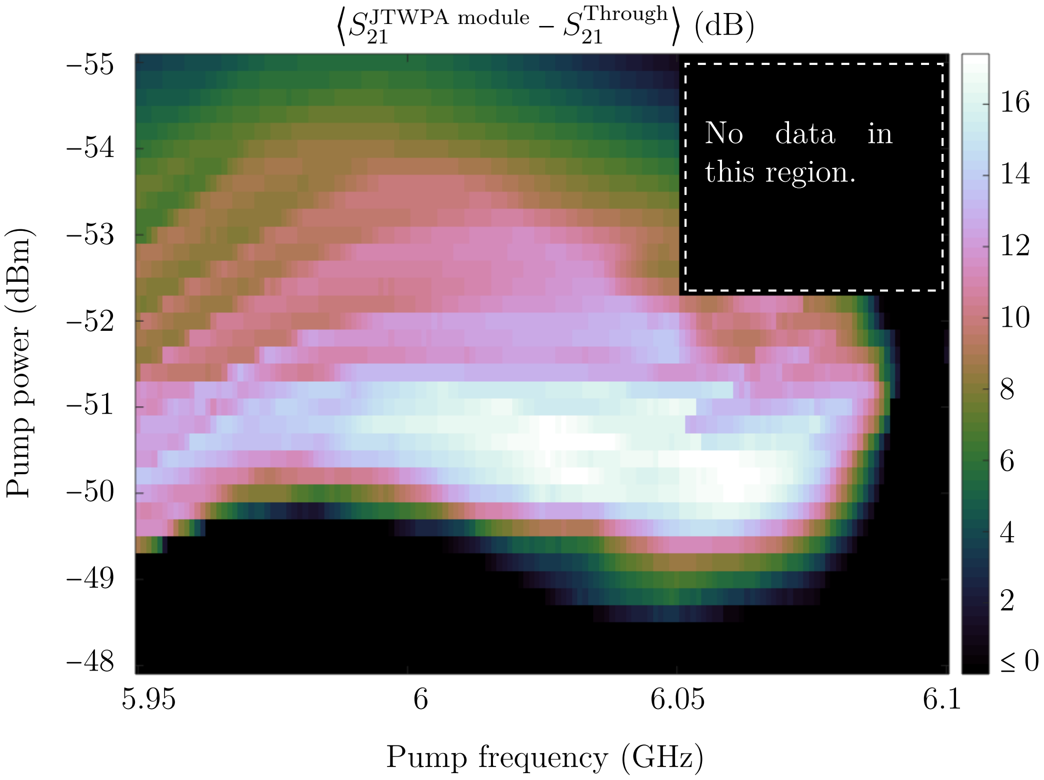

Figure 4.2: The average effective gain (dB) on the interval 4 to 8 GHz, exluding the stopband, for the different measured pumps. All values below 0 have been given the same colour in order to optimise contrast for values above 0. Note the sharp line at pump power equal to −51.2 dBm; the data above and below this line was measured at different times.

---

[1] Recall, effective bandwidth $BW_{x,\mathrm{eff}}$ is defined as the width of the polynomial fit to the curve above x dB gain minus the width of its stopband.

[2] The JTWPA module bandwidth is 4 - 8 GHz.

4.1.3 Bandwidths

In Figure 4.3 the effective bandwidth of 20 dB gain is presented and in Figure 4.4 the effective bandwidth of 15 dB gain is presented. Note that the former has its highest values in the range $P_\mathrm{p} \in [-51, -50]$ dBm, $f_\mathrm{p} \in [6.01, 6.03]$ GHz, while the latter has its highest values in the range $P_\mathrm{p} \in [-51, -50]$ dBm, $f_\mathrm{p} \in [6.05, 6.07]$ GHz.

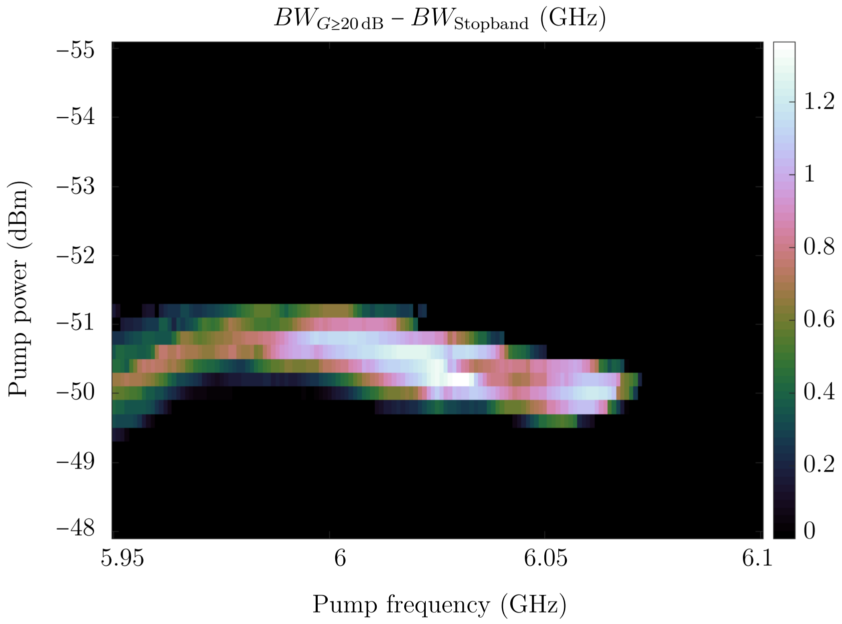

Figure 4.3: The bandwidth (in GHz) for gain above 20 dB minus the bandwidth of the stopband, *i.e.* the effective 20 dB-bandwidth.

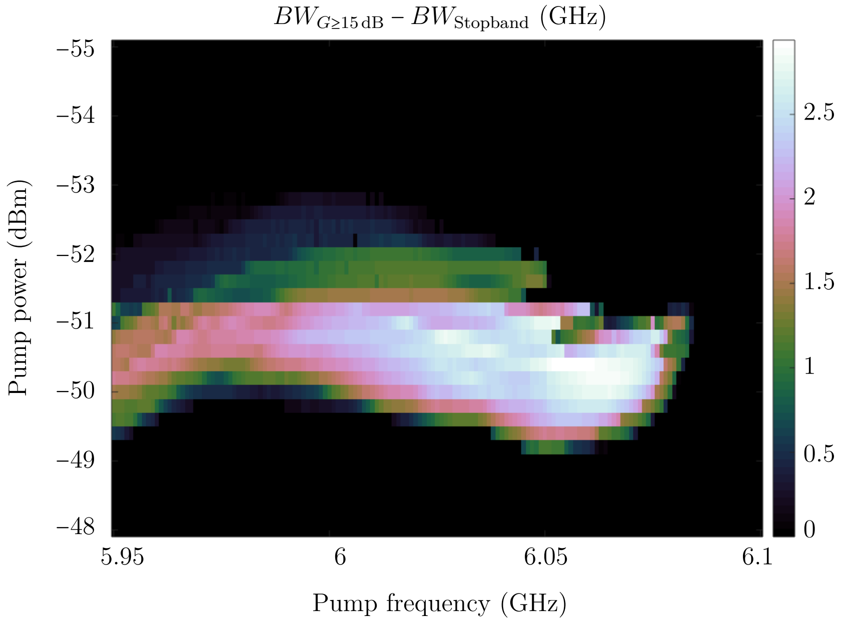

Figure 4.4: The bandwidth (in GHz) for gain above 15 dB minus the bandwidth of the stopband, *i.e.* the effective 15 dB-bandwidth.

4.1.4 Saturation power

Gain as a function of signal power is presented in Figure 4.5 at 4 different frequencies. In Figure 4.6 the average gain at three different intervals is presented. The saturation power[3] varies when studying gain at a single frequency, but converges to $P_{\mathrm{sat}} = -94\,\mathrm{dBm}$ when studying the average gain on intervals, both below the stopband, above the stopband and the whole interval except for the stopband.

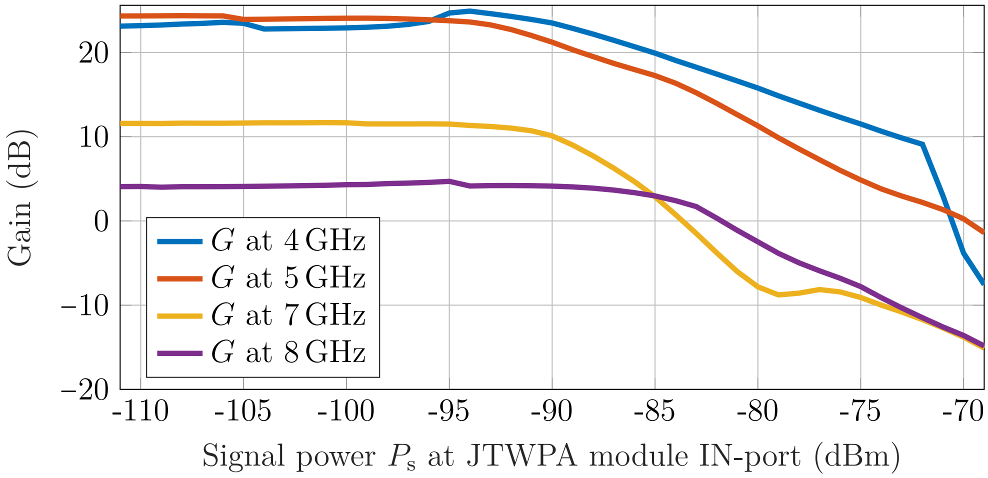

Figure 4.5: Gain at different frequencies for different signal powers using a pump with $f_{\mathrm{p}} = 6.065\,\mathrm{GHz}$ and $P_{\mathrm{p}} = -50.2\,\mathrm{dBm}$. At 4 GHz, $P_{\mathrm{sat}} = -90\,\mathrm{dBm}$. At 5 GHz, $P_{\mathrm{sat}} = -93\,\mathrm{dBm}$. At 7 GHz, $P_{\mathrm{sat}} = -90\,\mathrm{dBm}$. At 8 GHz, $P_{\mathrm{sat}} = -87\,\mathrm{dBm}$.

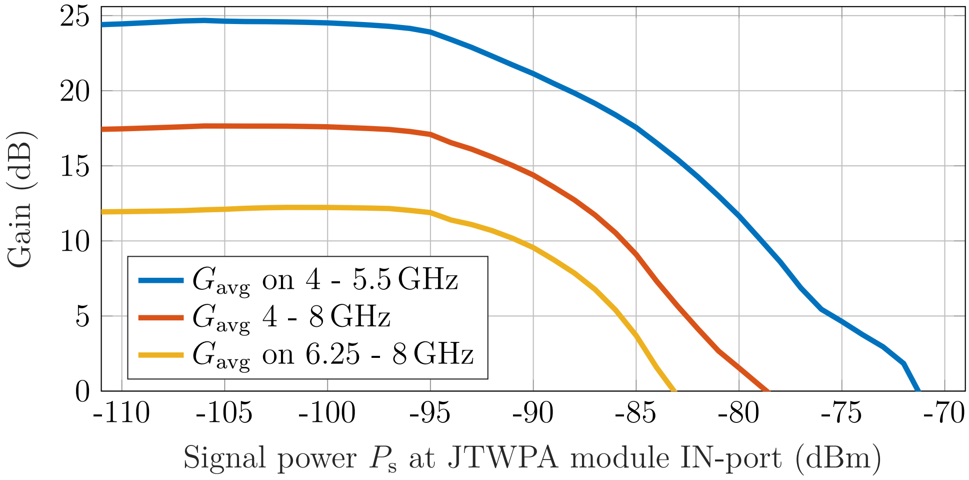

Figure 4.6: Average gain on different intervals for different signal powers using a pump with $f_{\mathrm{p}} = 6.065\,\mathrm{GHz}$ and $P_{\mathrm{p}} = -50.2\,\mathrm{dBm}$. All of the these gains have a saturation power $P_{\mathrm{sat}} = -94\,\mathrm{dBm}$.

---

[3] Also known as the 1-dB compression point, *i.e.* the signal power when the gain is 1 dB less than maximum gain.

4.2 Signal-to-Noise Ratio improvement

The SNR was measured at 36 different frequencies, 4.0-5.7 GHz and 6.3-8.0 GHz with 100 MHz steps, for 5371 different combinations of pump frequencies and pump powers. In Figure 4.7 the average ΔSNR over all 36 the different signal frequencies as a function of all the different pumps is presented.

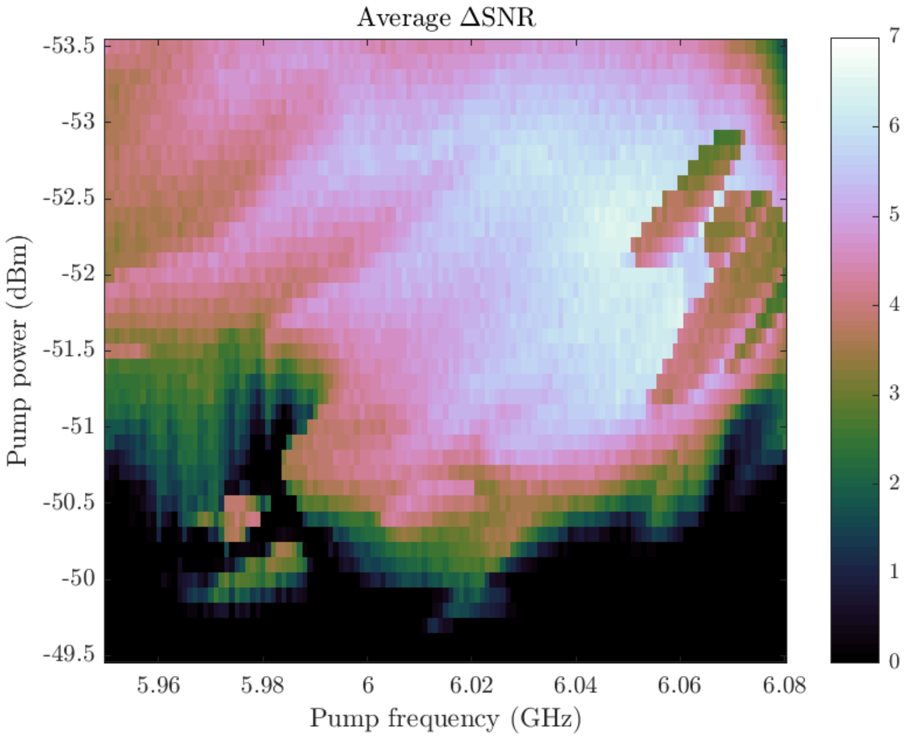

Figure 4.7: The ΔSNR averaged over the signal frequencies, as a function of pump frequency and pump power.

In Figure 4.8 we see the standard deviation of the ΔSNR for each combination of pump frequency and pump power. Finally in Figures 4.9 and 4.10 we see the maxima and minima ΔSNR:s at each combination of pump frequency and pump power. For the interested reader, all ΔSNR data is presented in Appendix B.

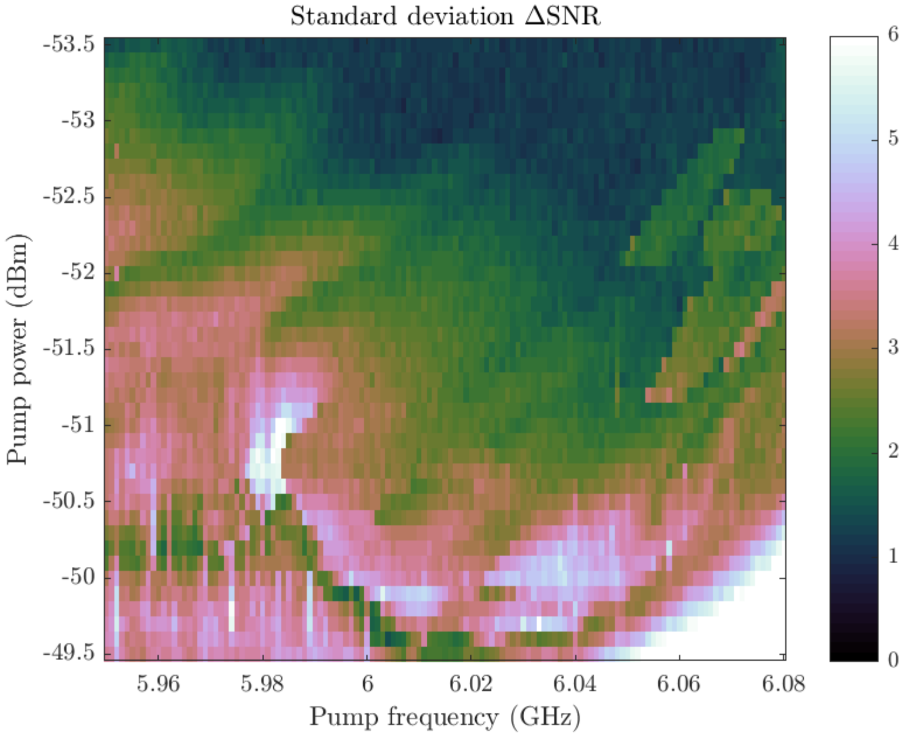

Figure 4.8: The standard deviation of the ΔSNR between the signal frequencies, as a function of pump frequency and pump power.

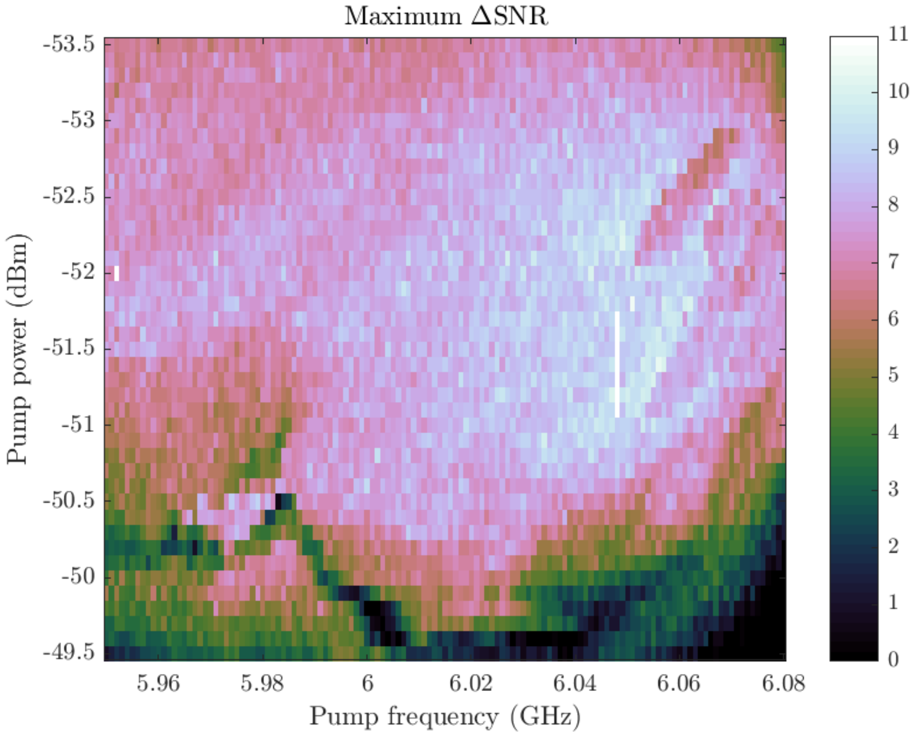

Figure 4.9: The maximum ΔSNR of any of the signal frequencies, as a function of pump frequency and pump power.

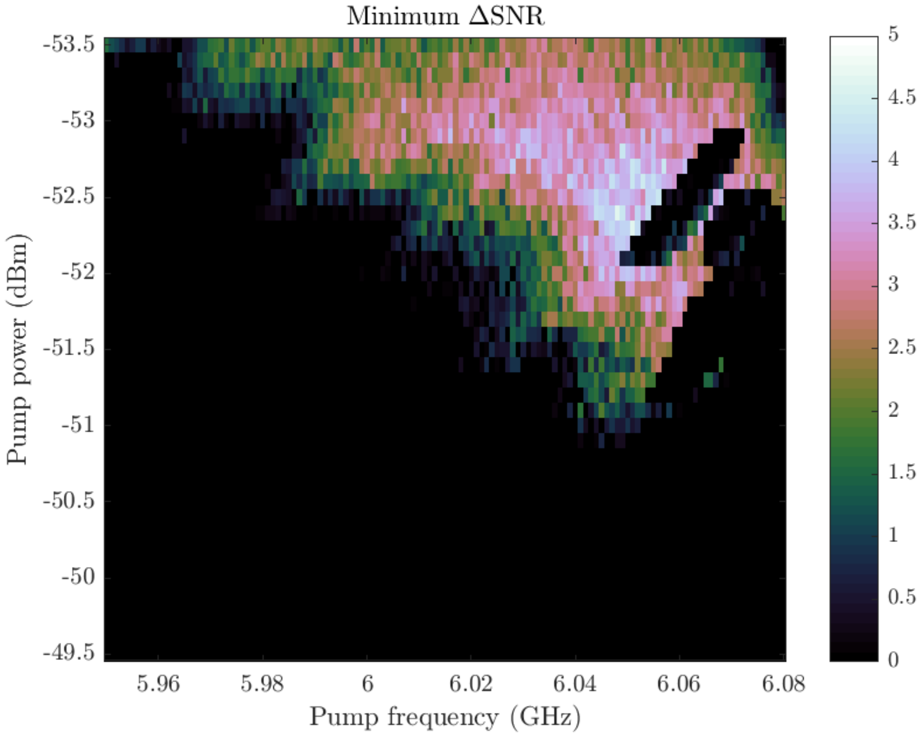

Figure 4.10: The minimum ΔSNR of any of the signal frequencies, as a function of pump frequency and pump power.

4.3 Results from qubit measurements

4.3.1 Quantum efficiency

Using the measured value of the system noise temperature T_N, recall Table 3.2 on page 3-31, we calculate the quantum efficiency to be

$$\eta = \frac{\hbar\omega_\mathrm{r}}{k_\mathrm{B}T_\mathrm{N}} = \begin{cases} 53.1\,\% & \text{for} \quad T_\mathrm{N} = 570\,\mathrm{mK} \quad \text{(pump on)} \\ 0.95\,\% & \text{for} \quad T_\mathrm{N} = 31.8\,\mathrm{K} \quad \text{(pump off)} \\ 1.66\,\% & \text{for} \quad T_\mathrm{N} = 18.2\,\mathrm{K} \quad \text{(through)} \end{cases} \tag{4.1}$$

4.3.2 Single-shot readout

Single-shot readout without the JTWPA is presented in Figure 4.11 and single-shot readout with the JTWPA is presented in Figures 4.12 and 4.13. In these figures the fidelities and the normalised state separation $\Delta V/\sigma$ are presented, where ΔV is the length difference between the average values (given by the crosses) and σ is one standard deviation of the ground state. Discussion about the measurements is presented in Chapter 5.

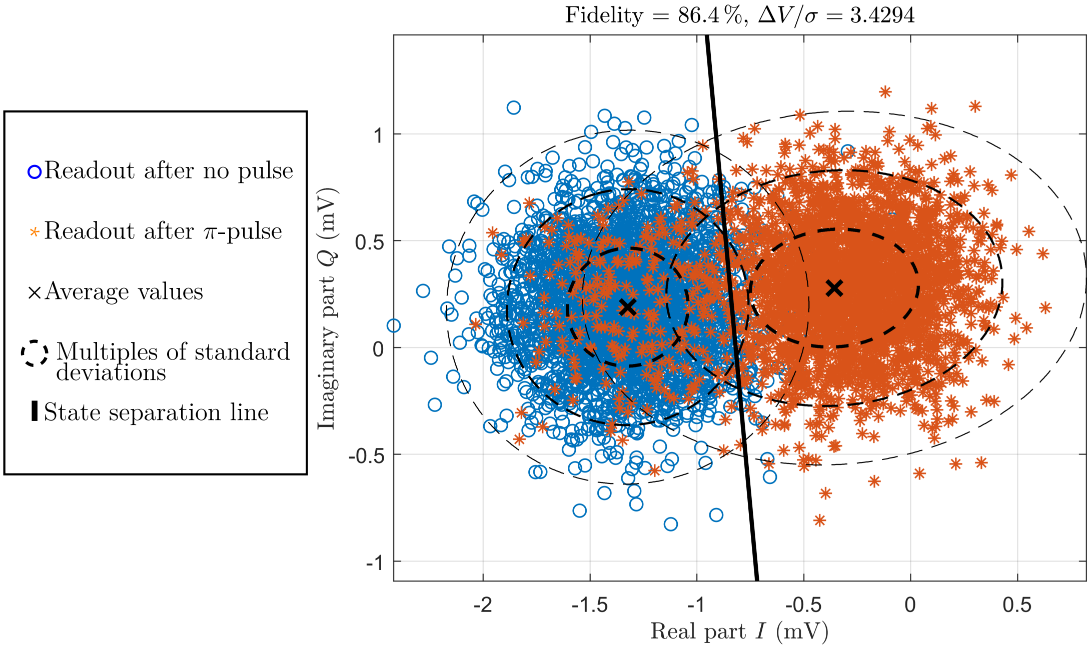

Figure 4.11: A single shot measurement of an Xmon qubit connected to the through, with a total of 2000 points. The fidelity is $F = 86.4\,\%$ and the normalised state separation is $\Delta V/\sigma = 3.4294$.

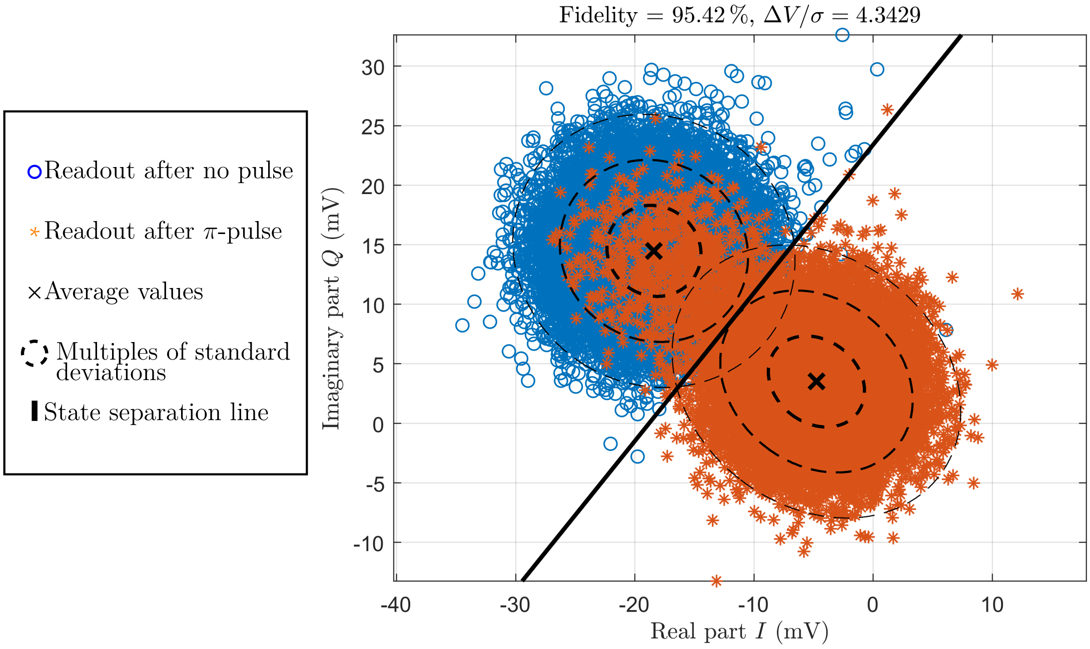

Figure 4.12: A single shot measurement of an Xmon qubit connected to the JTWPA with $f_\mathrm{p} = 6.064\,\mathrm{GHz}$, $P_\mathrm{p} = -51.2\,\mathrm{dBm}$, with a total of 60.000 points. The fidelity is $F = 95.42\,\%$ and the normalised state separation is $\Delta V/\sigma = 4.3420$.

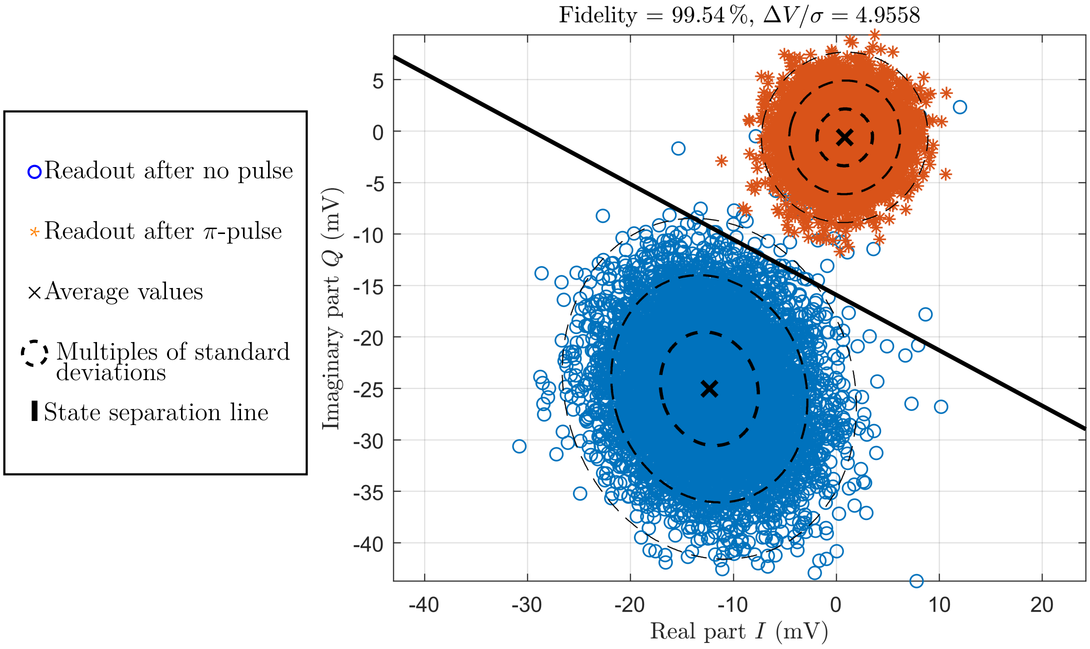

Figure 4.13: A single shot measurement of an Xmon qubit connected to the JTWPA with $f_\mathrm{p} = 6.0635\,\mathrm{GHz}, P_\mathrm{p} = -51.3\,\mathrm{dBm}$, with a total of 20.000 points. The fidelity is $F = 99.54\,\%$ and the normalised state separation is $\Delta V/\sigma = 4.9558$. Note that the state separation line now is in the middle between the states but that moving it closer to the excited state should improve the fidelity.

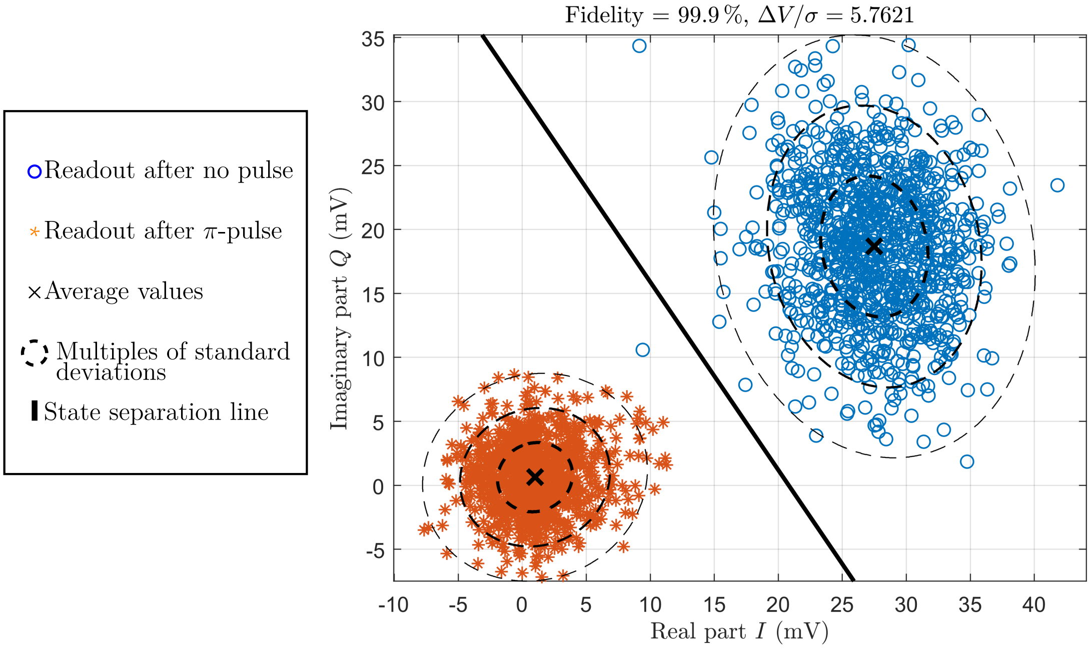

Figure 4.14: A single shot measurement of an Xmon qubit connected to the JTWPA with $f_\mathrm{p} = 6.064\,\mathrm{GHz}, P_\mathrm{p} = -51.2\,\mathrm{dBm}$, with a total of 2.000 points. The fidelity is $F = 99.9\,\%$ and the normalised state separation is $\Delta V/\sigma = 5.7621$.

5

Discussion and Conclusions

Below the results are discussed and the conclusions drawn are presented.

5.1 Gain discussion

As mentioned earlier, it is not easy to define what a good gain profile is. A “good” gain profile will differ depending on what the user needs. However, characteristics that usually are positive are high gain, low gain ripple and a large bandwidth.

5.1.1 Gain ripples

For some combinations of pump power and pump frequency the gain ripples were, without exaggeration, very large. Study Figure 5.1 and note that for $P_\mathrm{p} = -50.8\,\mathrm{dBm}$ and $f_\mathrm{s} \approx 6.45\,\mathrm{GHz}$ we can find a gain difference within a range of 21 MHz as big as 24 dB[1].

A hypothesis for the reason of this was that some of the junctions had turned resistive, and hence created resonances within the JTWPA which may interfere constructively for some frequencies and destructively for others. An argument against this hypothesis is that if some junctions have become resistive for one set of pump parameters, more should become resistive if the pump power is increased. This was however not the case, but rather the opposite. When a gain profile showed this gain ripple behavior, the oscillations in many cases disappeared if the pump power is increased. An example of this is also shown in Figure 5.1.

In the end this was not explored completely. The gain oscillation behaviour only occurred at relatively high pump powers, *i.e.* pump powers giving high gain but low ΔSNR. Since what we really wanted to optimise was the ΔSNR, we decided to not spend too much time investigating the properties of the JTWPA for a pump we will not use in the end anyway.

---

[1] More specifically, at $f_\mathrm{s} = 6.444\,\mathrm{GHz}$ the gain is 33.04 dB, while at $f_\mathrm{s} = 6.465\,\mathrm{GHz}$ it is only 8.59 dB.

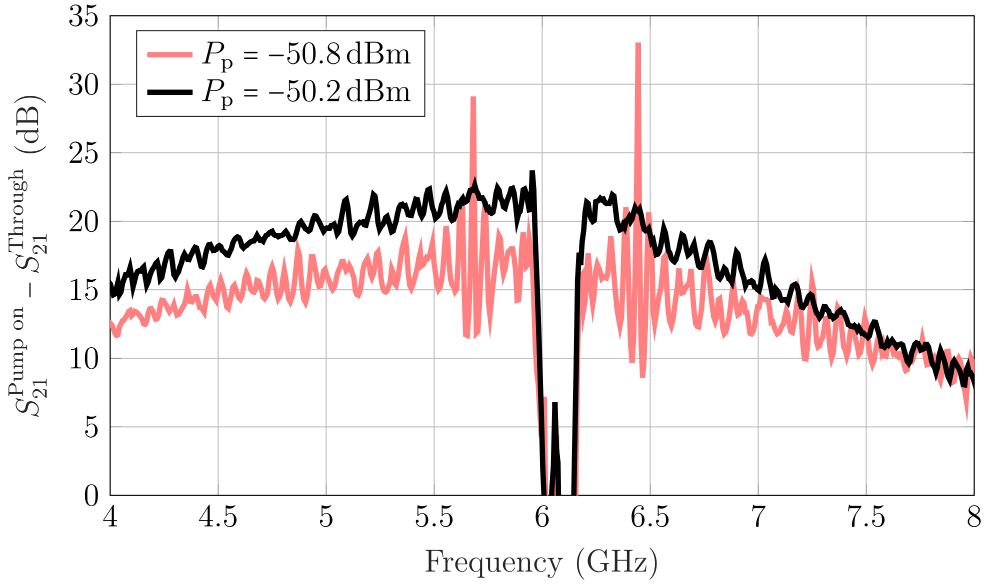

Figure 5.1: Two gain profiles at the same pump frequency $f_p = 6.062\,\mathrm{GHz}$ but at different pump powers. Note the gain oscillations close to the stopband for the gain profile with the lower pump power.

5.1.2 Stopband

According to the theory in Section 2.4.2, the stopband should reach from $2f_p - f_{\text{upper}}$ to f_{upper}, where f_p is the pump frequency and $f_{\text{upper}} = f_{\text{upper}}^{\text{disp}}$. In other words, the upper bound of the stopband should be fix at the same value as the dispersive feature's upper bound while the lower limit should be dependent on the pump frequency and the upper limit.

This was measured and verified to almost be the case, see Figure 5.2. The theoretical prediction was right about the upper limit being fixed, and it almost is. But it is not exactly at the same frequency as the upper bound of the dispersive feature, $f_{\text{upper}}^{\text{disp}} = 6.2\,\mathrm{GHz}$, but slightly lower, $f_{\text{upper}}^{\text{stopband}} \approx 6.18\,\mathrm{GHz}$. This upper limit also got smaller in regions of high gain. If f_{upper} is redefined to be this slightly lower upper limit, the lower limit is still given by the same equation.

5.1.3 Comparison of parametric and effective gain

Recall the difference between effective gain (Equation (3.7) on page 3-21) and parametric gain (Equation (3.8) on page 3-21). The effective gain is the actual gain of the JTWPA module, while the parametric gain is the difference between the amplified signal and the attenuated signal due to the insertion loss of the JTWPA module. These gains are hence related to each other as

$$G_{\text{eff}} = G_{\text{par}} - L_{\text{JTWPA module}} \tag{5.1}$$

if they are expressed in dB. Obviously the effective gain is the gain of interest, which usually can be estimated from the parametric gain by subtracting the losses according to the previously determined loss equation (recall Equation (3.9) on page 3-22).

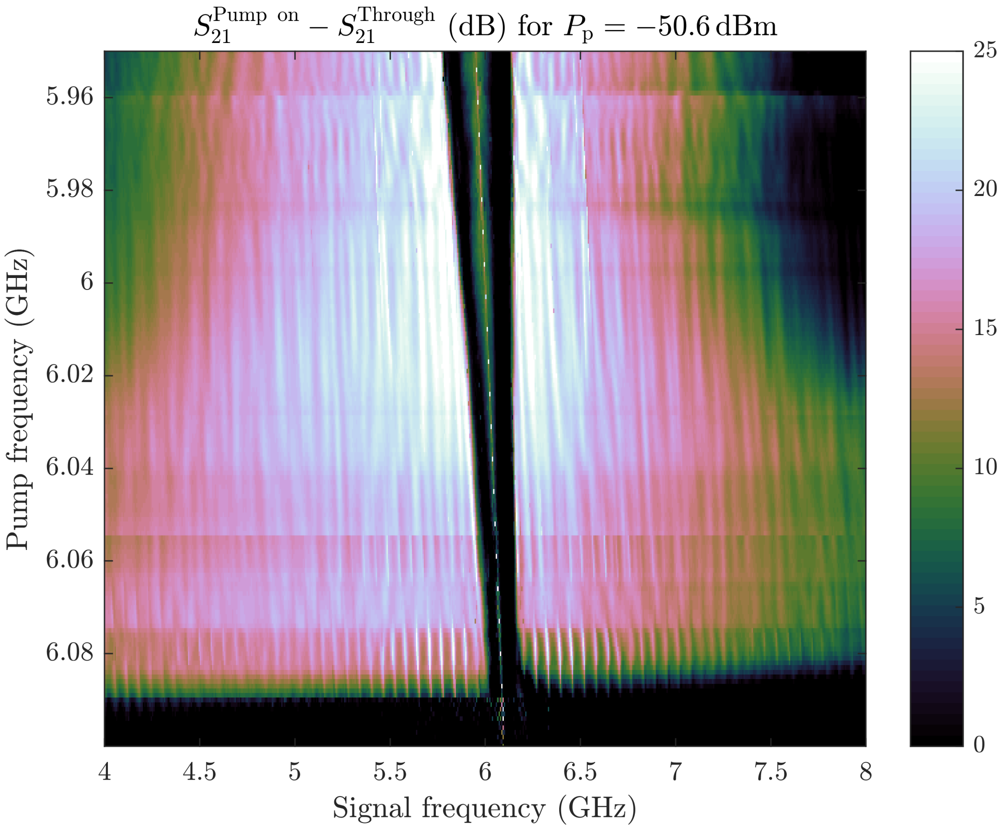

Figure 5.2: The effective gain for $P_\text{p} = -50.6\,\text{dBm}$ as a function of pump frequency f_p and signal frequency f_s. It is clear that the stopband upper limit f_upper is fix while its lower limit f_lower is linearly dependent on the pump frequency f_p. Note that all values below zero dB, *i.e.* the regions where the JTWPA module attenuates instead of amplifying, have been put to zero in order to increase the gain contrast.

However, as discussed above in Section 5.1.2, the upper bound of the dispersive feature is slightly higher than the upper bound of the stopband. This will result in a seemingly very large gain around the upper bound of the stopband when measuring the parametric gain (an example of this is shown further down, in Figure 5.5). This very large gain is only visible when studying the parametric gain since it is not actual strong signal gain but rather a strong compensation of the JTWPA module losses in this region.

5.1.4 Definition of bandwidth

There are multiple definitions of a bandwidth, while the most common is when the gain profile is 3 dB below maximum gain, while in this thesis the definition used is the one described previously, *i.e.* BW_x is the width of the mathematical fit for gain above x dB. The reasons for this choice are discussed below.

The mathematical fit is considered when determining bandwidth, instead of the actual measured gain profile data, because many of the gain profiles have big gain ripples. If the actual data was considered instead, the maximum gain would be at the top of one of these ripples, and the bandwidth would hence only be the width of the ripple.

The above-x dB bandwidth is considered instead of 3 dB below maximum gain because some of the gain profiles, *e.g.* the one depicted in Figure 3.29 on page 3-25, have a knob-like feature, giving them high gain in a narrow range, while others do not have this feature. Using the 3 dB below maximum gain definition would hence tell us that some gain profiles have a very narrow bandwidth and others a very wide bandwidth, while the ones with the narrow bandwidth still might have the overall highest gain. It would hence be misleading.

5.2 SNR discussion

Recall Figure 4.7 on page 4-5. Note that the ΔSNR is the highest around $P_\mathrm{p} \approx -52$ dBm, even though we know from the gain results that the highest gain is reached at $P_\mathrm{p} \approx -50$ dBm (recall Figure 4.2 on page 4-2). This implies that the highest gain does not necessarily mean that the ΔSNR is the highest.

Let us study the amplification of the signal, see Figure 5.3, and we see that the signal is amplified both for the low pump powers ($P_\mathrm{p} \approx -52$ dBm) and for high pump powers ($P_\mathrm{p} \approx -50$ dBm). Now let us compare it with the amplification of the noise floor, see Figure 5.4. We see that for high pump powers, the noise floor is more or less equally amplified, implying that the ΔSNR is approximately zero. Meanwhile, for low pump powers, the noise floor is only slightly amplified, giving us high ΔSNR. We can hence draw the conclusion that at high pump powers the ΔSNR is low because the amplifier adds about the same amount of noise photons as it adds signal photons.

There is a strange feature with the ΔSNR-measurements worth to mention. In the region with high ΔSNR, *i.e.* for $f_\mathrm{p} \in [6.03, 6.06]$ GHz and $P_\mathrm{p} \in [-53, -51]$ dBm, there are two smaller regions where the ΔSNR drops significantly (recall Figure 4.7 on page 4-5). The reason for this is yet to be understood and it should be investigated further, but for now we can draw the conclusion that these regions should be avoided.

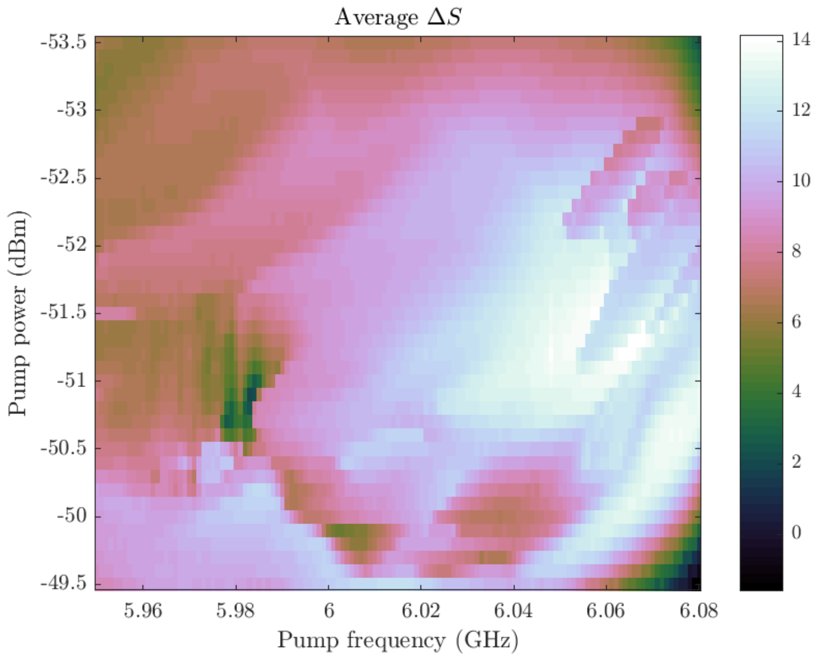

Figure 5.3: The average signal amplification as a function of pump frequency and pump power.

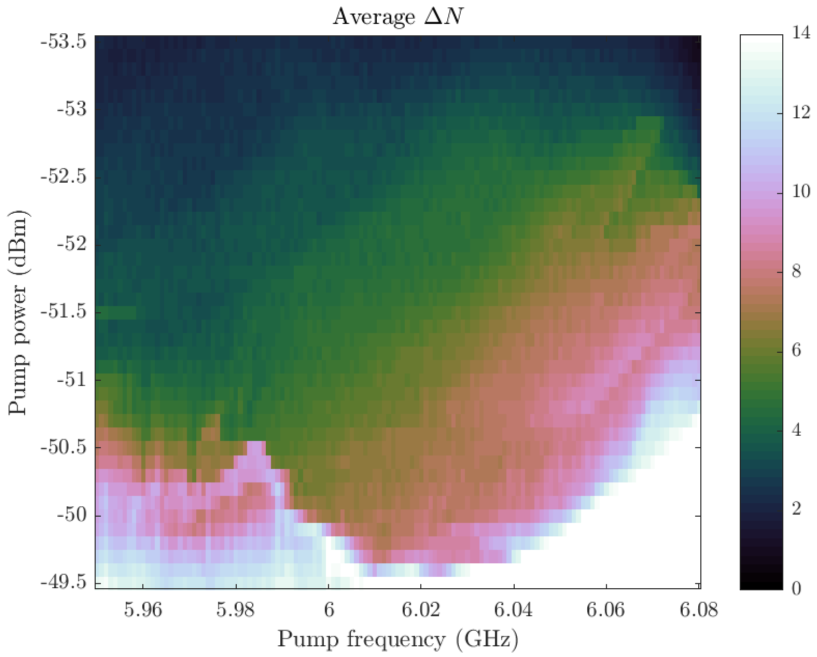

Figure 5.4: The average noise floor amplification as a function of pump frequency and pump power.

5.3 Single-shot readout and quantum efficiency

It is clear from the single-shot readout measurements that the JTWPA enhances the readout fidelity, but it is hard to say exactly how much it enhances the readout. The main reason for this is because the qubit used had to be recalibrated after the JTWPA was switched in and therefore the measurements cannot be directly compared.

There is also a strange feature in some of the JTWPA amplified single-shot readout measurements, recall Figure 4.13 on page 4-9. In theory the JTWPA should, since we use non-degenerate 4-wave mixing (recall Table 1.1 on page 1-8) amplify the two quadratures of the qubit equally, and also keep them symmetrically Gaussian distributed. This we see in Figure 4.12. But, in Figures 4.13 and 4.14 it is clear that the ground state is amplified more and also that its shape is changed. The reason for this is not understood. Even more strange is that the pump parameters are almost identical for these three measurements. However, these results were acquired during a time when we experienced gain instabilities, which we think were caused by an unstable pump source. It is hence possible that the pump parameters in reality were more different than we think.

Another thing about Figure 4.13 on page 4-9 is that we do not seem to have any relaxation at all. The qubit relaxation time is $T_1 \approx 100\,\mu\mathrm{s}$, the readout is completed about $2\,\mu\mathrm{s}$ after the π-pulse is done and we do 10.000 measurements after a π-pulse. Therefore there should be about 200 stars in the ground state, but we do not measure ground state one single time. We have not been able to determine why this is, but a hypothesis is that in some cases the strong readout stabilises the qubit in the excited state.

From the quantum efficiency measurement it is clear that the losses in the JTWPA have a very negative impact if there is no pump. Therefore the JTWPA should not be used in a readout line without also using a pump.

5.4 Conclusions

To summarise the results and the discussion of the JTWPA, the conclusions we can draw are:

- Pump power and frequency interdependent, *i.e.* one cannot determine the best pump power and pump frequency independently.
- Highest gain does not imply highest ΔSNR.
- Small changes in the pump can strongly affect the gain profile.
- Different pumps, and thereby different gain profiles, may be useful for different applications.

- The JTWPA module insertion loss L in dB at frequency f in GHz is well approximated by $L = 0.91f + 0.4 \pm 0.25$.
- The JTWPA module stopband is well estimated to reach from $2f_\mathrm{p} - f_\mathrm{upper}$ to f_upper, where f_p is the pump frequency in GHz and $f_\mathrm{upper} = 6.18\,\mathrm{GHz}$.
- The saturation power is $P_\mathrm{sat} \approx -94\,\mathrm{dBm}$.
- Highest gain is generally reached for $P_\mathrm{p} \approx -50\,\mathrm{dBm}$ and $f_\mathrm{p} \approx 6.06\,\mathrm{GHz}$.
- Highest ΔSNR is generally reached for $P_\mathrm{p} \approx -52\,\mathrm{dBm}$ and $f_\mathrm{p} \approx 6.05\,\mathrm{GHz}$.
- There are two regions with low ΔSNR very close to the region with high ΔSNR in the pump power/frequency-plane which need to be avoided.
- For $P_\mathrm{p} \approx -50\,\mathrm{dBm}$ the JTWPA adds noise photons to the extent that the SNR remains unchanged, while for $P_\mathrm{p} \approx -52\,\mathrm{dBm}$ it adds very few noise photons, increasing the SNR with between 5 and 11 dB.
- The JTWPA module can reach a system noise temperature close to the standard quantum limit and a system quantum efficiency above 50 %.

5.5 JTWPA calibration for new measurements

If the JTWPA is going to be installed and used in a new setup it needs to be recalibrated. The pump frequency does not need to be calibrated, since a properly working pump source will generate a signal with the frequency requested of it, but the pump power needs to be recalibrated since the exact total loss of all cables, all contacts, all attenuators, *etc*, is hard to know and the JTWPA is very sensitive to both pump frequency and pump power. In order to do this calibration, follow the instruction below.

1. Connect a VNA to the signal line and the pump source to the pump input line.
2. Set the pump frequency to $f_\mathrm{p} = 6.065\,\mathrm{GHz}$ and the pump power to what is expected to be $P_\mathrm{p} \approx -60\,\mathrm{dBm}$ at the JTWPA module pump-port.
3. Measure the parametric gain, *i.e.* the difference in transmission for pump on and pump off, for these pump settings in the interval 4-8 GHz.
4. Redo this for higher and higher pump power, with steps of 1 dB. At some point you should start getting gain. Keep increasing the pump power until the gain drops to zero.
5. Once you have found an approximate pump power region where the gain is the highest, sweep the pump power in this region in a 4 dB interval, with 0.2 dB steps.

6. Now you should have a similar image to the one presented in Figure 5.5. Determine the pump power giving the highest parametric gain. This pump power corresponds to −50 dBm at the JTWPA module pump-port. Now the results from the thesis can be used by subtracting the difference between pump source output power giving the highest gain and −50 from whichever pump power you want to use.

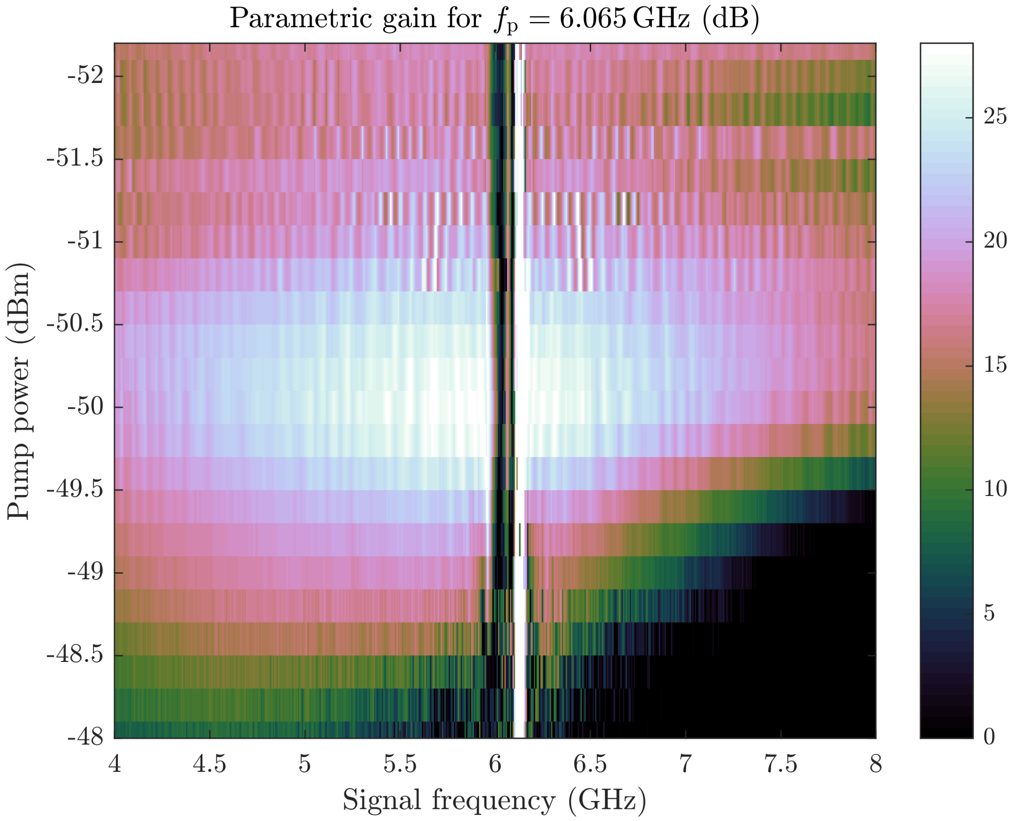

Figure 5.5: The parametric gain of the JTWPA module for $f_\mathrm{p} = 6.065$ GHz as a function of pump power at the JTWPA module and signal frequency. Note the huge parametric gain around the upper bound of the stopband.

5.6 Future work

Things that could be done in a future work to improve the JTWPA characterisation are:

- **Measure the gain profiles multiple times.** In this thesis work the gain profiles were measured with a VNA using averages, in order to average away noise. An improvement for the future could be to measure the gain profiles many times instead of using averages, since then the gain stabilities could be studied.

- **Measure the gain profiles for high ΔSNR.** In this work the gain was mainly studied in the region where the gain was the highest. Later it turned out that the highest ΔSNR was reached at lower pump powers. It would be interesting to study the gain profiles closer in this region.

- **Measure the ΔSNR multiple times.** Due to time limitations we could only measure the SNR for each pump once, making the results fairly noisy (recall Figure 3.31 on page 3-28). The ΔSNR-results would be more clear if the ΔSNR was measured multiple times in the relevant region (*i.e.* for $f_\mathrm{p} \in [6.03, 6.06]\,\mathrm{GHz}$ and ($P_\mathrm{p} \in [-53, -51]\,\mathrm{dBm}$).

- **Characterisation of the components.** By measuring each component's and each cable's transmission, reflection and insertion loss, it would be easier to make more accurate predictions about the JTWPA module as a whole. Then the resonance at 9 GHz (recall Figure 3.25 on page 3-22) might be located to one of the components.

- **Use of integrated through.** In this work the through has always been put in parallel with the JTWPA module as a whole. This was done since the JTWPA module as a whole was what was going to be used in the end. Increased understanding of the JTWPA could be reached by integrating a through into the JTWPA module and hence be able to measure intrinsic effective gain[2]. The circuit schematics for this are shown in Figure A.1 on page A-1.

- **Quantum efficiency map.** Gain and ΔSNR were measured for multiple pump powers and frequencies, which could then be shown in maps (recall Figure 4.2 on page 4-2 and Figure 4.7 on page 4-5), while the noise temperature and the quantum efficiency only were for one pump frequency and power. A similar map of quantum efficiency for different pump frequencies and powers could be useful. This was not done in this work simply due to lack of time. Some unexplained experimental problems took a lot of time, such as strong gain fluctuations.

- **Use of pump filter.** The pump power exiting the refrigerator was quite high, about ~ 7 dBm. The effects of the pump in the down conversion process is not completely known, but it might be one of the reasons for the strange amplification of the ground state of the qubit. To ensure that the pump does not affect the down conversion, or any other process outside the refrigerator, a bandstop filter should be added to the OUT-port of the JTWPA module, which would then reflect the pump into the OUT-isolators.

- **Ensure atomic reference lock.** We experienced some gain instabilities. It seemed like the JTWPA switched between different gain profiles. We believe the reason for this is that the pump source used an internal reference instead of the atomic clock and hence was not stable in frequency. To ensure this does not happen again for future measurements, the user should ensure that the

---

[2] That is, the effective gain of the JTWPA excluding the insertion loss of the other JTWPA module components.

pump source is properly locked to an atomic clock reference.

- **Use of one good qubit for calibration.** Throughout this work we have worked with multiple qubits. Since we kept changing qubits between the cooldowns, a lot of time was put into calibrating each new qubit. Multiple cooldowns were more or less wasted since many of the qubits turned out to be too bad to use for the calibration. A lot of time would hence be saved by using one good qubit for all cooldowns.
- **Measure reflection and backwards-travelling pump.** By putting a circulator in front of the JTWPA module, one could measure the JTWPA module reflection as well as the pump signal travelling out of the IN-port due to finite directivity and reflection at the JTWPA. This could help understanding the possible back-action of the JTWPA module on the sample.
- **Further investigation of single-shot measurements.** Some of our single-shot measurements using the JTWPA were only slightly better compared with a line through, while others were a lot better, but the pump parameters were almost identical between the measurements. This is not yet completely understood and should be investigated further.
- **Use of pump cancellation.** We used a double isolator at the JTWPA module IN-port to isolate the sample from the reflected and the backwards-travelling pump, but some of pump will still leak through. This can be improved by connecting another signal at the directional coupler isolation port, an “anti-pump”, at the pump frequency which is π-shifted compared with the pump.
- **Measure two JTWPAs in parallel.** Both JTWPA brackets were made to be able carry two JTWPAs in parallel, but we never got to that point. It could be interesting to study if the JTWPAs disturb each other, and if adding a second JTWPA line makes thermalisation of the refrigerator harder or not.
- **Measure two JTWPAs in series.** It could be interesting to connect two JTWPAs in a series after each other and do a similar characterisation as the one described in this thesis for this new system.

Bibliography

[1] M. A. Nielsen and I. L. Chuang, *Quantum computation and quantum information.* Cambridge : Cambridge University Press, 2010, ISBN: 978-1-107-00217-3.

[2] H. K. Onnes, "The resistance of pure mercury at helium temperatures", *Commun. Phys. Lab. Univ. Leiden*, 1911.

[3] F. Henyey, "Distinction between a perfect conductor and a superconductor.", *Physical Review Letters*, vol. 49, no. 6, p. 416, 1982, ISSN: 00319007.

[4] N. N. Bogoliubov, *The theory of superconductivity.* Ser. International science review series: 4. Gordon and Breach, 1962.

[5] B. Josephson, "Possible new effects in superconductive tunnelling.", *Physics Letters*, vol. 1, no. 7, pp. 251–253, 1962, ISSN: 00319163.

[6] A. Barone and G. Paternò, *Physics and applications of the Josephson effect.* New York : Wiley, cop., 1982, ISBN: 0-471-01469-9.

[7] D. K. Cheng, *Field and wave electromagnetics. [electronic resource].* Pearson Education, 2014, ISBN: 1292038942.

[8] F. Pobell, *Matter and methods at low temperatures. [electronic resource].* Berlin ; New York : Springer, 2007, ISBN: 3540463569.

[9] S. Bens, "A single photon generator for microwave photons", Master's thesis, Chalmers University of Technology, 2016.

[10] A. A. Clerk, M. H. Devoret, S. M. Girvin, F. Marquardt, and R. J. Schoelkopf, "Introduction to quantum noise, measurement, and amplification", *Rev. Mod. Phys.*, vol. 82, pp. 1155–1208, 2 Apr. 2010.

[11] J. F. Cox, *Fundamentals of linear electronics : integrated and discrete.* Delmar, 2002, ISBN: 0-7668-3018-7.

[12] C. S. Macklin, "Quantum feedback and traveling-wave parametric amplication in superconducting circuits", PhD thesis, University of California, Berkeley, 2015.

[13] M. Simoen, "Parametric interactions with signals and the vacuum", PhD thesis, Chalmers University of Technology, 2015.

[14] P. Krantz, *Parametrically pumped superconducting circuits.* Lic. thesis, Chalmers University of Technology, Göteborg, 2013.

[15] P. Krantz, Y. Reshitnyk, W. Wustmann, J. Bylander, S. Gustavsson, W. D. Oliver, T. Duty, V. Shumeiko, and P. Delsing, "Investigation of nonlinear effects in josephson parametric oscillators used in circuit quantum electrodynamics", *New Journal of Physics*, vol. 15, no. 10, p. 105 002, Oct. 2013.

[16] P. Krantz, A. Bengtsson, M. Simoen, S. Gustavsson, V. Shumeiko, W. Oliver, C. Wilson, P. Delsing, and J. Bylander, "Single-shot read-out of a superconducting qubit using a josephson parametric oscillator.", *Nature communications*, vol. 7, p. 11 417, 2016.

[17] P. Krantz, "The josephson parametric oscillator : From microscopic studies to single-shot qubit readout.", PhD thesis, Chalmers University of Technology, Göteborg, 2016, ISBN: 9789175973746.

[18] I.-M. Svensson, A. Bengtsson, P. Krantz, J. Bylander, V. Shumeiko, and P. Delsing, "Period-tripling subharmonic oscillations in a driven superconducting resonator", *Phys. Rev. B*, vol. 96, p. 174 503, 17 Nov. 2017.

[19] A. Bengtsson, P. Krantz, M. Simoen, I.-M. Svensson, B. Schneider, V. Shumeiko, P. Delsing, and J. Bylander, "Nondegenerate parametric oscillations in a tunable superconducting resonator", *Phys. Rev. B*, vol. 97, p. 144 502, 14 Apr. 2018.

[20] C. Macklin, K. O'Brien, D. Hover, M. Schwartz, V. Bolkhovsky, X. Zhang, W. Oliver, and I. Siddiqi, "A near-quantum-limited josephson traveling-wave parametric amplifier.", *Science*, no. 6258, p. 307, 2015, ISSN: 0036-8075.

[21] D. M. Pozar, *Microwave Engineering.* Chichester, 2012, ISBN: 9781118213636.

[22] B. J. Jafari, "Fabrication of on-chip microwave circulators", Master's thesis, Chalmers University of Technology, Jul. 2013.

[23] G. Johansson and T. Bauch, *A quantum bit*, Lecture note, Sep. 2018.

[24] J. Koch, T. M. Yu, J. Gambetta, A. A. Houck, D. I. Schuster, J. Majer, A. Blais, M. H. Devoret, S. M. Girvin, and R. J. Schoelkopf, "Charge-insensitive qubit design derived from the cooper pair box", *Phys. Rev. A*, vol. 76, p. 042 319, 4 Oct. 2007.

[25] Y. Nakamura, Y. A. Pashkin, and J. S. Tsai, "Coherent control of macroscopic quantum states in a single-cooper-pair box.", *Nature*, vol. 398, pp. 786–788, 1999.

[26] A. Wallraff, D. I. Schuster, A. Blais, L. Frunzio, R.-. S. Huang, J. Majer, S. Kumar, S. M. Girvin, and R. J. Schoelkopf, "Strong coupling of a single photon to a superconducting qubit using circuit quantum electrodynamics.", *Nature*, no. 7005, p. 162, 2004, ISSN: 0028-0836.

[27] A. Blais, R.-S. Huang, A. Wallraff, S. M. Girvin, and R. J. Schoelkopf, "Cavity quantum electrodynamics for superconducting electrical circuits: An architecture for quantum computation", *Phys. Rev. A*, vol. 69, p. 062 320, 6 Jun. 2004.

[28] E. Jaynes and F. Cummings, "Comparison of quantum and semiclassical radiation theories with application to the beam maser.", *Proceedings of the IEEE*, vol. 51, no. 1, p. 89, 1963, ISSN: 00189219.

[29] C. Gerry and P. Knight, *Introductory Quantum Optics.* Cambridge : Cambridge University Press, 2004, ISBN: 9780511791239.

[30] A. A. Houck, J. A. Schreier, B. R. Johnson, J. M. Chow, J. Koch, J. M. Gambetta, D. I. Schuster, L. Frunzio, M. H. Devoret, S. M. Girvin, and R. J. Schoelkopf, "Controlling the spontaneous emission of a superconducting transmon qubit", *Phys. Rev. Lett.*, vol. 101, p. 080 502, 8 Aug. 2008.

[31] P. Krantz, M. Kjaergaard, F. Yan, T. P. Orlando, S. Gustavsson, and W. D. Oliver, "A Quantum Engineer's Guide to Superconducting Qubits", *arXiv e-prints*, Apr. 2019. arXiv: `1904.06560 [quant-ph]`.

[32] K. O'Brien, C. Macklin, I. Siddiqi, and X. Zhang, "Resonant phase matching of josephson junction traveling wave parametric amplifiers", *Phys. Rev. Lett.*, vol. 113, p. 157 001, 15 Oct. 2014.

[33] A. B. Zorin, "Josephson traveling-wave parametric amplifier with magnetic flux drive.", *arXiv e-prints*, 2018. arXiv: `1804.09109`.

[34] J. E. Johnson, C. Macklin, D. H. Slichter, R. Vijay, E. B. Weingarten, J. Clarke, and I. Siddiqi, "Heralded state preparation in a superconducting qubit", *Phys. Rev. Lett.*, vol. 109, p. 050 506, 5 Aug. 2012.

[35] S. Probst, F. B. Song, P. A. Bushev, A. V. Ustinov, and M. Weides, "Efficient and robust analysis of complex scattering data under noise in microwave resonators", *Review of Scientific Instruments*, vol. 86, no. 2, p. 024 706, 2015.

[36] A. Bruno, G. de Lange, S. Asaad, K. L. van der Enden, N. K. Langford, and L. DiCarlo, "Reducing intrinsic loss in superconducting resonators by surface treatment and deep etching of silicon substrates", *Applied Physics Letters*, vol. 106, no. 18, p. 182 601, 2015.

[37] R. E. Collin, *Foundations for Microwave Engineering. [electronic resource].* Ser. The IEEE/OUP Series on Electromagnetic Wave Theory (Formerly IEEE Only), Series Editor Ser: Donald G. Dudley Ser Vol. 11. Wiley-IEEE Press [Imprint] Jan. 2001 Hoboken : John Wiley & Sons, Incorporated., 2001, ISBN: 9780780360310.

Part II

Appendices

A

Setup schematics

In this appendix more setup schematics are shown. In Figure A.1 the setup schematics of the JTWPA module with an integrated through line is depicted.

In Figure A.2 the first setup is completely depicted, including all attenuators on all cryostat levels, which was used to measure the gain profiles and make a first measurement of the ΔSNR. These first ΔSNR-measurements are not presented in this thesis.

In Figure A.3 the second setup used is completely depicted. The results from this setup are not presented in this thesis because the qubit was too unstable to get any good results. The pulse generator signify the up conversion setup shown in Figure 3.8 on page 3-7 and the digitizer in the setup schematics signify the down conversion setup shown in Figure 3.9 on page 3-8.

In Figure A.4 the third and fourth setups used are completely depicted. The only differences between the third and fourth setups are that the qubit was replaced with another qubit (not shown here). It was in this setup the noise temperature, quantum efficiency, single-shot readout and the ΔSNR presented in this thesis were measured.

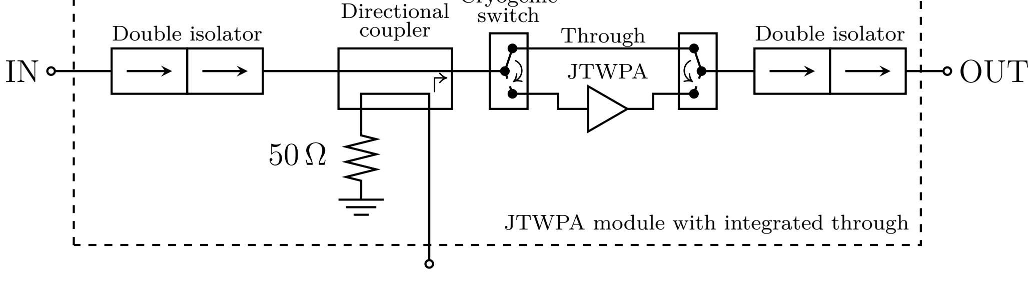

Figure A.1: Setup for measuring the gain specifically of the JTWPA, without including the losses in the lines, contacts, *etc* in the JTWPA module.

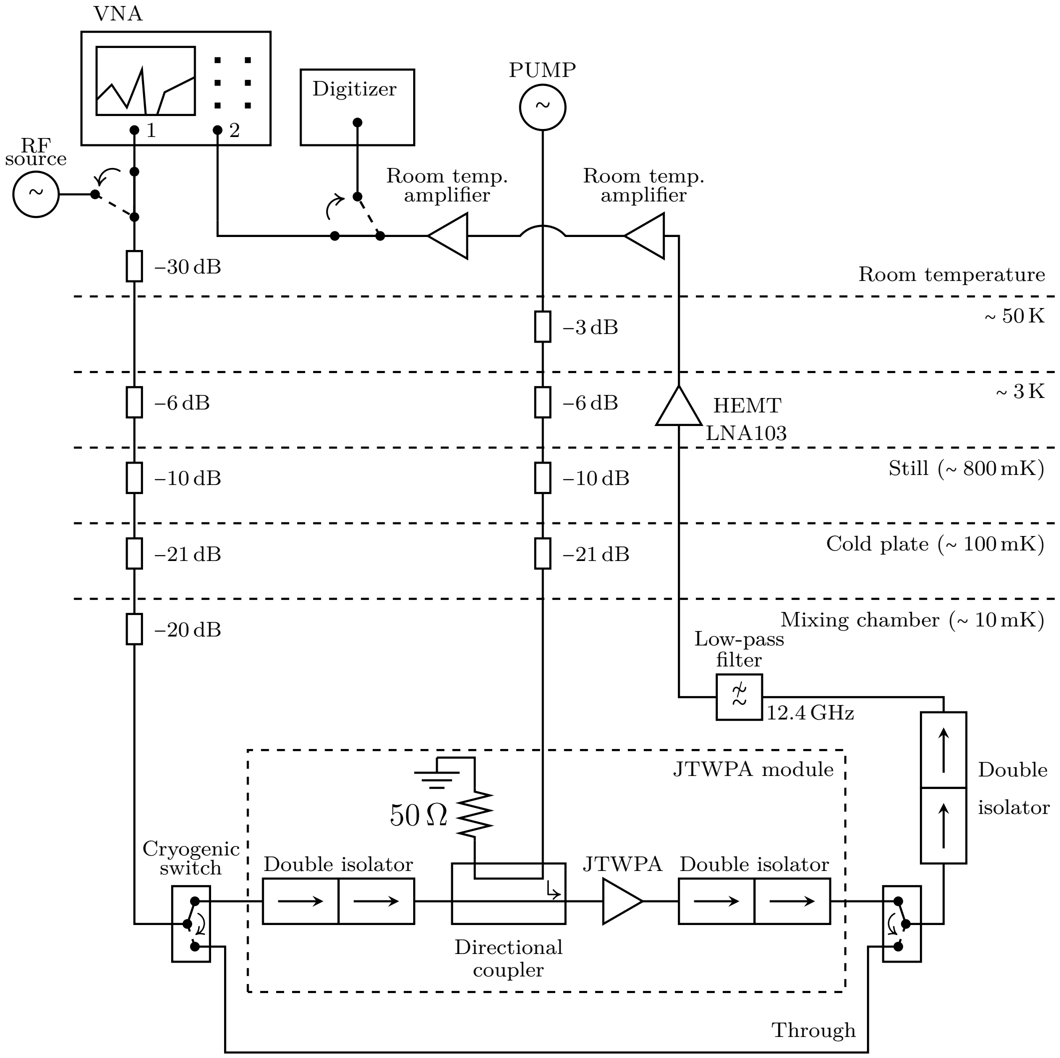

Figure A.2: The complete setup for the gain profile and ΔSNR measurements. Note the switches at room temperature allowing us to switch between using a VNA and using an RF source together with a digitizer. Also note the cryogenic switches allowing us to choose between measuring the through line and measuring through the JTWPA module. Assuming the lines down into the refrigerator have approximately 10 dB line attenuation each, the total attenuation is 97 dB of the signal line and 50 dB of the pump line. The directional coupler has a coupling of 13 dB.

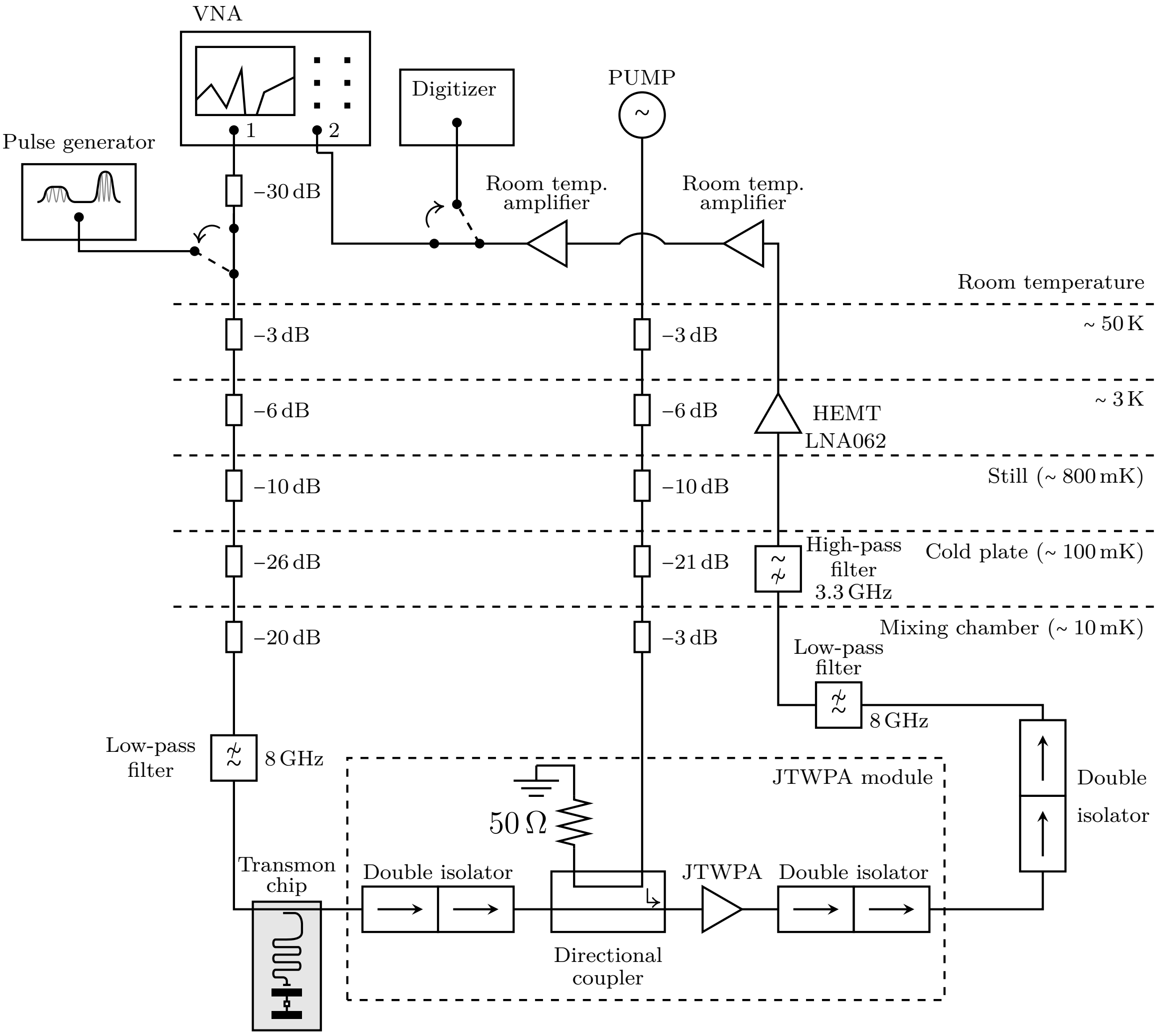

Figure A.3: The complete setup for the first try to measure the quantum efficiency. Assuming the lines down into the refrigerator have approximately 10 dB line attenuation each, the total attenuation is 75 dB on the signal line, excluding the 30 dB attenuator on the VNA, and 53 dB on the pump line. The directional coupler has a coupling of 13 dB.

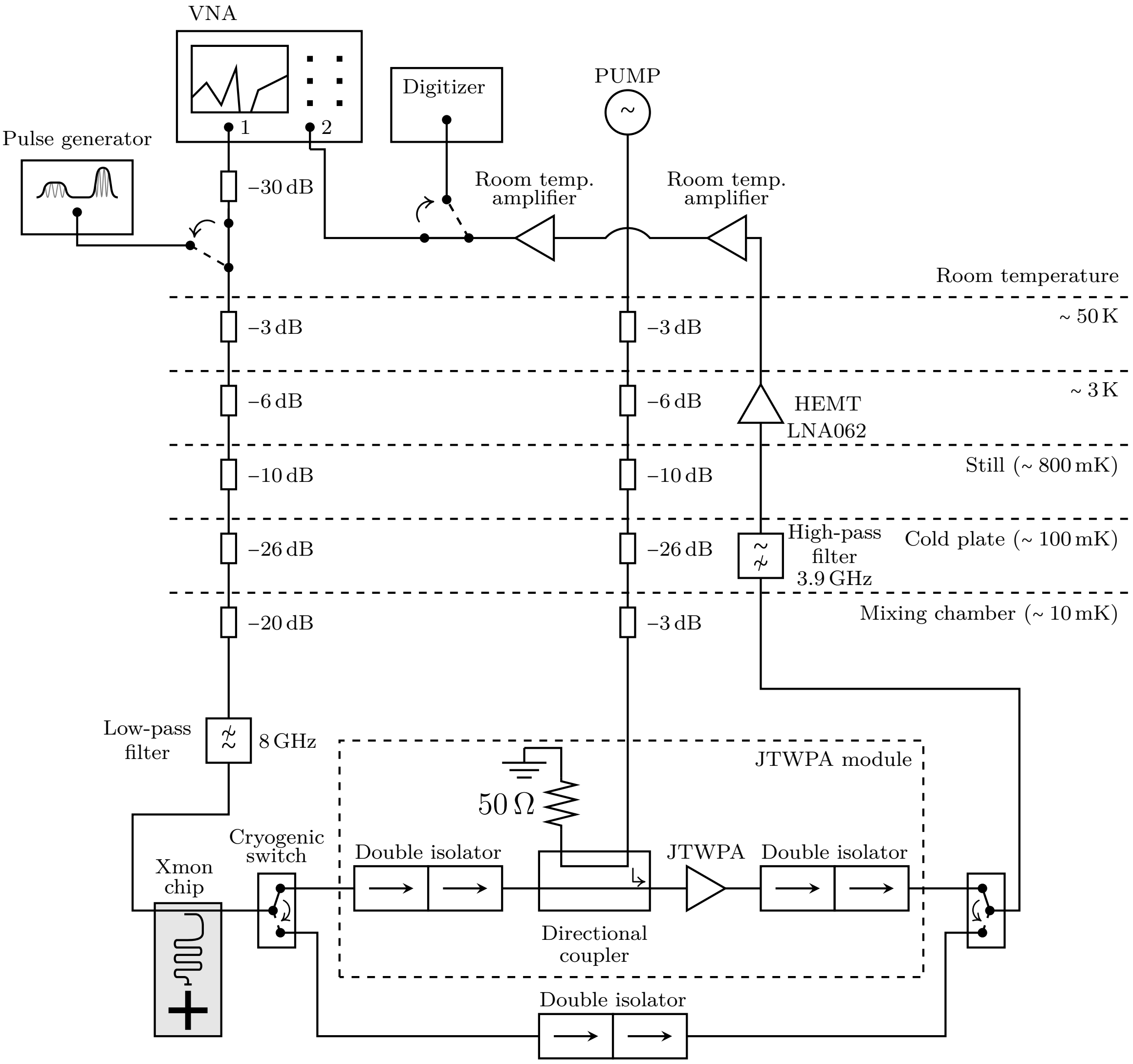

Figure A.4: The complete setup for the second try to measure the quantum efficiency. Assuming the lines down into the refrigerator have approximately 10 dB line attenuation each, the total attenuation is 75 dB on the signal line, excluding the 30 dB attenuator on the VNA, and 58 dB on the pump line. The directional coupler has a coupling of 13 dB.

B

All Signal-to-Noise Ratio improvement data

Below is all the data from the ΔSNR measurements presented.

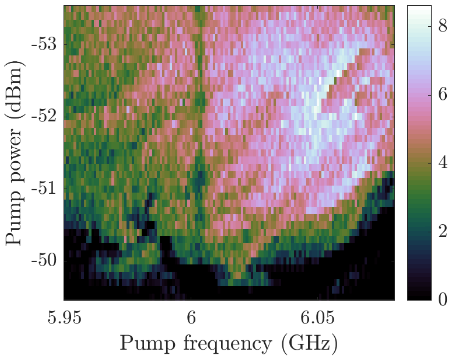

ΔSNR at 4 GHz

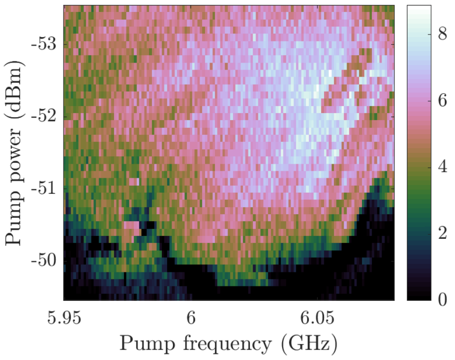

ΔSNR at 4.1 GHz

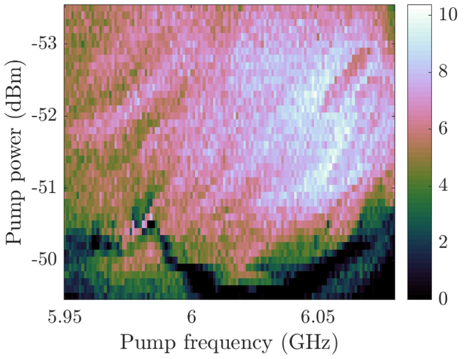

ΔSNR at 4.2 GHz

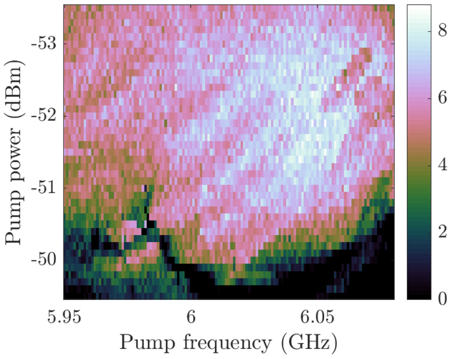

ΔSNR at 4.3 GHz

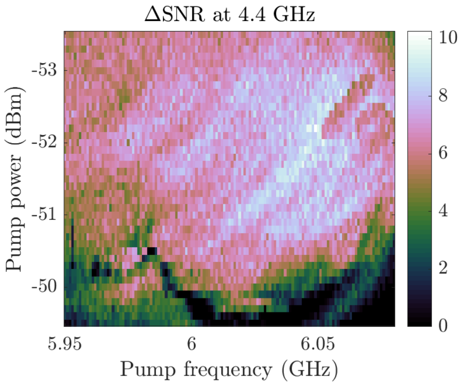
ΔSNR at 4.4 GHz

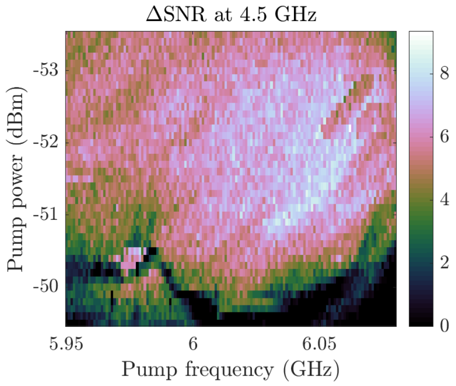
ΔSNR at 4.5 GHz

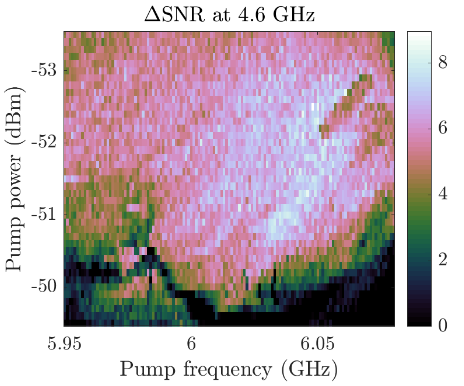
ΔSNR at 4.6 GHz

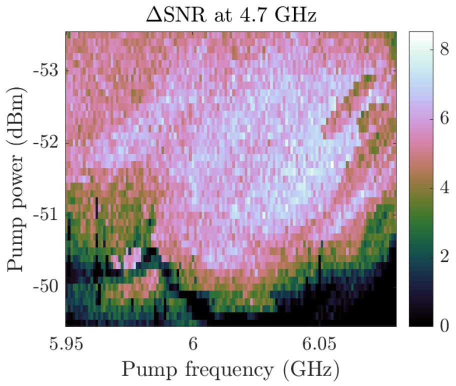
ΔSNR at 4.7 GHz

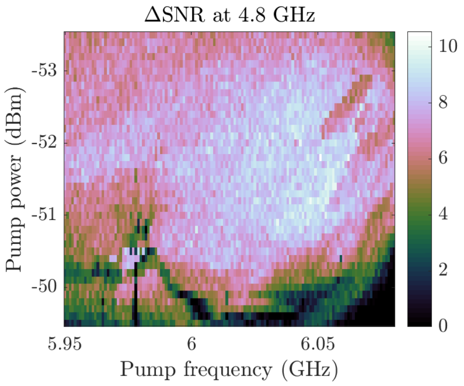
ΔSNR at 4.8 GHz

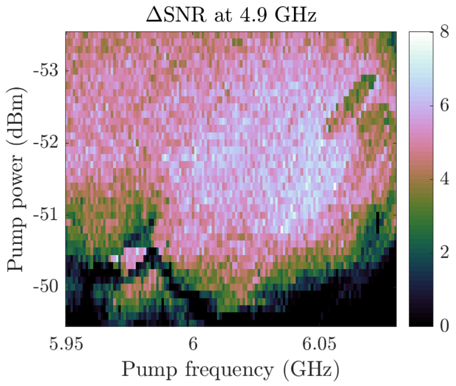
ΔSNR at 4.9 GHz

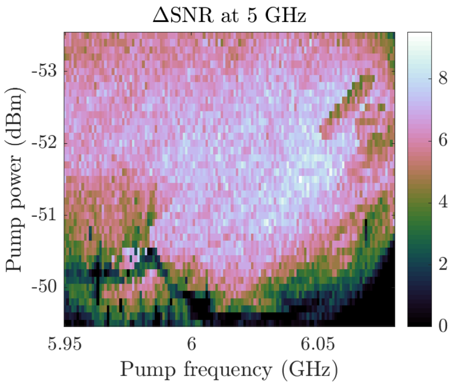
ΔSNR at 5 GHz

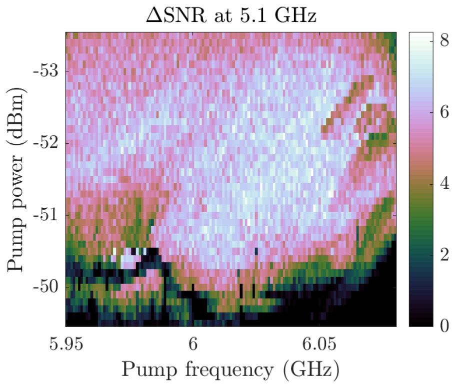
ΔSNR at 5.1 GHz

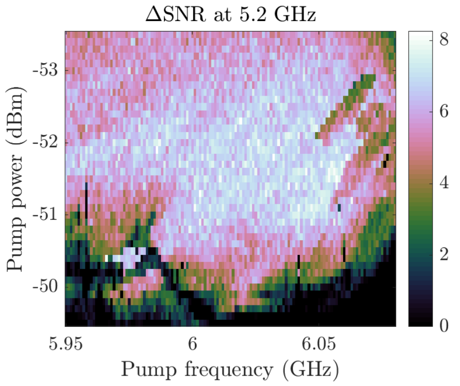
ΔSNR at 5.2 GHz

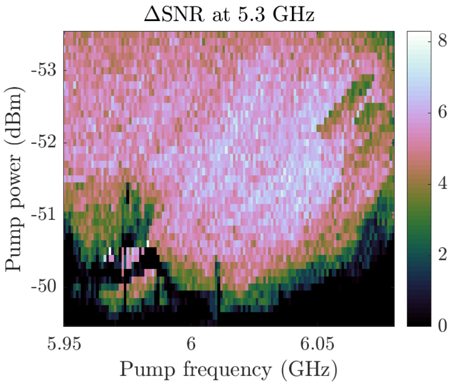
ΔSNR at 5.3 GHz

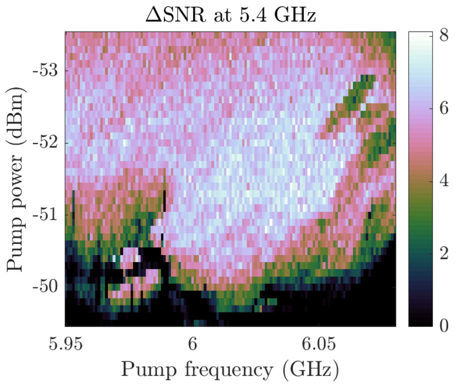
ΔSNR at 5.4 GHz

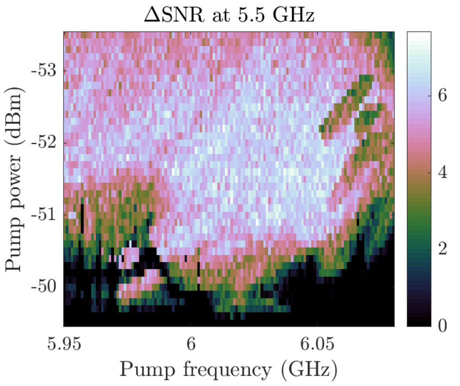
ΔSNR at 5.5 GHz

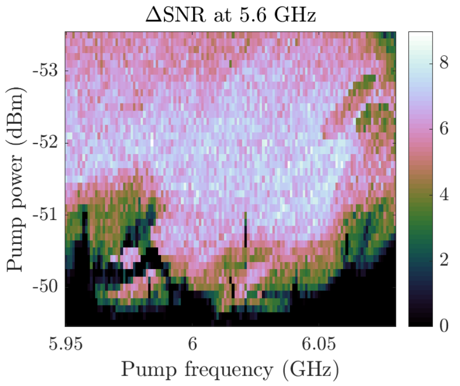
ΔSNR at 5.6 GHz

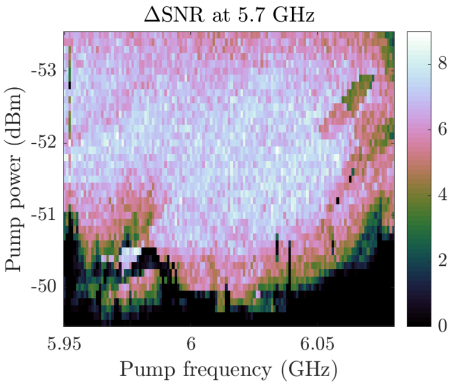
ΔSNR at 5.7 GHz

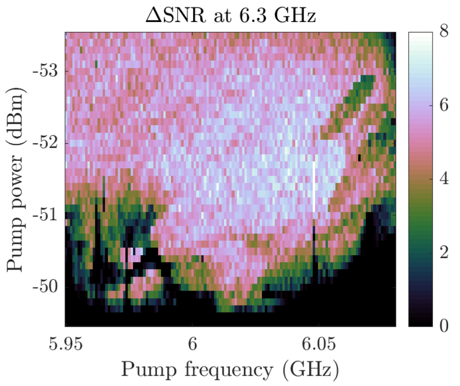
ΔSNR at 6.3 GHz

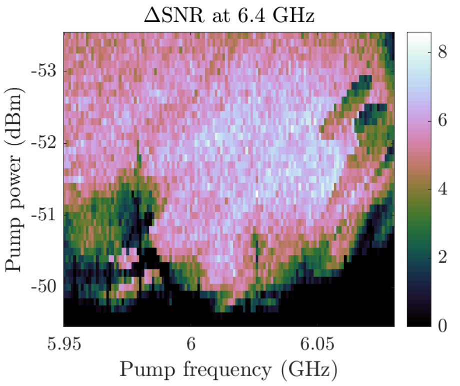
ΔSNR at 6.4 GHz

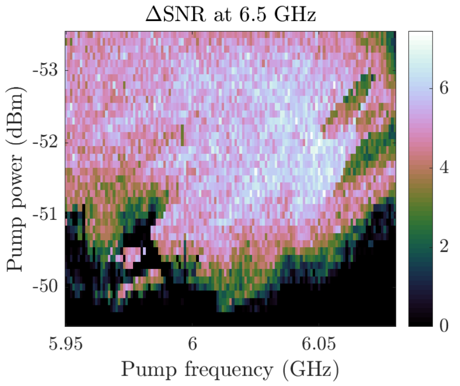
ΔSNR at 6.5 GHz

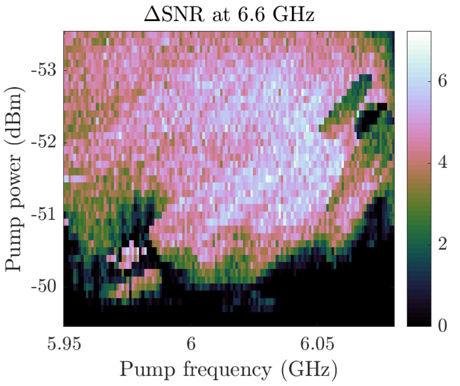
ΔSNR at 6.6 GHz

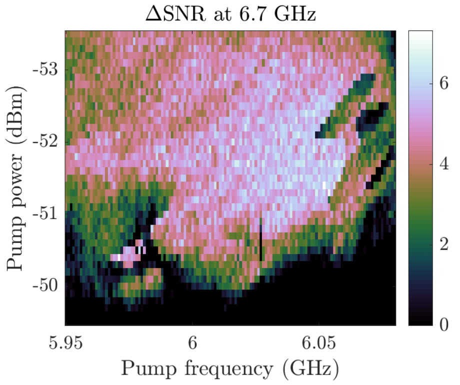
ΔSNR at 6.7 GHz

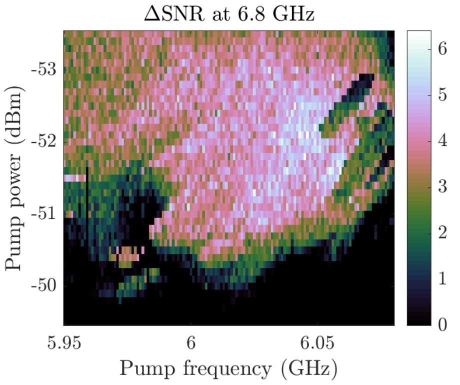
ΔSNR at 6.8 GHz

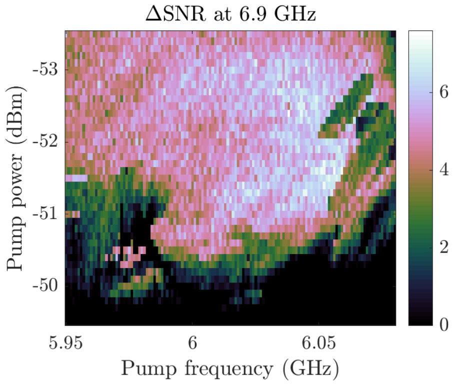
ΔSNR at 6.9 GHz

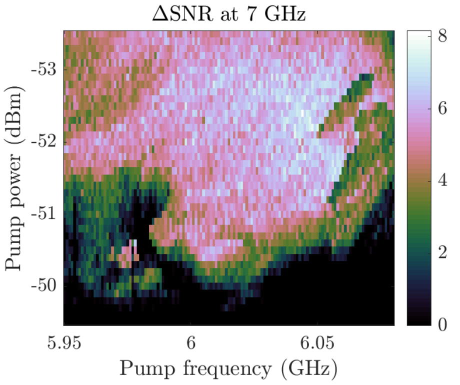
ΔSNR at 7 GHz

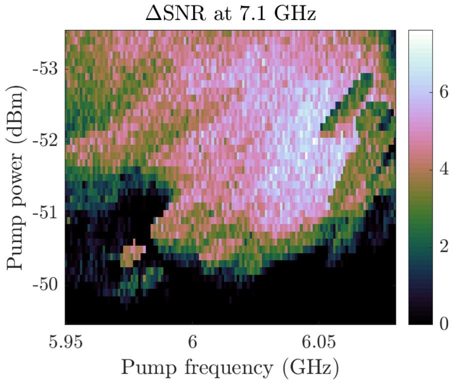
ΔSNR at 7.1 GHz

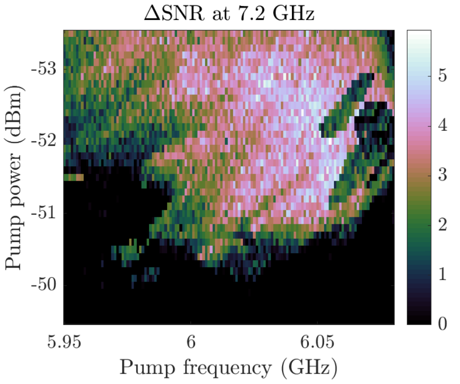
ΔSNR at 7.2 GHz

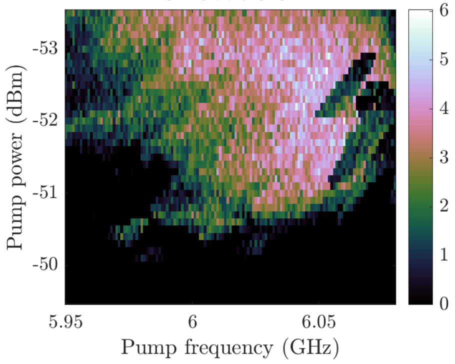
ΔSNR at 7.3 GHz

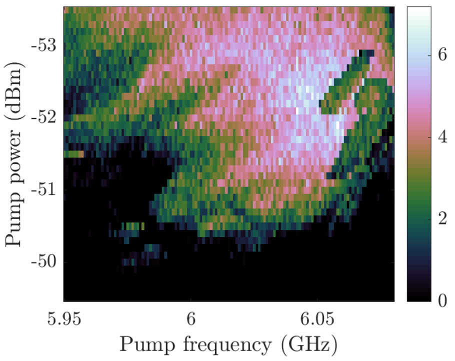
ΔSNR at 7.4 GHz

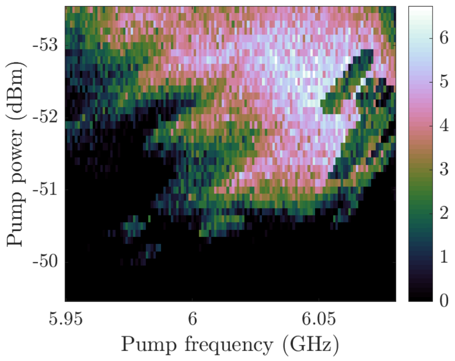
ΔSNR at 7.5 GHz

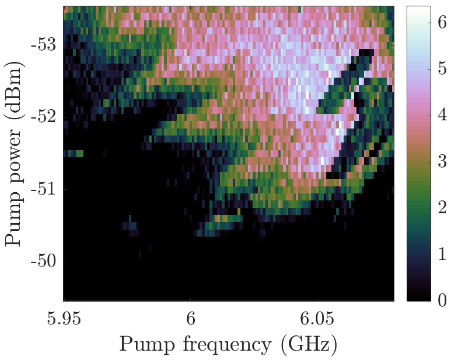
ΔSNR at 7.6 GHz

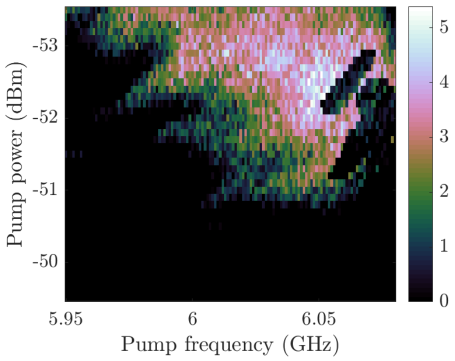
ΔSNR at 7.7 GHz

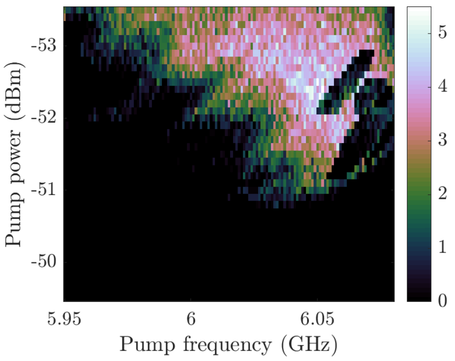
ΔSNR at 7.8 GHz

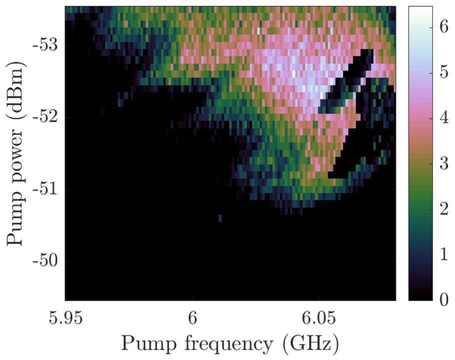
ΔSNR at 7.9 GHz

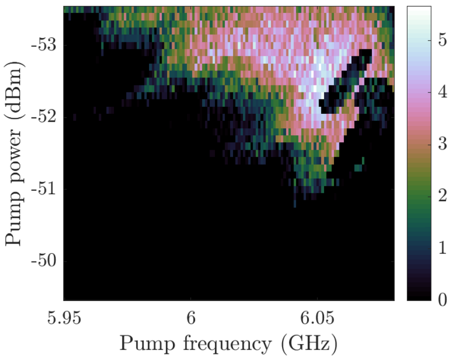
ΔSNR at 8 GHz

C

Derivations

This appendix contains interesting derivations that did not get into the thesis.

C.1 Derivation of Friis' formula

Consider a chain of n amplifiers with lossless cables as depicted in Figure C.1. Each amplifier has a gain and a noise temperature. Since we assume lossless cables the signal at node 1, denoted S_1 will be equal to the signal at the signal source, the initial signal S_i.

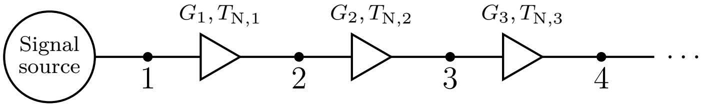

Figure C.1: A signal source connected to an amplifier chain, where amplifier i has gain G_i and noise temperature $T_{\mathrm{N},i}$.

The signal will be amplified through the chain with the gain of each amplifier and the final signal S_f will hence be given by

$$S_\mathrm{f} = S_\mathrm{i} \prod_{i=1}^{n} G_i \qquad \Longrightarrow \qquad S_4 = G_1 G_2 G_3 S_1 \tag{C.1}$$

where the latter equality is a simplification in the case of three amplifiers.

The noise will have a contribution from each amplifier which will then be amplified through all the remaining amplifiers,

$$T_{\mathrm{cont}.i} = T_{\mathrm{N},i} \prod_{j=i}^{n} G_j. \tag{C.2}$$

The total noise after the amplifier chain can hence be expressed as

$$\begin{aligned} T_\mathrm{f} &= \sum_{i=1}^{n} \left(T_{\mathrm{N},i} \prod_{j=i}^{n} G_j \right) \\ &= G_1 G_2 G_3 T_{\mathrm{N},1} + G_2 G_3 T_{\mathrm{N},2} + G_3 T_{\mathrm{N},3} \end{aligned} \tag{C.3}$$

where the latter equality is a simplification in the case of three amplifiers.

Now we express the signal-to-noise-ratio after the amplifier chain,

$$\frac{S_\mathrm{f}}{T_\mathrm{f}} = \frac{S_\mathrm{i}\prod_{i=1}^{n} G_i}{\sum_{i=1}^{n}\left(T_{\mathrm{N},i}\prod_{j=i}^{n} G_j\right)} = \frac{S_\mathrm{i}}{\sum_{i=1}^{n}\left(T_{\mathrm{N},i}\frac{\prod_{j=i}^{n} G_j}{\prod_{i=1}^{n} G_i}\right)} = \frac{S_\mathrm{i}}{\sum_{i=1}^{n}\left(T_{\mathrm{N},i}/\prod_{j=1}^{i-1} G_j\right)} \tag{C.4}$$

and we see that the noise at the end of the chain, compared with the original signal, is given by the denominator of this fraction, *i.e.* the system noise temperature is

$$T_\mathrm{sys} = \sum_{i=1}^{n}\frac{T_{\mathrm{N},i}}{\prod_{j=1}^{i-1} G_j} \tag{C.5}$$

which is Friis' formula for the system noise temperature.

In the case of three amplifiers this calculation would hence be

$$\begin{aligned}\frac{S_4}{T_4} &= \frac{G_1G_2G_3S_1}{G_1G_2G_3T_{\mathrm{N},1} + G_2G_3T_{\mathrm{N},2} + G_3T_{\mathrm{N},3}} \\ &= \frac{S_1}{\left(\frac{G_1G_2G_3T_{\mathrm{N},1}+G_2G_3T_{\mathrm{N},2}+G_3T_{\mathrm{N},3}}{G_1G_2G_3}\right)} \\ &= \frac{S_1}{T_{\mathrm{N},1} + \frac{T_{\mathrm{N},2}}{G_1} + \frac{T_{\mathrm{N},3}}{G_1G_2}}\end{aligned} \tag{C.6}$$

and we extract that the system noise temperature is

$$T_\mathrm{sys} = T_{\mathrm{N},1} + \frac{T_{\mathrm{N},2}}{G_1} + \frac{T_{\mathrm{N},3}}{G_1G_2} \tag{C.7}$$

which is Friis' formula for the system noise temperature of 3 amplifiers.

C.2 Derivation of rotation angle for maximised resolution

Assume we have two complex numbers z_1, z_2, *e.g.* the readout results of a single-shot readout measurement of a qubit. The goal here is to rotate these complex numbers such that all information is stored in one axis, *e.g.* the real axis. Then only the I channel contains information and the Q channel can be disregarded.

After a rotation of θ radians around origin the complex numbers can be written as

$$z_1 = r_1 \mathrm{e}^{\mathrm{i}(\theta_1+\theta)}, \tag{C.8a}$$

$$z_2 = r_2 \mathrm{e}^{\mathrm{i}(\theta_2+\theta)}. \tag{C.8b}$$

In order to maximise the readout resolution, we rotate them such that they get the same imaginary part. Then all the information will be stored in the real-part, *i.e.* we want

$$\Im(z_1) = \Im(z_2) \implies r_1\sin(\theta_1+\theta) = r_2\sin(\theta_2+\theta) \tag{C.9a}$$

which we can write as a function,

$$f(\theta) = r_2 \sin(\theta + \theta_2) - r_1 \sin(\theta + \theta_1)\,. \tag{C.9b}$$

We know that the sum of two sine functions of the same variable, in this case θ, will be another sine with the same frequency, *i.e.*

$$f(\theta) = r \sin(\theta + \theta') \tag{C.9c}$$

where θ' is some phase shift. Since we want the difference between the imaginary parts to be zero we now want to find the θ making $f = 0$, which we see from Equation (C.9c) is $\theta = -\theta'$, so the task now is to find $-\theta'$. By putting together Equations (C.9b) and (C.9c) and using smart choices of θ we can find useful relations in order to identify θ',

$$f(-\theta_1) = r \sin(\theta' - \theta_1) = r_2 \sin(\Delta\theta)\,, \tag{C.10a}$$

$$f\left(\frac{\pi}{2} - \theta_1\right) = r \cos(\theta' - \theta_1) = r_2 \cos(\Delta\theta) - r_1, \tag{C.10b}$$

where $\Delta\theta \coloneqq \theta_2 - \theta_1$. Now by dividing Equation (C.10a) with Equation (C.10b) we get

$$\tan(\theta' - \theta_1) = \frac{r_2 \sin(\Delta\theta)}{r_2 \cos(\Delta\theta) - r_1} \tag{C.11}$$

which we can solve for θ' and we get

$$\theta' = \theta_1 + \arctan\left(\frac{r_2 \sin(\Delta\theta)}{r_2 \cos(\Delta\theta) - r_1}\right) + n\pi, \quad n \in \mathbb{Z}. \tag{C.12}$$

To summarise, by rotating the two complex numbers z_1, z_2 with $-\theta'$ given in Equation (C.12) we get

$$z_1 = r_1 \mathrm{e}^{\mathrm{i}(\theta_1 - \theta')}, \tag{C.13a}$$

$$z_2 = r_2 \mathrm{e}^{\mathrm{i}(\theta_2 - \theta')} \tag{C.13b}$$

which will have the same imaginary part and thus all information in the real axis.

C.3 Estimation of system noise temperature using the JTWPA

In this section I estimate the system noise temperature using the JTWPA module, as a function of JTWPA gain and JTWPA ΔSNR. The main differences from the derivation of Friis' formula in Appendix C.1 are two: firstly the signal strength is assumed to be so small that vacuum noise has to be considered, and secondly the lines are now assumed to not be lossless anymore.

C.3.1 Schematics

The schematics of a general setup are presented in Figure C.2 and the JTWPA module setup is presented in Figure C.3.

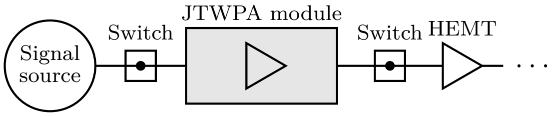

Figure C.2: A general schematic with the JTWPA module. Some signal is sent through a cable to the JTWPA module and then it goes to the HEMT-amplifier.

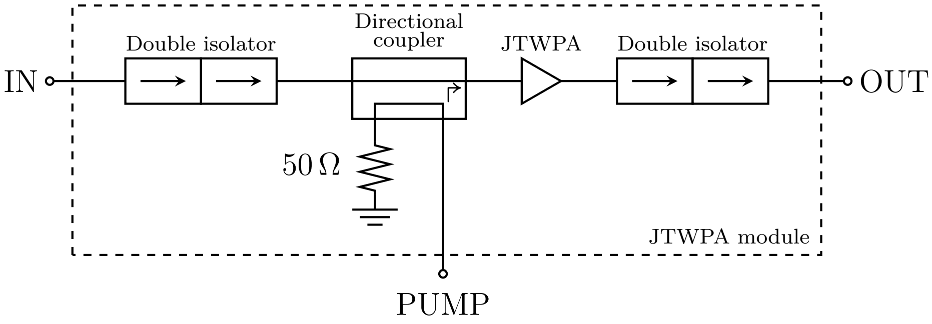

Figure C.3: The JTWPA module setup.

This schematic is rewritten as a model with attenuators representing the cable losses and insertion losses of the non-amplifying components, and the amplifiers, presented in Figure C.4. Since the insertion loss of the JTWPA is not included in the attenuation in the figure, the gain G considered for the calculations must be the effective gain.

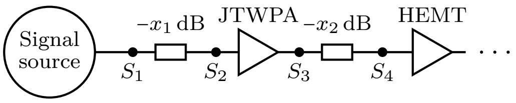

Figure C.4: A model of Figure C.2. The signal source generates a signal S_1 which is then attenuated and amplified by the cables and the components in the JTWPA module before reaching the HEMT amplifier.

C.3.2 Attenuation estimation

In order to estimate the noise temperature, first we need to estimate the attenuators x_1 and x_2. The attenuation x_1 corresponds to the losses between the signal source and the JTWPA. This path contains a switch with approximately 1 dB attenuation, an isolator with approximately 0.2 dB attenuation and a directional coupler with insertion loss L presented in Table C.1[1].

---

[1] Values taken from `https://www.markimicrowave.com/Assets/datasheets/C13-0126.pdf`

Table C.1: The insertion loss L of the directional coupler according to its specifications and the estimated attenuation x_1 at a few selected frequencies. The latter relates to the first one by adding 0.2 dB for the isolator and 1 dB for the cables.

f	L	x_1
4 GHz	0.4 dB	2.60 dB
5 GHz	0.45 dB	2.65 dB
7 GHz	0.5 dB	2.70 dB
8 GHz	0.55 dB	2.75 dB

The attenuation x_2 we estimate to be 2.2 dB, where 0.2 dB is from the double isolator, 1 dB from the cables between the JTWPA module and the HEMT amplifier and 1 dB from a switch.

C.3.3 Noise temperature estimation

The classical noise temperature can be estimated by estimating the signal strength S_4 at the HEMT amplifier. We do this step by step. First we estimate S_2 simply as

$$S_2 = S_1 \cdot 10^{-\frac{x_1}{10}} \tag{C.14a}$$

then S_3 as

$$S_3 = G S_2 \tag{C.14b}$$

where G is the effective gain of the JTWPA. Finally S_4 is estimated as

$$S_4 = S_3 \cdot 10^{-\frac{x_2}{10}}. \tag{C.14c}$$

All put together we get

$$S_4 = \underbrace{10^{-\frac{x_1+x_2}{10}} G}_{G'} S_1. \tag{C.15}$$

The noise after the first attenuator will be the same as before the amplifier [13], hence the first attenuator does not affect the noise amplitude, but otherwise the calculation is the same for the noise as for the signal. We end up with the noise T_4 at the HEMT amplifier to be

$$T_4 = G \cdot 10^{-\frac{x_2}{10}} \underbrace{(T_{\text{vacuum}} + T_{\text{JTWPA}})}_{\text{S.Q.L.}} + T_{\text{HEMT}} \tag{C.16}$$

where T_{vacuum} is the noise temperature due to vacuum fluctuations, T_{JTWPA} is the noise temperature of the JTWPA and $T_{\text{S.Q.L.}}$ is the standard quantum limit, which is equal to the sum of these two. The signal-to-noise-ratio at the HEMT is hence

$$\begin{aligned} \frac{S_4}{T_4} &= \frac{G' S_1}{G \cdot 10^{-\frac{x_2}{10}} T_{\text{S.Q.L.}} + T_{\text{HEMT}}} \\ &= S_1 \Big/ \left(10^{\frac{x_1}{10}} T_{\text{S.Q.L.}} + \frac{T_{\text{HEMT}}}{G'}\right) \end{aligned} \tag{C.17}$$

and the system noise temperature can be extracted as the denominator of this fraction, *i.e.*

$$T_{\text{sys}} = \frac{T_{\text{HEMT}}}{G'} + T_{\text{S.Q.L.}} \cdot 10^{\frac{x1}{10}} \tag{C.18}$$

where $T_{\text{HEMT}} = 2\,\text{K}$ is the noise temperature of the HEMT amplifier and $T_{\text{S.Q.L.}}$ is given by

$$T_{\text{S.Q.L.}} = 2 \cdot \frac{1}{2}\frac{hf}{k_{\text{B}}} \tag{C.19}$$

at frequency f.

We can now solve Equation (C.18) for different effective gains G of the JTWPA, which are presented Figure C.5.

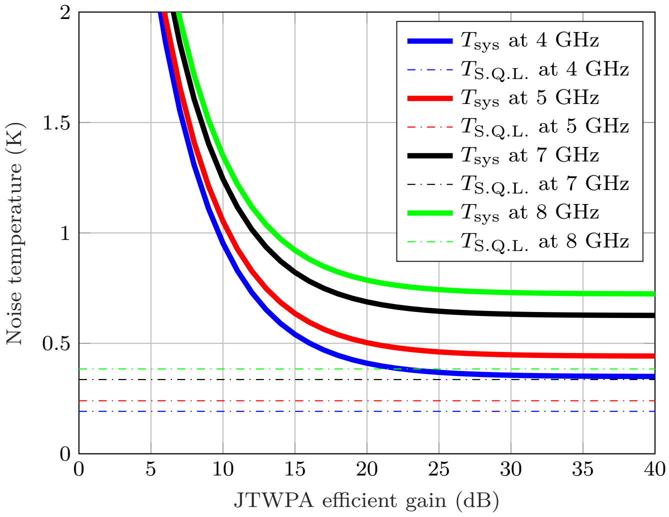

Figure C.5: System noise temperature for different effective gains of the JTWPA, compared with the noise temperature of the HEMT amplifier and the vacuum noise temperature at the frequencies 4, 5, 7, 8 GHz.

D

Investigation of directional couplers

One crucial component in the JTWPA setup is the directional coupler. In the thesis it is stated that the directional coupler used was Marki's model "C13-0126", but it is never really explained why. This appendix aims to go through the investigation of directional couplers and explain why the chosen one was chosen.

D.1 The priorities for the coupler

A list of priorities for the coupler was made in order to simplify the process. Below is the list revised by the supervisor.

1. **Couples the interval 5.8 - 6.2 GHz.** We knew that the optimal pump frequency was going to be in this interval. The reason to use a directional coupler was to couple the pump, so if it did not couple signals in this interval there would not be any reason to use it at all.

2. **Low insertion loss in the interval 4 - 8 GHz.** Since the HEMTs work in the interval 4 - 8 GHz the qubit readout resonators are also made to work in this interval. Since the point of the JTWPA is to amplify a very weak signal in this interval it is important that the signal is not reduced further, *i.e.* that the insertion loss is as small as possible.

3. **High directivity in the interval 5.8 - 6.2 GHz.** A finite directivity, which is always the case in reality, implies that some part of the pump signal will exit the wrong port of the coupler and travel towards the qubit. This signal could then interfere with the qubit. Therefore the directivity should be large enough that it is negligible compared with the pump signal reflected at the JTWPA.

4. **A low coupling factor, *i.e.* high coupling, in the interval 5.8 - 6.2 GHz.** The part of the pump that is not coupled is turned into heat at the isolated port. If the coupling is low then the power of the pump must be higher

and thereby there will be more heating, which we do not want since we want the system to stay at 10 mK.

D.2 Comparison of different couplers

It was known at the division that directional couplers from Marki worked well at cryotemperatures, which is why only directional couplers from Marki were investigated thoroughly. In Table D.1 a selected few directional couplers from Marki are compared with a theoretical desired directional coupler.

Table D.1: Some of the most promising directional couplers from Marki that coupled the relevant frequency interval. Insertion loss refers to the maximum insertion loss on the interval 4 - 8 GHz and directivity and coupling to the directivity and coupling around 6 GHz. The values in the table are read out from graphs so they are only approximately correct.

Coupler	**Insertion loss**		**Directivity**		**Coupling**	
Desired	≤ 0.5 dB		≥ 25 dB		≤ 20 dB	
C09-0R412	1.1 dB	✗	25 dB	✓	9 dB	✓
C10-0116	1 dB	✗	29 dB	✓	10 dB	✓
C13-0126	0.5 dB	✓	27 dB	✓	13 dB	✓
C20-0226	0.3 dB	✓	22 dB	✗	21 dB	✗
C20-0R518	0.9 dB	✗	30 dB	✓	20 dB	✓

In the end the model C13-0126 was chosen because it met all requirements while other models failed in one of the categories. Some other models, that are not listed in the table above, also met the requirements of the table but failed in some other way. Either they did not have SMA connectors, they coupled the wrong interval, they had an internal termination of the isolated port, or something else.

E

Pump filter design

In order to get rid of the pump from the output line of the refrigerator, without attenuating the signal, a high-quality narrow-band notch filter is needed. The steps of making this filter are described below.

E.1 Definitions

First we define the desired characteristics of the filter by defining at which frequencies the stopband should work. We define the relevant frequencies as

$$f_1 = 5.9\,\mathrm{GHz}, \tag{E.1a}$$

$$f_2 = 6.1\,\mathrm{GHz}, \tag{E.1b}$$

$$f_0 = \frac{f_1 + f_2}{2}, \tag{E.1c}$$

$$\delta f = f_2 - f_1, \tag{E.1d}$$

$$\omega_i = 2\pi f_i, \tag{E.1e}$$

$$\delta\omega = 2\pi\delta f \tag{E.1f}$$

where f_1, f_2 are the lower and upper cutoff frequencies of the stopband, f_0 the center frequency, δf the bandwidth and ω_i the corresponding angular frequencies for $i \in \{0, 1, 2\}$.

E.2 Ideal filter design

We use the topology shown in Figure E.2 with a high quality factor $Q = 1000$ of the resonators and we find an ideal filter which performs very well in simulations. The filter is simulated in Advanced Design System and the results from this simulation are presented in Figure E.2.

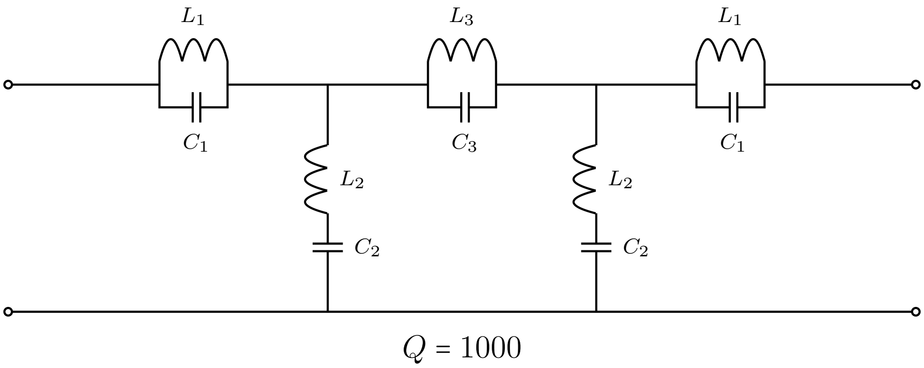

Figure E.1: An ideal filter filtering frequencies in the relevant stopband interval while letting frequencies outside the stopband transmit with low losses. The filter is symmetric and alternates between parallel resonators along the transmission line and series resonators to ground. Each resonator has the quality factor $Q = 1000$.

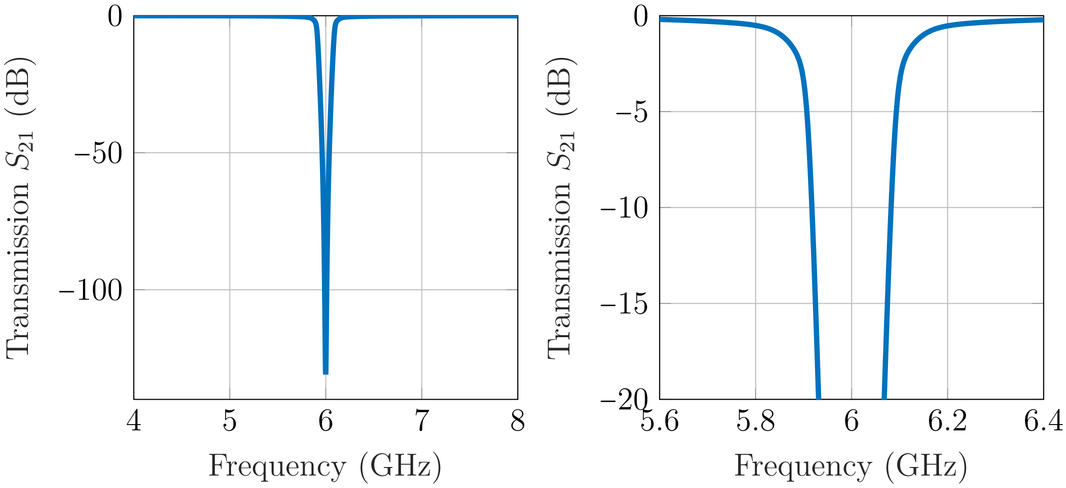

(a) **(b)**

Figure E.2: The transmission results of simulating the filter in Figure E.1 in Advanced Design System. The filter has almost zero losses outside the stopband, while the stopband reaches almost 150 dB attenuation. **(a)** Transmission on the whole interval 4-8 GHz. **(b)** Transmission only around the stopband.

To find the necessary inductances and capacitances for the resonators we use the constants

$$k_1 = 1.1468, \tag{E.2a}$$

$$k_2 = 1.3712, \tag{E.2b}$$

$$k_3 = 1.975 \tag{E.2c}$$

from a table in Reference [37] and define the impedances as

$$C_1^{-1} = Z_0 k_1 \delta\omega, \tag{E.3a}$$
$$C_2^{-1} = L_2 \omega_0^2, \tag{E.3b}$$
$$C_3^{-1} = Z_0 k_3 \delta\omega, \tag{E.3c}$$
$$L_1^{-1} = C_1 \omega_0^2, \tag{E.3d}$$
$$L_2^{-1} = \frac{1}{Z_0} k_2 \delta\omega, \tag{E.3e}$$
$$L_3^{-1} = C_3 \omega_0^2. \tag{E.3f}$$

E.3 Transformation to ideal transmission lines

As a next step the ideal lumped-element filter is transformed into ideal transmission lines. This transformation is done using a method described in Reference [37]. By defining the impedances

$$Z_1 = \sqrt{\frac{L_2}{C_1}} \approx 45.73\,\Omega, \tag{E.4a}$$
$$Z_2 = \sqrt{\frac{L_2}{C_2}} \approx 1094\,\Omega, \tag{E.4b}$$
$$Z_3 = \sqrt{\frac{L_2 C_3^2}{C_1^2 C_2}} \approx 635.2\,\Omega \tag{E.4c}$$

we can then rewrite the filter to a transmission line filter, see Figure E.3. Then this new, transformed, version of the filter is simulated using Advanced Design System, presented in Figure E.4.

The results from this simulation may seem very interesting. The highest attenuation of the transformed filter is now almost 800 dB while the losses are still very small. In theory this filter should have 0 transmission, *i.e.* $-\infty$ dB transmission. That we still get a finite value, 800 dB, is probably due to some simulation or rounding limitations.

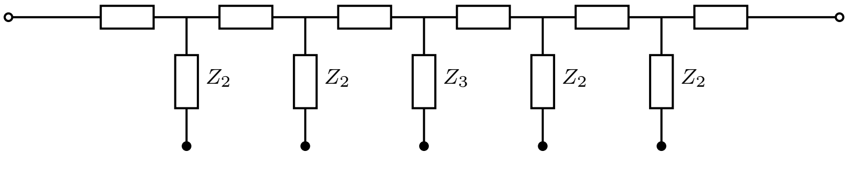

Figure E.3: The ideal filter transformed into ideal transmission lines with impedances Z_1, Z_2, Z_3. Each transmission line has centre frequency f_0 and electrical length $\frac{\pi}{2}$, *i.e.* the phase for a signal at the centre frequency changes $\frac{\pi}{2}$ over the length of the transmission line. The filled circles signify that the circuit is open there.

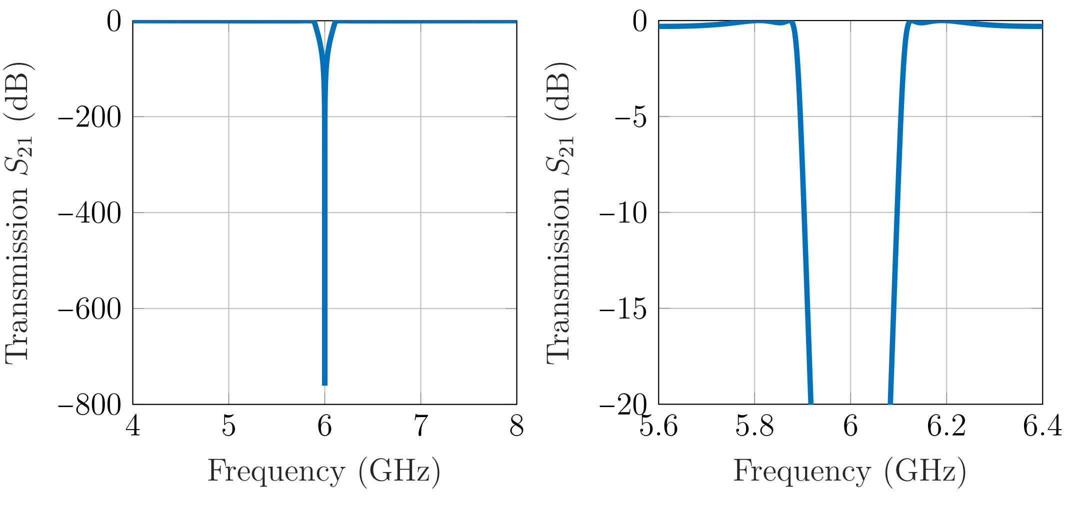

(a) **(b)**

Figure E.4: The simulated transmission response of the filter in Figure E.3 in Advanced Design System. This filter has some, but still negligible, losses outside the stopband, while having almost 800 dB attenuation at the lowest point. **(a)** Transmission on the whole interval 4-8 GHz. **(b)** Transmission only around the stopband.

E.4 Transformation to rectangular wave guides

To be able to fabricate the filter, a physical design is needed. This was not possible to realistically simulate in Advanced Design System so instead it was simulated in Ansys® HFSS. Ansys HFSS simulates the propagation of the actual electric fields, which makes its simulations very accurate.

At this point we got a problem though. The technology needed in order to get a high enough quality factor Q of the resonators requires wave guide technology. But the calculated value of Z_1 is below the impedance of free space, $Z_0 \approx 377\,\Omega$, so we could not translate our ideal transmission line model directly to a wave guide. Instead, we tried to make it as similar as possible and then simply used numerical optimisation to find a fairly good filter. The best simulated result is presented in Figure E.5 and the design for this result is presented in Figures E.6 and E.7.

E.5 Transformation to a manufacturable filter

The results from the simulation shown in Figure E.5 were no longer as good as in the simulation using ideal transmission lines, but we thought it might still be good enough.

However, it turned out it would be hard to manufacture this filter design with a high quality, due to the resonators being placed on multiple sides of the main wave guide. Therefore we tried transforming the filter design into a design where all the resonators were located on one side of the main wave guide. None of the simulations of these transformed filters ever showed any promising results and finally we gave up on the task.

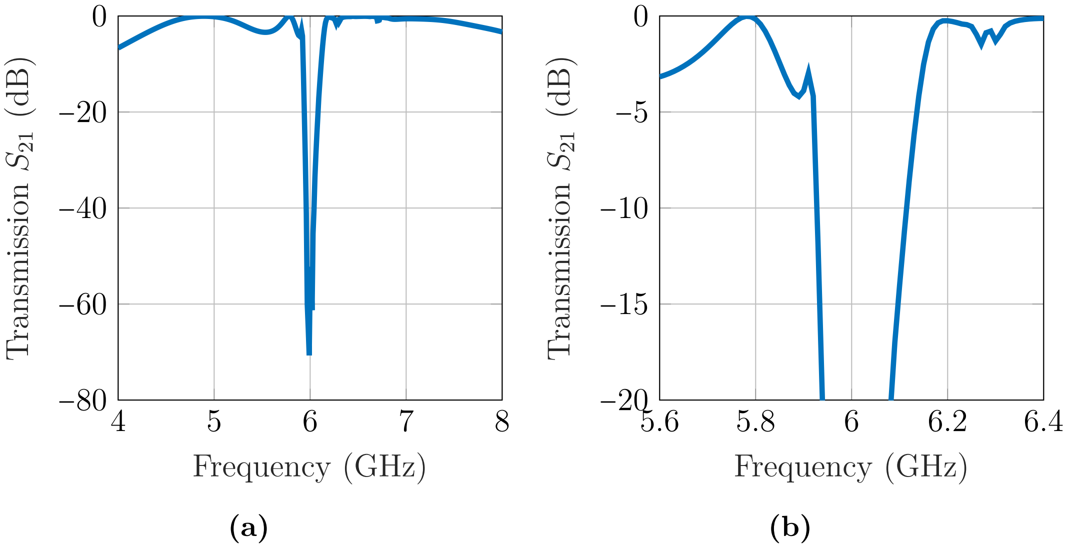

Figure E.5: The results of simulating the wave guide filter in Ansys® HFSS. **(a)** Transmission on the whole interval 4-8 GHz. **(b)** Transmission only around the stopband.

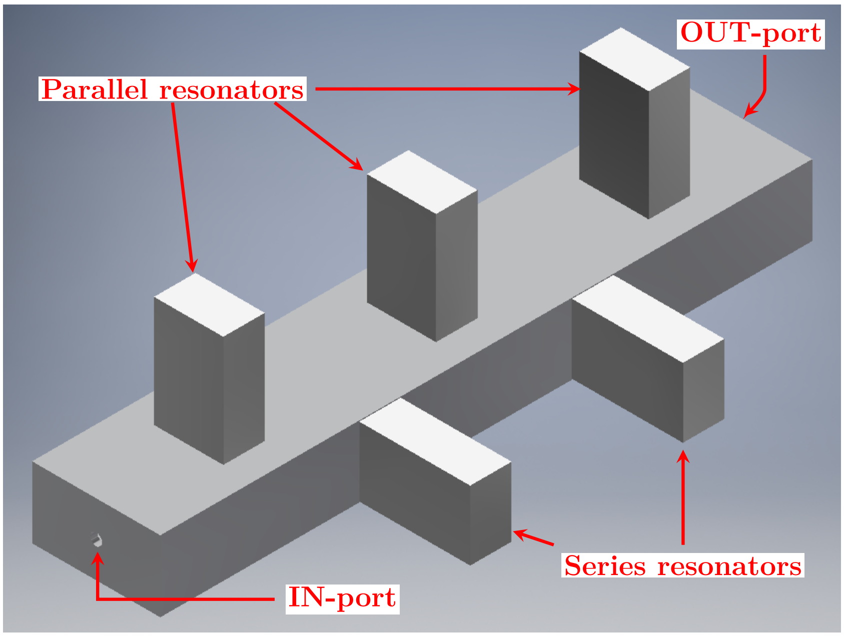

Figure E.6: The wave guide filter simulated in Ansys® HFSS. The filter is basically a long metal box, the main wave guide, with different boxes on the sides, the resonators. Whether a resonator works as a parallel resonator or a series resonator depends on what side of the wave guide the resonator is placed.

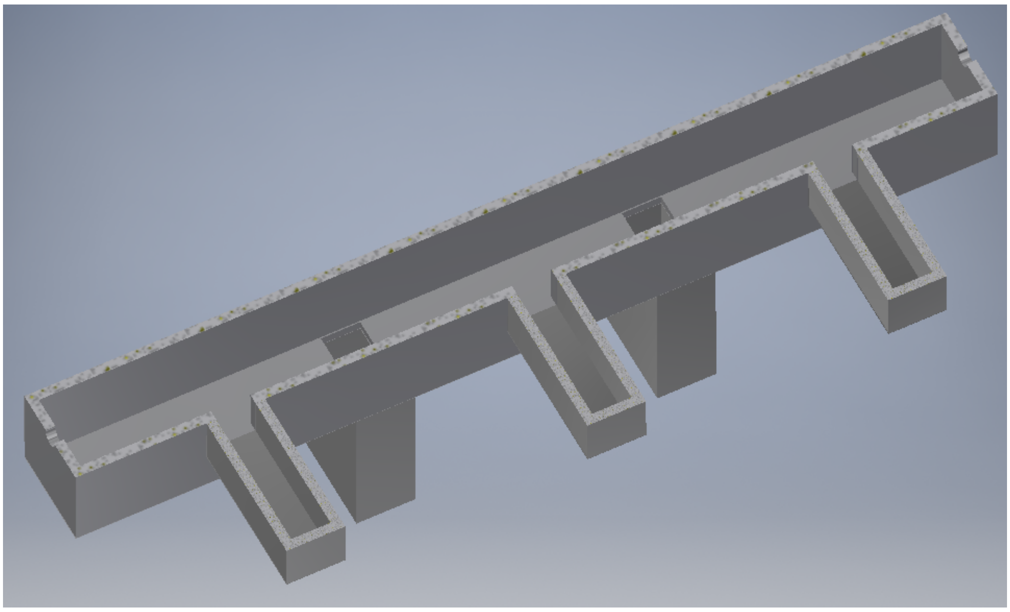

Figure E.7: The wave guide filter in a half section view. Note that all the resonators are simply hollow boxes with an opening towards the main wave guide.